STATISTICAL & DYNAMICAL MULTIPLE-SCALE PREDICTABILITY OF THE NORTH PACIFIC OCEAN

A Dissertation
Presented to
The Academic Faculty

by

Tongtong Xu

In Partial Fulfillment
of the Requirements for the Degree
Doctor of Philosophy in the
School of Civil and Environmental Engineering

Georgia Institute of Technology
August 2021

STATISTICAL & DYNAMICAL MULTIPLE-SCALE PREDICTABILITY OF THE NORTH PACIFIC OCEAN

Approved by:

Dr. Kevin A. Haas, Advisor
School of Civil and Environmental Engineering
Georgia Institute of Technology

Dr. Jian Luo
School of Civil and Environmental Engineering
Georgia Institute of Technology

Dr. Emanuele Di Lorenzo, Co-Advisor
Program in Ocean Science and Engineering
Georgia Institute of Technology

Dr. Matthew Newman
NOAA Physical Sciences Laboratory
CIRES, University of Colorado, Boulder

Dr. Hermann M. Fritz
School of Civil and Environmental Engineering
Georgia Institute of Technology

Date Approved: 07/26/2021

ACKNOWLEDGEMENTS

It has been a special and unique journey.

During this journey, I have received help and support from many people, who deserve reignition and to whom I am forever grateful.

I would like to express my sincere gratitude to my advisors, Dr. Kevin Haas and Dr. Emanuele Di Lorenzo. I joined Dr. Haas's group in 2014 with nothing but the curiosity of researches. It was Dr. Haas's guidance and mind-broadening discussions that shaped my perspective of science and engineering and my understanding of how to conduct thorough and objective scientific researches. I am also grateful for his continuous support throughout this entire journey. There was a time when I felt most challenged in pursuing an academic direction. That was when I became also a member of Dr. Di Lorenzo's group. Dr. Di Lorenzo provided immense guidance on my weakest spots of research work, how to identify the frontier scientific questions, initiate researches correspondingly and how to organize and write research work coherently for scientific publications. It was also Dr. Di Lorenzo's constant encouragement that led me to regaining self-confidence. Thus, despite the tough moments, I had always felt very lucky during the journey, as I had the opportunity to work with the two great advisors, Dr. Kevin Haas and Dr. Emanuele Di Lorenzo.

Next I would like to express special thanks to my collaborators, Dr. Matthew Newman, who is also a member of the committee, and Dr. Antonietta Capotondi. Both had provided many constructive comments on my first published research paper, incited mind-

stimulating discussions, and stayed on the lengthy Zoom calls to help me improve the research work. Without them the paper would not have been possible.

I would also like to acknowledge the rest of my committee members: Dr. Jian Luo and Dr. Hermann Fritz for their constructive comments and salient advice to help complete this thesis.

I would also like to extend my gratitude to the following people who have helped in various ways: to Dr. David Frost, for his constant encouragement and mentorship; to Xiufeng Yang, for his guidance on parallel computing and for his support over years; to Yilin Li, Wenjia Wang, Miko and Ahri, for their friendship and help both in my life and in study; to Donghua Cai, for her help and kindness in all the circumstances; to Xian Qin, for being the best female role model. Special thanks to the following friends: Hongmeng Ni, Shihyu Huang, Yue Zhao, Fangzhou Liu, Guangpeng Liu, Daoxun Sun, Yingying Zhao, Mahdi Roozbahani, Gian Giacomo Navarra, Jade Sainz.

Finally, I would like to thank my parents with wholehearted gratitude, for their love and support, for their patience and encouragement, for giving me the greatest strength to overcome the most challenged scenarios, and most importantly, for being in my life this far. Special thanks to Jinge Huo, for her support that helped me be brave and for her immediate help when I was most vulnerable; to Helen and Zan, for their love and tremendous kindness that saved me from troubles; to Ryan and Mango, for their accompany and reminders of the world's beauty.

TABLE OF CONTENTS

LIST OF TABLES

LIST OF FIGURES

SUMMARY

Prolonged ocean surface warming in North Pacific, such as those extreme events known as marine heatwaves, could lead to significant impact on coastal ecosystems. As such, predicting the North Pacific sea surface temperatures days to weeks to months or even years in advance, especially prolonged marine heatwaves and coastal variability, helps provide guidance to decision makers to understand the future ecosystem variation and to utilize the adverse situation to their benefits. Therefore, it is of vital importance to construct credible and effective ocean forecast systems on various spatial and temporal scales. While statistical models capture the large-scale dynamics and provide forecast skill comparable to the state-of-the-art climate models, regional dynamical models are necessary to resolve high resolution coastal processes and to improve coastal prediction skill. Thus, this thesis combined the use of a Linear Inverse Model (LIM) and the Regional Ocean Modeling System (ROMS), a widely-used empirical model and a commonly-accepted dynamical ocean model, to understand the North Pacific extremes and to evaluate North Pacific forecast on multiple spatial and temporal scales. This includes: (1) using LIM to analyze the statistical behaviors, progression, and prediction of marine heatwaves in Northeast Pacific; (2) using LIM to explore the prediction of North Pacific coastal systems and the impact of tropical versus extratropical Pacific on the prediction; (3) using a multi-scale nesting configuration of ROMS to resolve coastal processes and to explore the near-real time forecast skill around Pt Sal, California; (4) using the fine resolution grid of ROMS to quantify the impact of different forcings, including initial conditions, boundary forcings and atmospheric surface forcings, on the near-real time forecast.

CHAPTER 1. INTRODUCTION

The North Pacific Ocean climate variability has important impacts on weather over North America and Asia, large-scale ocean warming, and coastal marine ecosystems. This is particularly evident over the last decade when the North Pacific has experienced a series of extreme climate events with the record-breaking multi-year (2013-2015) marine heatwaves and drought over North America, the second largest El Niño of the century in 2015-2016, the recent record summer warming around the Alaskan Peninsula in 2019, and the related impacts on marine ecosystems that include massive die offs of mammals and birds, the emergence of prolonged harmful algal blooms and the closure of commercial fisheries. While much progress has been done in predicting large-scale phenomena like El Niño, less is known about the dynamics and prediction skill of prolonged marine heatwaves and of coastal systems in the Pacific Basin. This work aims at understanding the forecast of these extremes and of coastal systems on multiple spatial and temporal scales from their large-scale dynamical evolution to their impacts on the coast at the scale that are relevant for managing marine ecosystem services and operations.

1.1 Introduction to Climate Dynamics in North Pacific

This section begins with an introduction to the Northeast Pacific marine heatwaves, as a novel concept of the North Pacific extremes and a motivation of the forecast study, followed by the introduction of the general atmospheric and oceanic circulation in North Pacific, relevant dominant large-scale dynamics and the impact of climate dynamics on marine ecosystem services and operations.

1.1.1 Northeast Pacific Marine Heatwaves

Marine heatwaves (MHWs) are defined as extended periods of anomalously warm ocean surface temperatures and are often classified based on the intensity and duration of these warm anomalies (Hobday et al., 2016; Hobday et al., 2018). One of the most prominent MHWs was the 2013-2015 event, with a record-high warming of 2.8^{o}C (Bond et al., 2015; Di Lorenzo and Mantua, 2016) that persisted over a broad range of Gulf of Alaska and California Current System. The following ecosystem impact was unprecedented, including but not limited to, massive stranding, entanglement and mortality of marine species and seabirds (Cavole et al., 2016; Jones et al., 2018; Santora et al., 2020) and prolonged harmful algal blooms that closed major fisheries (McCabe et al., 2016; Ryan et al., 2017; Sanford et al., 2019). Triggered by this event, MHWs are under scrutiny of the scientific community on a variety of aspects, including metrics for evaluating their severities (Hobday et al., 2016; Jacox et al., 2020a; Scannell et al., 2016), the driving mechanisms (Bond et al., 2015; Di Lorenzo and Mantua, 2016; Holbrook et al., 2019), the impacts of climate change on the frequency and intensity of the events (Oliver, 2019), the predictability of events in global climate models (Jacox et al., 2019b), and the impacts on marine ecosystem dynamics (Santora et al., 2020).

Many studies have focused on diagnosing the driving mechanisms behind the 2013-2015 MHW event. Specifically, the onset and growth of this extreme event is attributed to the persistence of atmospheric ridge (Bond et al., 2015), connected to the North Pacific Oscillation (NPO) (Baxter and Nigam, 2015), which acts to suppress the air-sea heat exchange and therefore increase ocean surface warming in the Northeast Pacific, resembling the North Pacific Gyre Oscillation (NPGO) (Di Lorenzo et al., 2008). This

warming propagates southwestward to the central equatorial Pacific via Wind-Evaporation-SST (WES) feedback mechanism (Xie, 1999), a phenomenon known as the Pacific Meridional Mode (PMM) (Chiang and Vimont, 2004) and often identified as a precursor to the El Niño/Southern Oscillation (ENSO). During an El Niño, the re-arrangement of tropical convection excites atmospheric Rossby wave to the higher troposphere and establishes an atmospheric teleconnection (Alexander et al., 2002) that influence the extratropical atmosphere and drives a subsequent ocean surface warming, which projects on the spatial pattern of the Pacific Decadal Oscillation (PDO) (Newman et al., 2003). These teleconnections from extratropics to tropics to extratropics are thought to have played a significant role in maintaining the prolonged MHW event (Di Lorenzo and Mantua, 2016) and are a key process for energizing the decadal variance of the Pacific basin (Di Lorenzo et al., 2015).

As the definition of MHW is subject to the percentage threshold and the prolonged period, while some studies focus on the categorization based on the extremity of MHW magnitude (Hobday et al., 2016; Hobday et al., 2018), others have discovered that the low frequency baseline temperature could have a significant impact on those defined as MHWs (e.g. Oliver, 2019). Specifically, it has been discussed that it is the mean temperature increase that leads to the more frequent and extreme MHWs (Oliver, 2019). Others suggest that the low frequency large-scale dynamics such as the PDO play an important role in promoting prolonged MHWs (e.g. Joh and Di Lorenzo, 2017). More recently, starting in the summer of 2019, a marine heatwave event with record-breaking SSTa occurred in the Northeast Pacific (Amaya et al., 2020). The reappearance of record-breaking MHW within 10 years seems to confirm the importance of baseline climate dynamics. Therefore,

triggered by these extreme MHWs, in the next sections and the following chapters we reviewed the ocean-atmosphere circulation and the dominant large-scale dynamics in North Pacific and, based on the understanding, modeled and analyzed how predictable the North Pacific Ocean is from a daily to interannual time scale.

1.1.2 North Pacific Atmospheric & Oceanic Circulation

Atmospheric and oceanic circulation processes interact in North Pacific and exhibit variability on timescales from diurnal (Clayson and Weitlich, 2007; Tanahashi et al., 2003) to seasonal (Jacox et al., 2019a), decadal and centennial (Mantua et al., 1997; Yeh et al., 2011). The concept of ocean-atmosphere coupling is established on the mutual feedback between ocean and atmosphere such that a large-scale ocean surface warming or cooling induces diabatic heating or cooling of the atmosphere, which, through generating a lower- or higher-pressure system, affects atmospheric circulation. Atmospheric circulation, in turn, modifies the ocean thermal structure and circulation, giving rise to positive feedbacks that reinforce the initial ocean surface warming or cooling.

In the tropical Pacific, the ocean-atmosphere coupling is characterized by an easterly trade wind inducing a positive ocean temperature gradient between western and eastern boundary of the Pacific basin. The cooler ocean surface temperature in the eastern tropical Pacific is associated with the equatorial Ekman upwelling, which brings cold water from depth to compensate the flow divergence on the ocean surface. The flow divergence is caused by the opposite direction Ekman transport, which is a net transport to the right (left) of the wind direction in the northern (southern) hemisphere balanced by Coriolis effect. Due to the presence of continents, flow in tropical Pacific in bounded, causing warm

water to accumulate in western tropical Pacific. The positive temperature gradient between western and eastern tropical Pacific is accompanied with negative pressure gradient in the overlying atmosphere, which reinforces the easterly trade wind that initially induces the positive temperature gradient on the ocean surface.

In the North Pacific, the ocean-atmosphere coupling is featured by a midlatitude westerly and a tropical easterly trade wind, which, together with the continental boundaries, induces an anticyclonic subtropical ocean circulation gyre and a cyclonic subpolar gyre. The opposing wind direction results in a converging (diverging) Ekman transport and a corresponding Ekman downwelling (upwelling) in the subtropical (subpolar) region, which is balanced by a depth integrated equatorial (poleward) Sverdrup transport. The interior Sverdrup transport of the gyre is returned meridionally in narrow western boundary currents, as a balance between current vorticity and the noneligible fictional effect near the continental coastline. On the other hand, the shallower and broader eastern boundary circulation is driven by alongshore wind stress that creates offshore (onshore) Ekman transport with a compensating coastal upwelling (downwelling) (see Vallis, 2017).

However, these atmospheric and oceanic circulation processes describe only the mean state circulation over many years and do not provide understanding toward the anomalous fluctuations of various spatial and temporal scales and the role of ocean-atmosphere coupling in those fluctuations. Since Bjerknes (1968) linked the anomalous ocean surface warming in the equatorial Pacific to a deeper than normal Aleutian low, the ocean-atmosphere coupling connecting the anomalous climate dynamics in the tropical Pacific with the extratropics, which has been collectively represented as the tropical-

extratropical teleconnection (Alexander et al., 2002), is widely researched in scientific communities of climate dynamics.

1.1.3 Dominant Large-Scale Dynamics in North Pacific

The ocean-atmosphere coupling in North Pacific is manifested in many large-scale dynamics, which are recognized to be dominant drivers for many anomalous phenomena of North Pacific. Therefore, it is of interest to review pertinent large-scale dynamics and scientific developments toward understanding these dynamics and their interactions in the tropical-extratropical teleconnection.

1.1.3.1 El Niño Southern Oscillation (ENSO)

The ENSO is the strongest interannual climate phenomenon in the tropical Pacific, presented as undulation between the unusual ocean surface warming (El Niño) and neutral and cooling (La Niña) in the equatorial Pacific with the coupled overlying pressure variation and atmospheric circulation shift (Southern Oscillation) (Bjerknes, 1966). Specifically, when the easterly trade wind in the tropical Pacific is punctuated by episodic westerly wind bursts, a warm anomaly appears as a result of the associated strong eastward flowing currents that carry warm surface waters from the western Pacific into the central Pacific (e.g. Chen et al., 2015a; Menkes et al., 2014). Another mechanism that is known to trigger El Niño is by exciting westward-propagating Rossby waves to the continental boundary that reflects as eastward-propagating, downwelling Kelvin waves, depressing the normal upwelling (e.g. Chen et al., 2015a; Menkes et al., 2014).

While these mechanisms explain the onset of the ENSO events and their variability within the tropical Pacific, it has been discussed that the ENSO can be initiated from extratropics through precursor dynamics. One of the mechanisms is identified by Vimont et al. (2003) as the seasonal footprinting mechanism, whereby the intrinsic atmospheric variability of the subtropics in winter with an expression of the southern lobe of the NPO pattern, the second leading sea level pressure (SLP) pattern over the North Pacific in winter (Linkin and Nigam, 2008), imparts a sea surface temperature (SST) "footprint" onto the ocean via changes in the surface heat fluxes. The SST footprint persists into summer, leading to a coupled zonal atmospheric circulation along the equator, and eventually produces the ENSO-like tropical variability in the following winter. The ENSO may also be promoted through the PMM (Chiang and Vimont, 2004), whereby the NPO-induced modulation of the trade winds leads to SST anomalies that propagate southwestward to the central equatorial Pacific via WES feedback mechanism (Xie, 1999) to promote the initiation of the ENSO.

As warming establishes along the equator, the atmospheric convection and heavy rainfall normally located in the western tropical Pacific migrates eastward to the central tropical Pacific, which leads to further weakening of the trade winds and further amplifying of the ocean surface warming. Once an El Niño event is fully developed, the delayed negative feedbacks involving ocean dynamics begin to dominate and eventually terminate the El Niño, returning the system to normal or sometimes overshooting into a cold La Niña phase (Battisti and Hirst, 1989; McPhaden, 2015; Schopf and Suarez, 1988).

The ENSO-related SST variabilities in the tropical Pacific and the associated shifting patterns of atmospheric convection and rainfall are recognized to be influential on

the climate dynamics of the North Pacific. Weare et al. (1976) and many following studies (e.g. Zhang et al., 1996) revealed that the tropical Pacific variability is connected to the North Pacific, as the dominant Empirical Orthogonal Functions (EOF) pattern of Pacific SST variability has anomalies of one sign in the central and eastern equatorial Pacific and along the coast of North America and anomalies of the opposite sign in the western equatorial Pacific and the Kuroshio Extension (KE) region. During El Niño, the equatorial Pacific is subject to the eastward-propagating, downwelling Kelvin waves and, as they reach to the continental boundary, continues poleward as coastal Kelvin waves along the North America west coast. However, these coastal Kelvin waves are confined within a narrow band from the coast. The ENSO events also influence remote regions through atmospheric pathways, whereby the deep atmospheric convection shift associated with the ENSO-related SST variabilities serves as an atmospheric bridge that links to the North Pacific ocean variability (Alexander et al., 2002).

1.1.3.2 Pacific Decadal Oscillation (PDO)

The PDO is defined as the leading EOF of monthly SST anomalies in North Pacific, characterized by a monopole spatial structure with a strong coherent signature along the coast (Mantua et al., 1997) and a decadal oscillation in the corresponding time series. Specifically, the spatial pattern of the PDO is similar to the ENSO, with a warm phase and a cold phase oscillating over decades and a corresponding fluctuation of position and strength of the Aleutian Low. During the PDO warm phase, the Aleutian Low intensifies and moves southeastward over the central North Pacific, causing SST to decrease in the central North Pacific and to increase in the eastern Pacific. The decrease of SST in the central North Pacific is associated with the advection of cool and dry air from

the north, the increases of westerly winds and ocean-to-atmosphere turbulent heat fluxes, and the strengthened equatorward advection of temperature by Ekman currents (Schneider and Cornuelle, 2005). The increase of SST in the eastern Pacific is associated with enhanced poleward winds. During the PDO cold phase, the Aleutian Low weakens and is centered over the Northwest Pacific, with warm SST anomalies in the central North Pacific and cold SST anomalies in the eastern regions.

As the understanding of mechanisms responsible for the PDO has been greatly improved over decades of scientific development, it is now well acknowledged that the PDO is, instead of a single physical mode and an inherent variability within the mid-latitude North Pacific, associated with a combination of various phenomena and linked to the tropical variability. (See Newman et al., 2016 for the review of candidate mechanisms). The mechanisms include: (1) Due to the coupling between the PDO and the overlying Aleutian Low, it has been discussed that the large-scale stochastic atmospheric forcing via intrinsic variability of the Aleutian Low is one of the primary drivers forcing the PDO variability. (2) Furthermore, because of the similarity between the spatial pattern of the PDO and the ENSO as well as the similar connection to the Aleutian Low variation, Zhang et al. (1997) describes the PDO as “the decadal ENSO-like variability” and Newman et al. (2003) suggests that the ENSO-related tropical variability serves as a remote forcing that drives the PDO via the “atmospheric bridge”. (3) Ocean memory via “reemergence mechanism” (Alexander and Deser, 1995) preserves the temperature anomalies that mix downward throughout the deep mixed layer from the previous winter, remain at depth insulated from the surface in summer and resurface in the following winter. This mechanism occurs over a large area of the North Pacific, contributes to preserving the

thermal anomalies from one winter to the other so that the North Pacific Ocean retains a similar warming/cooling state that helps maintaining the PDO (Alexander et al., 1999; Alexander et al., 2001). (4) Westward-propagating oceanic Rossby waves excited by anomalous wind stress curl modulates the stability of the KE jet by shifting the latitude and intensity of the fronts (Qiu, 2003; Qiu and Chen, 2010). These waves propagate through the KE region in approximately 3-10 years (Sasaki and Schneider, 2011) and, combined with the air-sea interaction, are thought to be contributing to the PDO on multidecadal scales (Miyasaka et al., 2014).

1.1.3.3 North Pacific Gyre Oscillation (NPGO)

The NPGO is defined as the second leading EOF of Sea Surface Height anomalies (SSHa), characterized by a pronounced dipole structure in the Northeast Pacific with opposite signs between the subpolar regions and the subtropical region separated by the North Pacific Current (Di Lorenzo et al., 2008). The NPGO is closely related to the "Victoria Mode" (Bond et al., 2003), the second leading EOF of SSTa, but exhibits more prominent low-frequency fluctuations (Di Lorenzo et al., 2008). The similarity between the spatial structure of the NPGO-related wind anomalies and the expression of the NPO has led to a conclusion that the NPGO is the oceanic expression of the atmospheric NPO (Di Lorenzo et al., 2008).

As defined, the NPGO has both a positive phase and a negative phase with a corresponding fluctuation of the NPO that collectively contributes to the decadal variability of the North Pacific. During the positive phase, the NPGO is expressed as negative SSHa in the subpolar regions and positive SSHa in the subtropical regions. The negative SSHa

induces positive Ekman pumping, which brings cold water from depth, whereas the positive SSHa leads to negative Ekman pumping, which pushes the surface warm water to depth. As a result, the SSTa structure, i.e., the Victoria Mode, of the NPGO is featured by the negative temperature anomalies within the subpolar regions and positive temperature anomalies within the subtropical regions. In terms of gyre circulation, the NPGO represents an intensification of the North Pacific Current, which bifurcates into a strengthening poleward and a strengthening equatorward propagation as it reaches to the coastal boundary, resulting in enhanced Alaskan Gyre and Subtropical Gyre along the coast. This is also supported by the corresponding wind forcing. Along the California Current system, the NPO-related equatorward wind forcing during the positive phase of the NPGO generates upwelling favorable conditions, whereas along the Alaskan current, the poleward wind forcing leads to downwelling favorable conditions.

Studies of the climate impact of the NPGO have started to emerge: Di Lorenzo et al. (2010) presents a hypothesis that the NPGO-mode in the North Pacific leads to warming in the central tropical Pacific via the atmospheric response near Hawaii, the center of the southern lobe of the NPO. Ceballos et al. (2009) presents the propagation from the NPGO signal in the eastern North Pacific to the quasi-regular oscillation of the KE jet in the western North Pacific via the westward propagation of Rossby wave. The propagation takes about 2.5 years from where the signal emerges to reach to the KE region. As the NPGO and PDO are the two most important modes in North Pacific, the NPGO and PDO can alternate in control leading to different oceanic expressions. Di Lorenzo and Mantua (2016) and Joh and Di Lorenzo (2017) show the coupling between the NPGO and PDO is an important dynamic interaction to prolonged Northeast Pacific marine heatwaves.

1.1.3.4 Pacific Meridional Mode (PMM)

The PMM (Chiang and Vimont, 2004) is a subtropical ocean-atmosphere coupling mode that initializes stochastically by the atmospheric fluctuation intrinsic to the mid-latitude, but has a deterministic component during the persistent process (Amaya, 2019). It is characterized by the southwestward propagation of the anomalous warming from Baja California to the central tropical Pacific via WES feedback mechanism (Xie, 1999) and linked to the initiation and development of the ENSO. Specifically, a weakening NPO in subtropics induces relaxation of the trade wind, leading to a reduction of evaporation and latent heat flux along the southwestward propagation band and, thus the expansion of warming toward the equator and the intensification of the meridional mode. Anderson et al. (2013) proposed a Trade Wind Charging (TWC) hypothesis, whereby the PMM-related wind stress curl anomalies in the western Pacific force the subsurface heat content in the tropical Pacific to propagate eastward along the thermocline as Kelvin waves, shoaling and reaching the eastern equatorial Pacific, setting the stage for the onset of an El Niño event.

1.1.3.5 Kuroshio Extension (KE)

The KE is the eastward-flowing extension of the poleward-propagating Kuroshio, separated from the Japan coast where the zonal integral of wind stress curl is zero, featured by its eastward-flowing inertial jet, large-amplitude meanders, abundant mesoscale eddy variability and the strongest air-sea interaction in the North Pacific (Yasuda et al., 1992). It is by now well recognized that the KE jet undergoes a decadal oscillation between a stable and an unstable dynamic state: In the stable state, the KE jet tends to have a more stabilized stationary path, larger eastward surface transport and greater zonal penetration,

accompanied by an enhanced southern recirculation gyre and a decreased regional eddy kinetic energy (Qiu, 2000, 2003; Qiu and Chen, 2005). This stable eastward-propagating KE jet tends to be originated from a more northerly latitudinal location (Qiu, 2000, 2003; Qiu and Chen, 2005). These tendencies reverse in the unstable state.

The dynamics contributing to the decadal oscillation of the KE jet are complex and various theories exist. These include: (1) The decadal oscillation of the KE jet is induced as the dynamical adjustment of the oceanic circulation to changes in wind stress curl according to the Sverdrup theory (Deser et al., 1999; Miller et al., 1998). The decadal variation of wind stress in the North Pacific asserts corresponding changes of Sverdrup transport in the interior of subtropical and subpolar gyres, which subsequently forces the compensation of the Sverdrup transport, the west boundary currents, and their downstream extensions, the KE, to adjust accordingly. (2) It is attributed to the baroclinic Rossby wave that is originated by the PDO-related or NPGO-related wind stress in the eastern North Pacific and that propagates and intensifies westward to the KE region (Ceballos et al., 2009; Qiu, 2003). Specifically, during the PDO warm phase, the Aleutian Low intensifies and shifts southeastward over the central North Pacific, causing strengthened Ekman divergence and hence generating negative SSH anomalies. The negative SSH anomalies propagate westward as baroclinic Rossby waves at a phase speed of ~0.04m/s (i.e., 3-4 years of propagation to the KE region) (Mizuno and White, 1983; Qiu, 2003) and weakens the KE jet and recirculation gyre into the unstable dynamic state. The opposite happens when the positive SSH anomalies induced by a weakened Aleutian Low in the central North Pacific propagates westward, which acts to strengthen the KE jet. Similarly, the NPGO-related wind stress curl in the eastern North Pacific induces the corresponding

baroclinic Rossby wave that propagates to the KE (Ceballos et al., 2009). (3) The KE jet interacts with the deeper or shallower bottom bathymetry to either stabilize or destabilize the KE jet (Qiu and Chen, 2005, 2010).

1.1.3.6 California Current System (CCS)

The CCS is among the most productive marine ecosystems, as the prevailing northerly wind along the coastal boundary drives offshore Ekman transport that is compensated by coastal upwelling. As such, cold water is brought up from depth along with rich nutrient, stimulating the growth of phytoplankton that forms the base of the marine food web (Carr, 2002; Chavez and Messie, 2009). However, the primary production varies substantially over years. Mechanisms driving the anomalous variation of the CCS have been studied.

It is well documented that the ENSO, through both oceanic and atmospheric teleconnections, is one of the most important drivers for the seasonal to interannual CCS variability. From oceanic pathway, during El Niño, westerly wind bursts induce downwelling Kelvin waves that propagates eastward to the continental boundary, causing poleward propagating coastally-trapped Kelvin waves along the North America west coast, deepening thermocline and suppressing upwelling (McPhaden, 1999). However, Gill (1982) argues that this oceanic pathway is confined within the distance of ~50km from the coast and reaches only poleward of 15^{o}N. Frischknecht et al. (2015) shows that the impact of tropical oceanic forcing dominates the variability in the nearshore region of the CCS. From atmospheric teleconnection, the deep atmospheric convection shifts to the central

equatorial Pacific and serves as an atmospheric bridge to impart on the Aleutian Low and drive ocean variability in the North Pacific (Alexander et al., 2002).

While the ENSO dominates the seasonal to interannual variability of the CCS, the mechanisms driving decadal variability are still unclear. As the PDO and the associated spatial structure of the Aleutian Low possess a monopole structure in the eastern North Pacific, it is argued that the positive PDO serves to weaken the CCS variability as a part of the subtropical gyre while strengthens the subpolar Alaskan gyre (Lavaniegos and Ohman, 2003; Trenberth and Hurrell, 1994). The opposite is true for strengthening the CCS variability and weakening the subpolar Alaskan gyre. In the meantime, the NPGO and the associated NPO structure have pronounced dipole structures, which coincide with the subpolar and subtropical interior and serve to strengthen (weaken) both the subpolar and subtropical variability during the positive (negative) phase of the NPGO (Di Lorenzo et al., 2008). As such, the interaction of the PDO and NPGO could collectively contribute to enhance or reduce the CCS variability (Bond et al., 2003; Di Lorenzo et al., 2008).

However, nearshore processes of the CCS are more complex and combined with higher frequency variability. Due to the fact that the shoreline orientation and the local bathymetry rapidly varies along the coast of the CCS, the dynamic interaction between winds, sub-mesoscale eddies, surface and internal waves, mixing and surf zone processes can lead to complex three-dimensional local circulation in the nearshore CCS region.

1.1.4 Impacts on Marine Ecosystem Services and Operations

Climate variability has significant influence on the marine ecosystem services and operations, primarily through the “double integration hypothesis”, such that ocean serves

as an integrator that absorbs the variability of stochastic atmosphere and persists to affect the marine ecosystem (atmosphere – ocean – ecosystem) (Di Lorenzo and Ohman, 2013). Specifically, SST and mixed layer variability are the most important ocean variables involved in changing the ecological conditions, such as nutrient supply or primary production (Miller and Schneider, 2000).

Atmosphere and ocean coupling dynamics responsible for the variability of these ocean indicators are different along the eastern boundary of the North Pacific compared with the western boundary. Along the eastern boundary, these ocean indicators are largely driven by net heat transport from the atmosphere and ocean processes such as local coastal upwelling and horizontal advection (Di Lorenzo et al., 2013a; Miller and Schneider, 2000). Large-scale climate dynamics such as the remote ENSO influence from the tropics, the Aleutian Low coupled with the PDO, the NPO coupled with the NPGO, downstream of the KE exert their influence on the local coastal upwelling and horizontal advection through modulating the subpolar and subtropical gyre circulation and the corresponding vertical transport response (Di Lorenzo et al., 2013a; Jacox et al., 2020b). Along the western boundary, the intensive air-sea coupling is featured by decadal oscillation of the KE jet, as the convergence and extension of the western boundary return flow of subpolar and subtropical gyre circulation. The Aleutian Low coupled with the PDO and the NPO coupled with the NPGO modulates the KE jet oscillation through westward propagation of the baroclinic Rossby wave generated from the eastern Pacific (e.g. Ceballos et al., 2009; Qiu and Chen, 2010).

Ecosystem response to the climate variability is categorized into two primary types, based on whether a “regime shift” of marine species is directly linked to a climate driver

or the impact on a specie is mediated by trophic relationship (e.g. Overland et al., 2010). An example of the first type is sardine population in the Santa Barbara Basin, as the warmer temperatures are preferred for spawning and growth of sardine along the eastern Pacific boundary (Lluchbelda et al., 1992; Miller and Schneider, 2000). The latter one is drawn from a hypothesis that climate variability exerts controls on lower-trophic phytoplankton and zooplankton that eventually affects the upper trophic marine species, named as "bottom-up control" (Di Lorenzo et al., 2013b; Ware and Thomson, 2005).

While climate variability exerts influence on the marine ecosystem, it also inevitably affects relevant services and operations for fisheries, aquaculture, shipping and scientific in-situ measurement. Therefore, it is of vital importance to understand air-sea coupling variability and climate extremes to make proactive decisions and to better adapt to the future variability. For a timescale of days, understanding the coastal ocean circulation in response to instant wind forcing and heat fluxes helps guide the scientific in-situ measurement to strategically plan for the sampling sites. For a seasonal to interannual timescale, understanding the marine species response to climate variability helps fisheries and aquaculture to adapt farming to the favorable conditions.

1.2 Predictability of the North Pacific from Diurnal to Seasonal Timescale

Ocean predictability of the North Pacific has been a subject of interest over decades, as achieving adequate predictability skill at temporal and spatial scales is of vital importance for navigation guidance, marine ecosystem balance, and decision planning for fisheries and aquaculture (Jacox et al., 2020b; Stock et al., 2015). How predictable the oceanic processes of North Pacific are and how much of the predictability in North Pacific

derives from mechanisms intrinsic to North Pacific versus remotely forced by the tropics is still an ongoing investigation.

Dominant mechanisms contributing to the predictability of the North Pacific basin vary depending on which spatial and temporal scales that the mechanism exerts on. The ENSO has been identified as a dominant source of predictability in the tropical Pacific and largely contributes to predictability along the eastern Pacific boundary from seasonal to interannual time scales (Jacox et al., 2019a; Quan et al., 2006). The ocean memory via reemergence of subsurface temperature anomalies stored below the upper mix layer from year to year is also considered an important source of predictability to the Northeast Pacific, as the thermal inertia preserved in the mixed layer from the previous winter resurfaces in the following winter (Alexander et al., 1999). The PDO coupled with the Aleutian Low and the NPGO coupled with the NPO are the two most dominant large-scale climate dynamics in the North Pacific (Di Lorenzo et al., 2008; Mantua et al., 1997) and might also be a source of predictability on decadal time scales. These large-scale climate dynamics are most prominent in the eastern North Pacific and are found to modulate the decadal oscillation of the KE through the generation of baroclinic Rossby wave in the eastern North Pacific that propagates westward (Ceballos et al., 2009; Qiu, 2003; Schneider and Miller, 2001) and potentially contribute to the predictability in the western North Pacific. Predictability of the KE, as a convergence region of the subpolar and subtropical gyre circulation, and predictability along the western boundary are therefore subject to the strength and positions of the gyre circulation (Qiu and Chen, 2010). Although these climate dynamics exert their influence on a decadal time scale, they serve as a sustained warming

or cooling source that affects the oceanic predictability on higher frequency time scales (Dias et al., 2019).

While the predictability of the Pacific basin has been investigated in many previous studies, less is understood of the predictability along the North Pacific coastline. It is commonly acknowledged that the ENSO exerts its influence on the North Pacific via an atmospheric bridge and oceanic teleconnections (e.g. Capotondi et al., 2019 and reference therein). The atmospheric bridge with information from the remote tropics affects the oceanic processes mainly through net surface heat flux and wind-driven Ekman transport (Alexander et al., 2002), which are equally prominent along the coastal boundary of the eastern Pacific (Jacox et al., 2019a). Oceanic teleconnection via coastal Kelvin waves from the ENSO has influence on the eastern Pacific boundary within a narrow band from coastline and does not extend to the high latitude of the North Pacific (Frischknecht et al., 2015; Newman et al., 2016). Besides the ENSO, the PDO and NPGO might also affect the predictability of the eastern Pacific boundary by modulating the subtropical and subpolar gyre. Specifically, the PDO influence along the coastline is featured by strengthening one gyre but weakening the other, while the NPGO affects the gyre circulations by simultaneous strengthening or weakening both gyres (Di Lorenzo et al., 2008). Still, the predictability along the eastern Pacific boundary is not fully exploited in the global climate model, as coastal upwelling as well as Kelvin waves are not properly resolved due to the coarse resolution. Moreover, these large-scale climate dynamics do not explain the high frequency variability (diurnal scale), as predictability of diurnal scale is linked to tidal processes, instantaneous oceanic response to the anomalous wind that deviates from the mean atmospheric circulation, and other nonlinear processes.

Several studies explored the predictability along the western boundary of Atlantic, while studies of the western Pacific boundary focused on the predictability of the KE. As western boundary currents share some common characteristics, specifically as the fast and narrow returning flow of the Sverdrup transport in the ocean interior (Miller et al., 1998), the findings of the predictability along the western boundary of the Atlantic have some reference values for the Pacific. Seasonal predictability along the western return flow was found to be at most comparable to the persistence forecast (Hervieux et al., 2019). These limited forecast skills were attributed to the poorly resolved continental shelf and the unrealistically laminar flow simulated by the global forecast systems (Stock et al., 2015). As a result, the Gulf Stream in the Atlantic, analogous to the Kuroshio current in the Pacific, extended too far north before separating from the eastern U.S. continental shelf (Hervieux et al., 2019), leading to inaccurate oceanic prediction. These findings suggest that the predictability along the western boundary of the Pacific might not be as good as the predictability along the eastern boundary and that the poorer seasonal predictability skill might be attributed to the unresolved continental shelf and the inaccurate representation of the western boundary flow.

1.3 Motivation for the Present Study

Predictability of the North Pacific, especially climate extremes and coastal variability, and the source mechanisms contributing to the predictability are still not clear. Specifically, this thesis aims to target the following questions in the field of predictability studies: (1) Are the Northeast Pacific marine heatwaves intrinsically unpredictable or a recurrent phenomenon of the Pacific dynamics? What is the role of tropical-extratropical interaction in shaping the progression of Northeast Pacific marine heatwaves? (2) How predictable the

North Pacific coastal waters are, especially the ocean indicators important to the coastal ecosystem? How does the tropical and extratropical forcing contribute to the predictability of these ocean indicators? (3) For a regional ocean forecast system, predictability skill relies on the appropriate formulation of ocean circulation, realistic initial forcings and lateral boundary conditions. To the extent that a model is a good surrogate for nature, understanding the sensitivity and response of forecast to forcings becomes crucial for a credible prediction to be a useful assessment. In regional climate models, it remains to be investigated for how much of the ocean predictability is controlled by initial forcing versus boundary forcings.

CHAPTER 2. THE CONTINUUM OF NORTHEAST PACIFIC MARINE HEATWAVES LINKED TO THE TROPICAL PACIFIC

The content of this chapter was published in:

Xu, T., M. Newman, A. Capotondi, and E. Di Lorenzo (2021), The Continuum of Northeast Pacific Marine Heatwaves and Their Relationship to the Tropical Pacific, *Geophysical Research Letters*, *48*(2), 2020GL090661, doi:https://doi.org/10.1029/2020GL090661.

The 2013-2015 multi-year Northeast Pacific marine heatwave (MHW) is considered a record-breaking event. It remains unclear if this event was an exception or merely the most pronounced of a group of similar events, and if its intensity and multi-year duration was driven by internal extratropical processes or intensified by the tropical Pacific influence. This chapter aims to (1) analyze the statistical behaviors of Northeast Pacific MHWs within the observed ERSST.v3 dataset over the 1950-2019 period, (2) develop a Pacific Linear Inverse Model (LIM) (Penland and Sardeshmukh, 1995) to generate a large ensemble simulation of the North Pacific and tropics, which provides a greater range of MHW expressions than the observational record alone. Both observed and simulated MHWs of various intensities and durations are identified to understand the characteristics and progression of the MHWs and to analyze the role of extratropical internal variability versus the remote influence of tropical Pacific in the progression of these events.

2.1 Introduction

Prolonged marine heatwaves (MHWs) in the Northeast Pacific, defined as extended periods of anomalously warm ocean temperatures, have been brought to the attention of

many scientists due to their unique progression patterns, extreme amplitudes and durations, and severe ecological impacts (e.g. Bond et al., 2015; Di Lorenzo and Mantua, 2016; Frolicher and Laufkotter, 2018; Holbrook et al., 2019). [See section 1.1.1 for a detailed introduction of Northeast Pacific MHWs, or see Holbrook et al. (2020) and Oliver et al. (2021) for reviews on current understanding of MHWs].

Are Northeast Pacific MHWs predictable? Away from regions of strong currents, midlatitude extratropical sea surface temperature (SST) anomalies are thought to be largely driven by unpredictable weather noise (Frankignoul and Hasselmann, 1977; Hasselmann, 1976), which the ocean serves to integrate and thereby redden (Frankignoul and Reynolds, 1983). Consistent with the stochastically-forced view of North Pacific Ocean mixed layer dynamics, studies have found that forcing from a resilient Northeast Pacific atmospheric ridge initiated the 2013-2015 event (Bond et al., 2015; Swain et al., 2014), so perhaps its start was unpredictable beyond the atmospheric forcing time scale. On the other hand, the MHW's subsequent multi-year persistence has been linked to tropical teleconnections (Di Lorenzo and Mantua, 2016) emanating from the central and western tropical Pacific (Capotondi et al., 2019; Hartmann, 2015), suggesting the presence of a deterministic, potentially predictable component.

Moreover, while over the past 70 years no other historical Northeast Pacific warm event had such record-breaking warming nor persisted so long as the 2013-2015 event (over 700 days in Hobday et al. (2018)), other intense warm events have occurred before and since (e.g. Amaya et al., 2016; Amaya et al., 2020; Oliver et al., 2018). In fact, prolonged Northeast Pacific warm events may be said to occur over a range of intensities and durations (Scannell et al., 2016). However, the short observational record provides

only a limited set of historical realizations of the MHWs that may not be adequate either to represent the full spectrum of possible MHWs or to entirely differentiate the behavior of long-lasting and high-intensity MHWs from short-lived and moderate-warming ones.

We suggest that Northeast Pacific MHWs may be viewed as a recurrent phenomenon of the Pacific basin involving large-scale teleconnection dynamics, with the 2013-2015 MHW being a particularly strong realization within a continuum of MHW events. In this view, MHWs are neither unprecedented nor intrinsically unpredictable in their dynamical evolutions, although some properties like the maximum amplitude may be (Hu et al., 2017). To demonstrate this point, we evaluate Northeast Pacific MHWs in the observational record by diagnosing a Pacific-basin Linear Inverse Model (LIM) (Penland and Sardeshmukh, 1995), an empirical dynamical model derived from observed anomaly covariances. The LIM is attractive for this purpose since it is able to capture observed climate anomaly evolution over extended periods (for example, its seasonal forecasts are generally comparable with state-of-the-art multi-model operational forecast ensembles; e.g. Newman and Sardeshmukh, 2017), yet its low dimensionality allows generation of long climate simulations suitable for hypothesis testing (e.g. Capotondi and Sardeshmukh, 2017; Newman et al., 2011b). Here, we develop a LIM to produce a large ensemble simulation of tropical and North Pacific SST anomalies, so that we may evaluate details of observed MHW evolution against the much larger sample of simulated MHW events.

2.2 Data and Methods

2.2.1 Data

Monthly SST data from the 1950-2019 period were obtained from the National Oceanic and Atmospheric Administration (NOAA) Extended Reconstruction SST, version 3 (ERSST.v3b; Smith et al. (2008)). SST anomalies (SSTa) were constructed by temporally smoothing SST fields with a 3-month running mean, removing the monthly climatology, and linearly detrending.

2.2.2 Linear Inverse Model

When the nonlinear portion of climate dynamics decorrelates much faster than the linear dynamics, we may approximate the evolution of a suitably-averaged climate anomaly state vector $\mathbf{x}(t)$ as

$$\frac{\mathrm{d}\mathbf{x}}{\mathrm{d}t} = \mathbf{L}\mathbf{x} + \boldsymbol{\xi}, \tag{1}$$

(Hasselmann, 1976; Penland and Sardeshmukh, 1995), where $\mathbf{L}$ is a linear dynamical operator and $\boldsymbol{\xi}$ is a vector of temporally white noise. From (1), the most probable state of $\mathbf{x}$ at $t + \tau$ is

$$\hat{\mathbf{x}}(t+\tau) = \mathbf{G}(\tau)\mathbf{x}(t) = \exp(\mathbf{L}\tau)\,\mathbf{x}(t), \tag{2}$$

which therefore represents the ensemble-mean forecast at lead τ.

A LIM (Penland and Matrosova, 1994; Penland and Sardeshmukh, 1995) empirically determines (1) from observed covariances. In this study, we constructed a LIM where $\mathbf{x}(t)$ consisted of the 19 leading principal components (PCs) of Pacific region (110°E to 60°W, 20°S to 60°N) SSTa, which explain 88.7% of the variance. This SST-only

model can capture the dominant seasonal climate dynamics (Penland and Sardeshmukh, 1995), although fully capturing interannual-to-decadal variability requires including some measure of upper ocean heat content as well (e.g. Newman et al., 2011a). For example, we compared the lag-covariance statistics predicted by the LIM to those derived from observations, over lags ranging from 3-12 months (Figure 1). This "tau-test" (Penland and Sardeshmukh, 1995) showed that the LIM's linear approximation is valid over several multiples of the 3-month training lag.

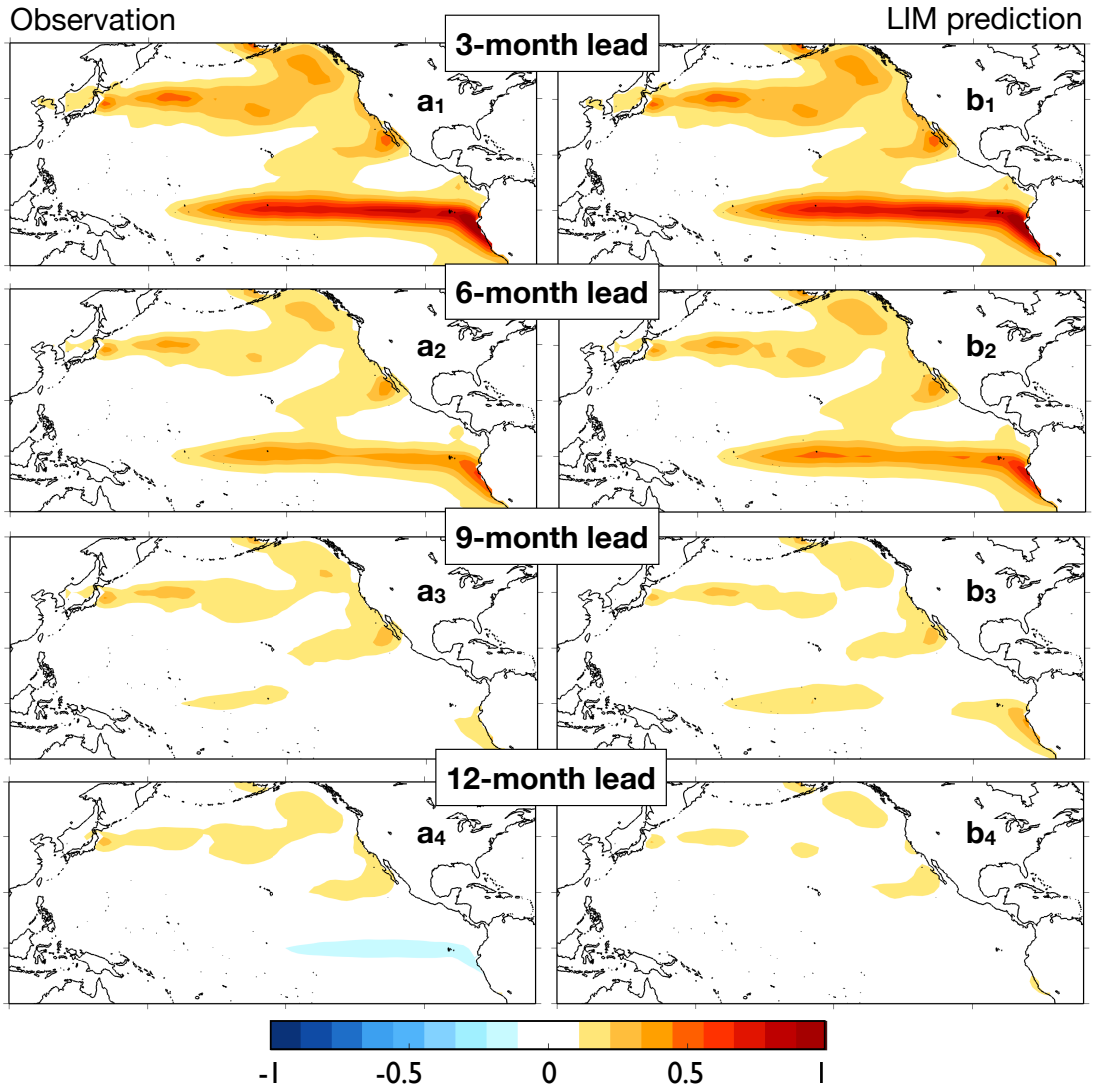

Figure 1. Lag covariance of (a_1-a_4) observation and (b_1-b_4) LIM prediction for 3-, 6-, 9-, 12-month lead. Units are in ($^oC^2$).

In addition to being used as a skillful forecast model (2), the LIM may be run in simulation mode by integrating (1) forwards in time, driven by white noise forcing whose spatial structure is determined from the noise covariance $\mathbf{Q} = < \boldsymbol{\xi}\boldsymbol{\xi}^{\mathrm{T}} > \mathrm{d}t$ of the stationary Fluctuation-Dissipation relationship (Penland and Matrosova, 1994)

$$\mathbf{L} < \mathbf{x}\mathbf{x}^{\mathrm{T}} > + < \mathbf{x}\mathbf{x}^{\mathrm{T}} > \mathbf{L}^{\mathrm{T}} + \mathbf{Q} = 0. \tag{3}$$

The LIM simulation is carried out following Penland and Matrosova (1994), which is a two-step integration of the white noise forcing following

$$\mathbf{y}(t + \Delta) = \mathbf{y}(t) + \mathbf{L}\,\mathbf{y}(t)\,\Delta + \mathbf{V}_{\mathrm{k}}\sqrt{\boldsymbol{\Lambda}_k \Delta}\,\mathbf{n}_k, \tag{4}$$

$$\mathbf{x}(t + \Delta/2) = \{\mathbf{y}(t) + \mathbf{y}(t + \Delta)\}/2 \tag{5}$$

where $\mathbf{y}$ is an intermediate vector, the scalar Δ is the incremental time step, $\mathbf{V}$ represents the eigenvectors of $\mathbf{Q}$ and $\boldsymbol{\Lambda}$ represents a diagonal matrix containing the eigenvalues of $\mathbf{Q}$ such that $\mathbf{Q} = \mathbf{V}\boldsymbol{\Lambda}\mathbf{V}^{\mathrm{T}}$. Only the non-negative eigenvalues of $\mathbf{Q}$ and their corresponding eigenvectors are incorporated in the stochastic simulation, which is denoted as $\boldsymbol{\Lambda}_{\mathrm{k}}$ and $\mathbf{V}_{\mathrm{k}}$. If negative eigenvalues exist, the non-negative eigenvalues are proportionately rescaled to maintain the same variance (i.e., the trace of $\mathbf{Q}$ is unchanged). The k-dimensional vector $\mathbf{n}_k$ of independent Gaussian deviates, each having unit variance, must be generated at each time step. Here, with a small Δ of 16 hours, we integrated the randomly perturbed noise forcing forward for a length of 140,000 years and retained the monthly data, which is then separated into 2000-member ensemble of 70-yr long segments matching the length of the observed record we examined.

2.3 Observed and LIM-Simulated Northeast Pacific Marine Heatwaves

2.3.1 Composite Analysis of Observed Northeast Pacific Marine Heatwaves

To diagnose Northeast Pacific MHWs, including their observed and simulated evolution, we defined a Northeast Pacific SSTa index (Figure 2a) by averaging SSTa within a representative region (150°W to 135°W, 35°N to 46°N; inset in Figure 2a). Following previous studies of oceanic (Hobday et al., 2016; Holbrook et al., 2019; Scannell et al., 2016) and atmospheric (e.g. Dole and Gordon, 1983; Miller et al., 2020) persistent anomalies, abnormally intense and persistent warm events were identified as occurring when the Northeast Pacific index exceeded a given temperature amplitude threshold ("intensity") and persisted above it for a given length of time ("duration"). Defining MHW events using a $\mathbf{1}\boldsymbol{\sigma}$ amplitude threshold and 5 months duration, we found 12 discrete MHW events over the past 70 years (gray bars in Figure 2a; Table 1).

Of course, this definition of an MHW event is not unique. More generally, as in the aforementioned studies, we calculated the frequency of abnormally warm events defined by varying intensity and duration thresholds. The resulting Intensity-Duration-Frequency (IDF) plot (Figure 2b) shows how MHW events are observed less frequently for increased intensity or duration thresholds. For example, extremely warm events persisting for a short period are about as frequent as more prolonged but weaker events. The 1σ-intensity and 5-month-duration criteria (blue circle in Figure 2b) provide a representative set of observed MHW events for our analysis.

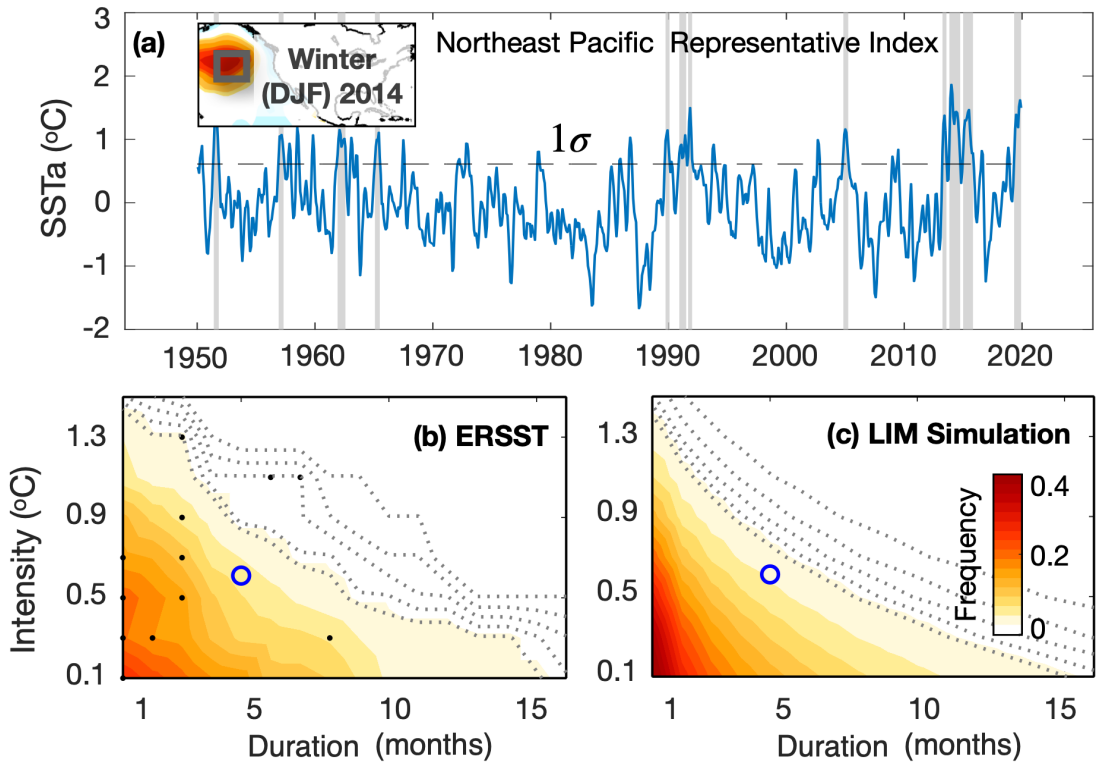

Figure 2. SSTa time series within the Northeast Pacific region and its corresponding frequency statistics as a function of intensity and duration. (a) Northeast Pacific index, defined as the spatially-averaged SSTa within the gray box region in the insert (overlaid on the winter 2014 SSTa). Gray bars mark each event that both exceeded one standard deviation (1σ) and persisted for ≥5 months. (b, c) Northeast Pacific MHW Intensity-Duration-Frequency (IDF) plot, derived from the (b) observed and (c) LIM-simulated Northeast Pacific time series, obtained by calculating the number of events exceeding each intensity and duration threshold pairs. In (b), dots mark those observed values significantly different from the LIM simulation (at a 95% significance level).

Table 1. Information for historical Northeast Pacific MHW events that exceed 1 σ and persist ⩾5 months in the observed Northeast Pacific index.

#	Start Date	End Date	Duration (months)
1	1951/06	1951/11	6
2	1956/12	1957/05	6
3	1961/12	1962/08	9
4	1965/02	1965/07	6
5	1989/10	1990/02	5
6	1990/12	1991/07	8
7	1991/09	1992/01	5
8	2004/11	2005/04	6
9	2013/04	2013/08	5
10	2013/11	2014/10	12
11	2015/01	2015/11	11
12	2019/05	2019/12	8

We also examined sensitivity to the region chosen to define the Northeast Pacific index. The mean duration of abnormally warm events ($\geq 1\sigma$) at each location within Northeast Pacific was around 4 to 6 months (Figure 3). [In contrast, the mean duration in the central and eastern equatorial Pacific region was around 6 to 8 months, typical of El Niño.] That is, the mean persistence of abnormally warm events in Northeast Pacific is not too sensitive to the location, so MHW duration may be represented using our Northeast Pacific index.

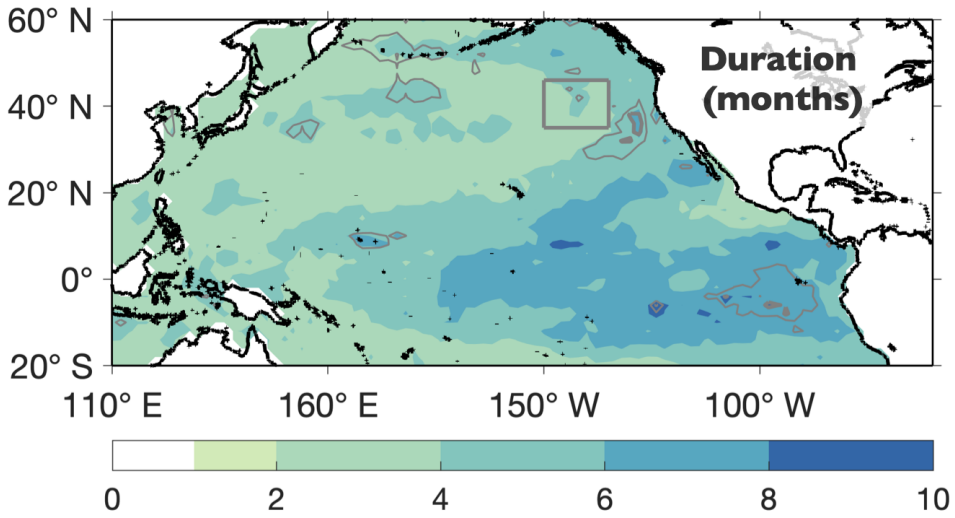

Figure 3. Average duration (in months) of warm events exceeding 1σ calculated at each grid point of our domain. Shading denotes the average duration from observations. Results of the LIM simulation are generally similar except in the regions enclosed by gray contours, where the observed duration is ±1month significantly different from the LIM simulation at a 95% significance level.

The composite evolution, including leads and lags, of the 12 observed Northeast Pacific MHWs identified in Figure 2a is shown in Figure 4. At $t = -12$ months (Figure 4a), the composite spatial pattern shows warm temperature anomalies extending zonally along 40ºN within the central North Pacific Current region. These warm anomalies then extended eastward at $t = -6$ months (Figure 4b), intensifying until the Northeast Pacific index reached the 1σ threshold at $t = 0$ months (Figure 4c). While the Northeast Pacific warming persisted at $t = +6$ months (Figure 4d), El Niño conditions developed in the tropics, perhaps linked to the Northeast Pacific warming through the North Pacific Meridional Mode (NPMM) (Chiang and Vimont, 2004) that is often identified as an El Niño precursor (Capotondi and Sardeshmukh, 2015; Larson and Kirtman, 2014). At $t = +12$ months (Figure 4e), while El Niño persisted, the Northeast Pacific warming spread along the US West Coast, consistent with atmospheric teleconnections from the tropics (Alexander et al., 2002; Di Lorenzo and Mantua, 2016).

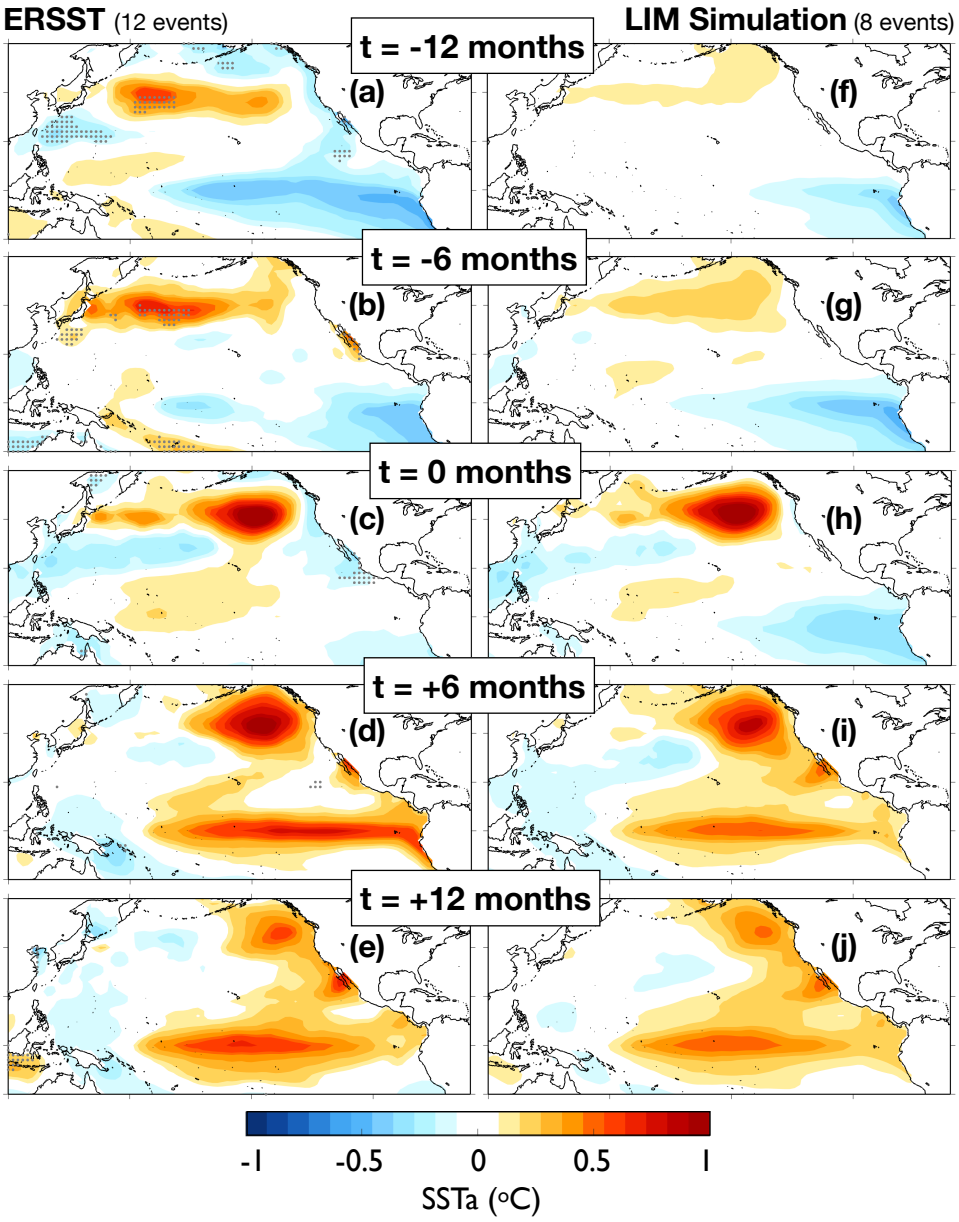

Figure 4. Composite Northeast Pacific MHW evolution based on (a-e) observations and (f-j) LIM simulation. The composite at t=0 month is calculated by averaging SSTa of all events at the time when the Northeast Pacific index first exceeds 1σ and subsequently persists for at least five months. This pair of intensity and duration is also indicated by the blue circles in Figure 2b and c. Other maps represent the leading and lagging composites at t=$\pm$6 months and t=$\pm$12 months. Gray dots in (a-e) show where the observed composite amplitude is significantly different from the LIM simulation at a 95% significance level. Number of events inserted on the top represents mean events per 70 years.

2.3.2 Comparison to the LIM Simulation

In this section, we evaluate how well these aspects of observed MHWs are reproduced within the LIM simulation. The IDF plot derived from the LIM simulated Northeast Pacific time series (Figure 2c) matches the observed IDF plot (Figure 2b), except for short (1~3 month) duration MHWs where the LIM event frequencies were 95% significantly different from the observed (black dots in Figure 2b). The significance test was carried out by (1) calculating the IDF of each ensemble to obtain the 2.5% as the lower bound and 97.5% as the upper bound at each intensity-duration pair, (2) determining whether the observed IDF at the corresponding intensity-duration pair lies outside the confidence interval. If so, there is a significant difference between the observation and the LIM simulation.

Similarly, the mean duration of abnormally warm events ($\geq 1\sigma$) within the LIM simulation generally agrees well with observations, except for some small regions in the eastern equatorial Pacific, northwestern subtropics and northwestern Pacific (gray contours in Figure 3). In sum, the LIM simulation reproduces the statistics of observed MHWs over a continuum of intensities and durations, implying that it contains a full range of expression of MHWs consistent with observations.

Composite evolution of the LIM-simulated MHWs (Figure 4f-j) also matches well with the observed evolution (Figure 4a-e). There are virtually no statistically significant differences between the observed and LIM composites from $t = 0$-12 months. The observed and LIM composites also have similar patterns prior to $t = 0$ months, but LIM amplitudes are weaker than observed, significantly so in the Northwest Pacific (gray dots

in Figure 4a-e). Overall, the large ensemble LIM simulation contained on average 8 MHW events per 70 years, compared to 12 historical events over the past 70 years. This suggests that MHWs as a phenomenon share some common features in their evolution and that these prolonged and spatially evolving warm events are a recurrent feature of the Pacific basin.

2.4 Characteristics Linked to the Tropical Pacific

We next explore the sensitivity of LIM composite MHWs to different threshold criteria, in order to help understand extratropical versus tropical impacts on MHW intensity and duration. This is done by comparing composites where we vary one threshold while fixing the other.

We first analyzed the sensitivity to duration, keeping the intensity fixed at 1σ (Figure 5). The PDF of durations from the simulated MHW events exceeding the 1σ intensity threshold and persisting at least five months (Figure 5a) shows a notable fraction of long-lived MHWs (up to 53 months) in the LIM simulation. From these simulated events, composite MHW evolution was determined for subsets with durations ≥ 6 months (Figure 6a), ≥ 12 months (Figure 6b), and ≥ 18 months (Figure 6c). We found three key differences between longer and shorter duration MHW events: (1) while the MHW onset intensity was similar regardless of the duration thresholds, the maximum MHW amplitude was greater for longer-lasting MHWs, (2) the initial equatorial Pacific cold anomalies were stronger and persisted longer, and (3) the central Pacific El Niño was slower to develop, reaching greater peak amplitude at later lags (cf. t=+12 m for Figure 6b with t=+18 m for Figure 6c). Also, as the duration threshold was increased, the composite evolution became increasingly similar to the 2013-2015 MHW event.

The relationship between Northeast Pacific MHW evolution and ENSO development is seen by plotting the composite evolution of the Northeast Pacific index against the corresponding Niño 3.4 index (Figure 5b). Each curve shows, for a different duration threshold indicated by the color shading, the concurrent evolution of the Northeast Pacific indices and Niño 3.4 indices, with time running in a counter-clockwise direction from -12 to 24 months. Four distinctive phases of each MHW event are evident: (1) Initial equatorial Pacific cold anomalies persist as the MHW rapidly strengthens to first reach its 1σ threshold value at t=0 (open circles); (2) Subsequently, equatorial Pacific SSTa develop into El Niño conditions, with relatively little change in MHW amplitude; (3) With El Niño remaining strong or even amplifying, the MHW gradually weakens; (4) The El Niño fades in the equatorial Pacific. What distinguishes these curves from each other is that the longer duration events start with colder Niño3.4 values, and (more slowly) develop warmer Niño3.4 values, than the shorter duration events, despite identical MHW intensity at t=0. Overall, these results suggest a key tropical role in driving more persistent MHWs (Joh and Di Lorenzo, 2017; Liguori and Di Lorenzo, 2018), corroborating previous studies emphasizing the impact of tropical teleconnections on shaping the 2013-2015 MHW event (Capotondi et al., 2019; Di Lorenzo and Mantua, 2016).

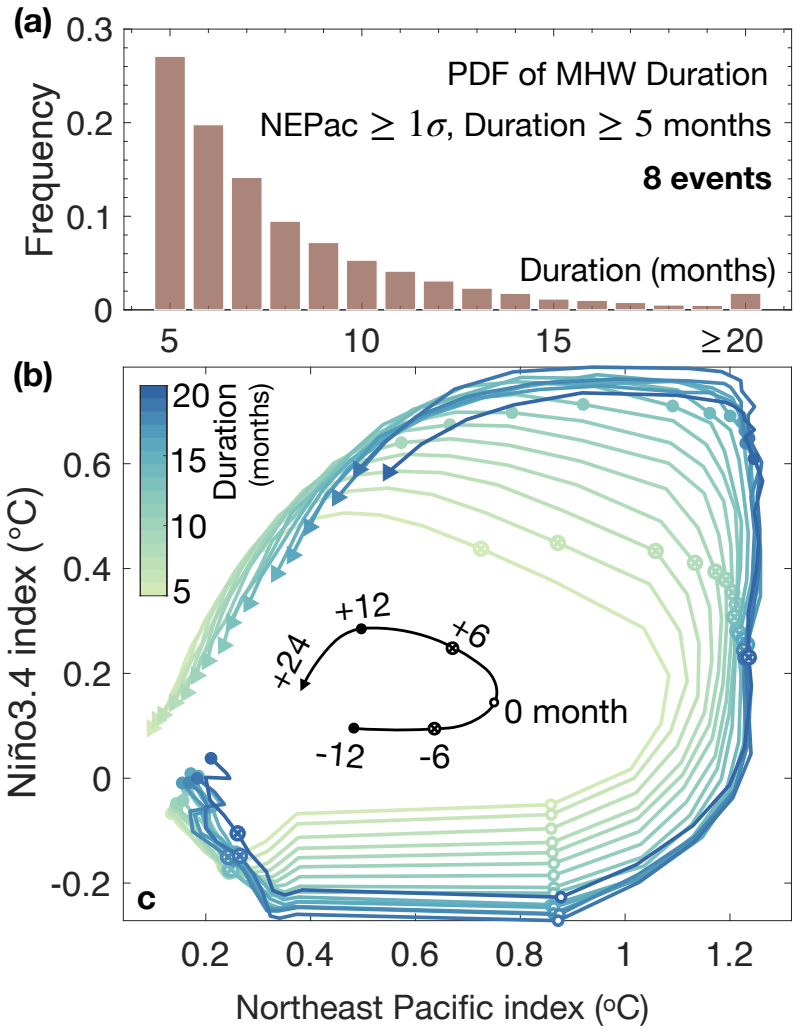

Figure 5. Histogram and evolution of LIM-simulated Niño 3.4 index as a function of the Northeast Pacific index with varying duration thresholds, for fixed intensity threshold 1σ. (a) Probability distribution function (PDF) of durations for MHW events exceeding an intensity of 1σ, starting at 5-month duration. Number of events inserted represents mean events per 70 years. (b) Niño 3.4 index as a function of Northeast Pacific index during the composite evolution of Northeast Pacific MHWs, from -12 months to +24 months, where each line represents varying duration thresholds ranging from 5 months (light green) to 20 months (blue).

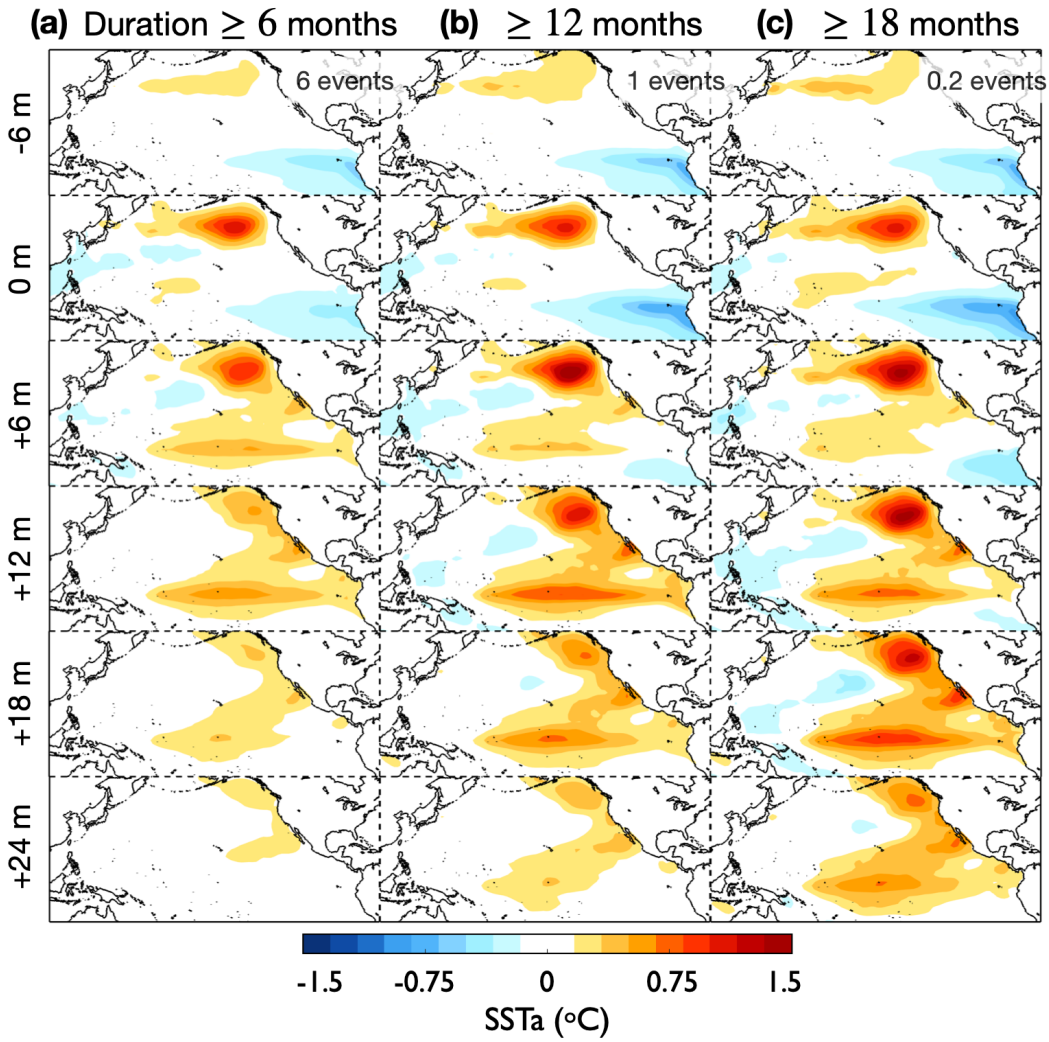

Figure 6. Evolution of LIM-simulated Northeast Pacific MHW composites with varying duration thresholds: (a) 6 months, (b) 12 months, (c) 18 months, for fixed intensity threshold 1σ. Composite evolution from 6 months before to 24 months after the MHW initiation. Number of events inserted on top represents mean events per 70 years.

We then repeated the analysis, but varied intensity thresholds for a fixed 6-month duration threshold (Figure 7 and Figure 8). The PDF of intensities from the simulated MHW events that persisted for $\geq$ 6-months duration and had an intensity $\geq 1\sigma$ (Figure 7a) shows that the LIM simulation generated MHWs with amplitudes even greater than observed in the past 70 years (cf. Figure 2a). Composite MHW evolution was then determined for subsets with intensities $\geq 5/3\sigma$ (Figure 8a), $\geq 2\sigma$ (Figure 8b), and $\geq 7/3\sigma$ (Figure 8c). Unlike the results for increased event duration, there was little difference in the evolving patterns of weaker and stronger events apart from an overall increased amplitude throughout the Northeast Pacific. In particular, the initial cold anomalies in the equatorial Pacific were almost identical (first and second row of Figure 8), and the maximum El Niño warming occurred at about the same time (third and fourth row of Figure 8), albeit with generally greater amplitude for higher MHW intensity thresholds. However, this relative tropical magnitude increase was less than the relative Northeast Pacific intensity increase. Similarly, the Northeast Pacific versus Niño 3.4 indices evolution curves (Figure 7b) demonstrate that increased MHW intensity depended much more on the initial Northeast Pacific value than on the initial Niño 3.4 value. Overall, these results suggest that MHW intensity may be more strongly affected by variability intrinsic to the extratropics than by ENSO teleconnections.

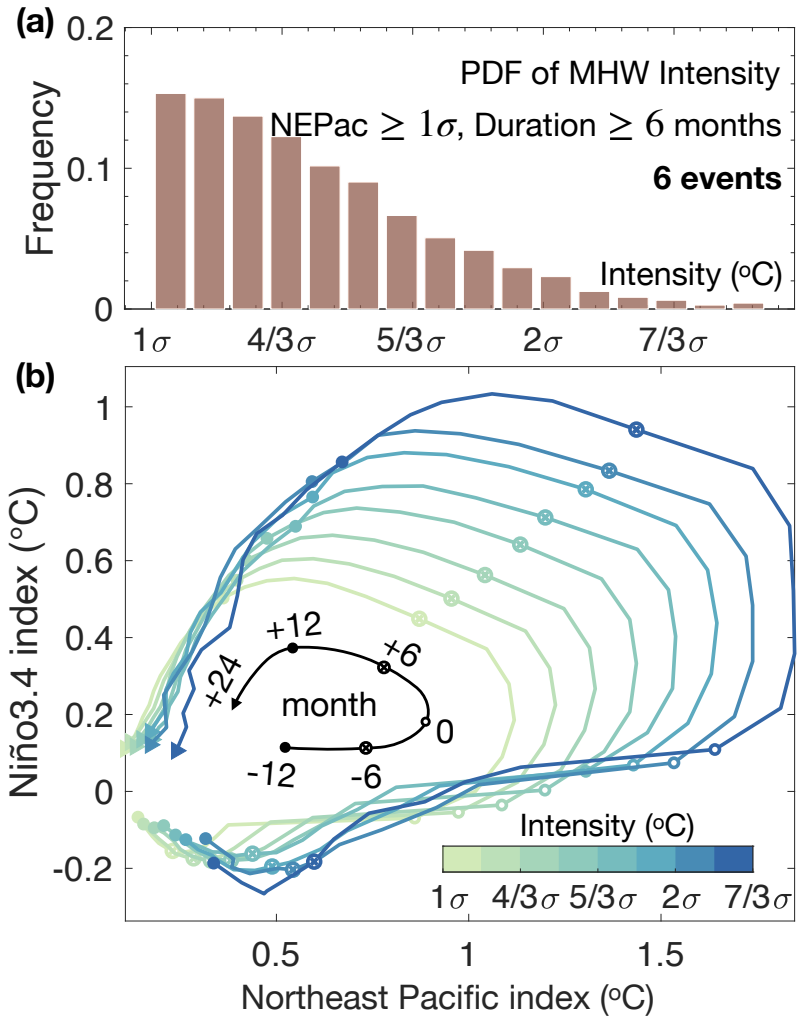

Figure 7. Same as Figure 5, except that the intensity threshold is varied while the duration threshold is fixed at 6 months.

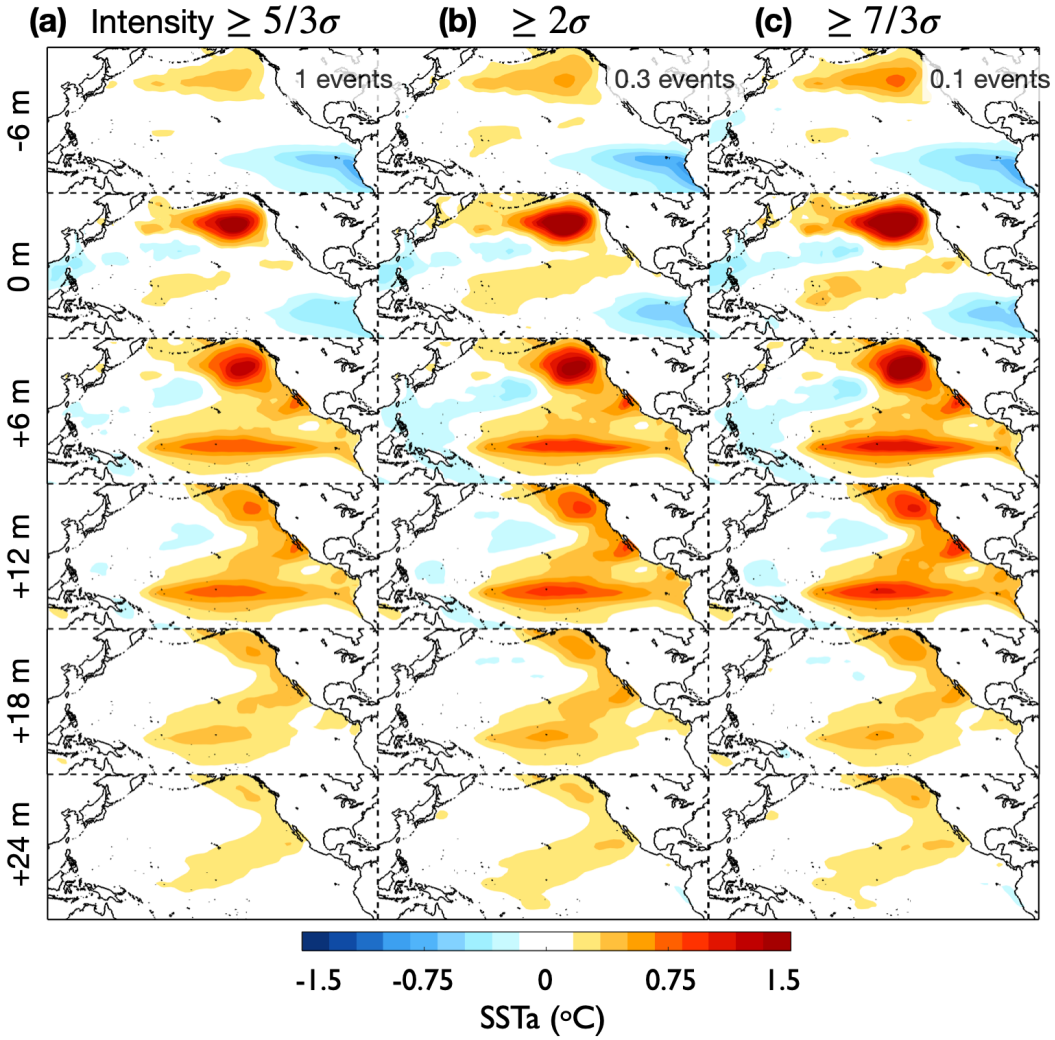

Figure 8. Same as Figure 6, except that the intensity threshold is varied while the duration threshold is fixed at 6 months.

2.5 Implication on the 2013-2015 Marine Heatwave Event

Finally, we evaluated how consistent the most extreme observed event, the 2013-2015 MHW event, is with the above LIM diagnosis, starting by analyzing the evolution and corresponding 6-month-lead LIM prediction of this historical multi-year event. The observed evolution (Figure 9a-e) shows a large warm anomaly developing and then intensifying within a broad region of the Gulf of Alaska, concurrent with a strengthening La Niña (Figure 9a-b). The warm SSTa subsequently spread eastward and then along the entire Pacific North American coastal boundary, along with a meridional mode structure and weak positive tropical SSTa (Figure 9c-d). The event ended with El Niño developing in the equatorial Pacific (Figure 9e). Note that this evolution featured both long-lasting, record-breaking warm anomalies in Northeast Pacific and the delayed development of strong El Niño conditions. Based on our findings in the previous section, the long-lasting feature of this MHW event may be strongly affected by the tropical variability, while the record-breaking intensity of this event may be influenced by the intrinsic variability of the extratropics.

The 6-month-lead LIM prediction patterns (Figure 9f-j) of the 2013-2015 MHW event, calculated from (2), track the observed evolution patterns (Figure 9a-e) with significant spatial correlation skill (R=0.60). Notably, the LIM prediction captured the North Pacific offshore warming in spring 2013 (Figure 9f) and the intensification of the anomalies in winter 2013/14 (Figure 9g). The NPMM-like warm anomalies with weak El Niño were also predicted (Figure 9h) in fall 2014 and winter 2014/15, and the emergence of El Niño in fall 2015 (Figure 9j). Overall, the LIM prediction of this historical MHW

event serves as another demonstration of the LIM's capability for capturing Pacific dynamics and seasonal MHW evolution.

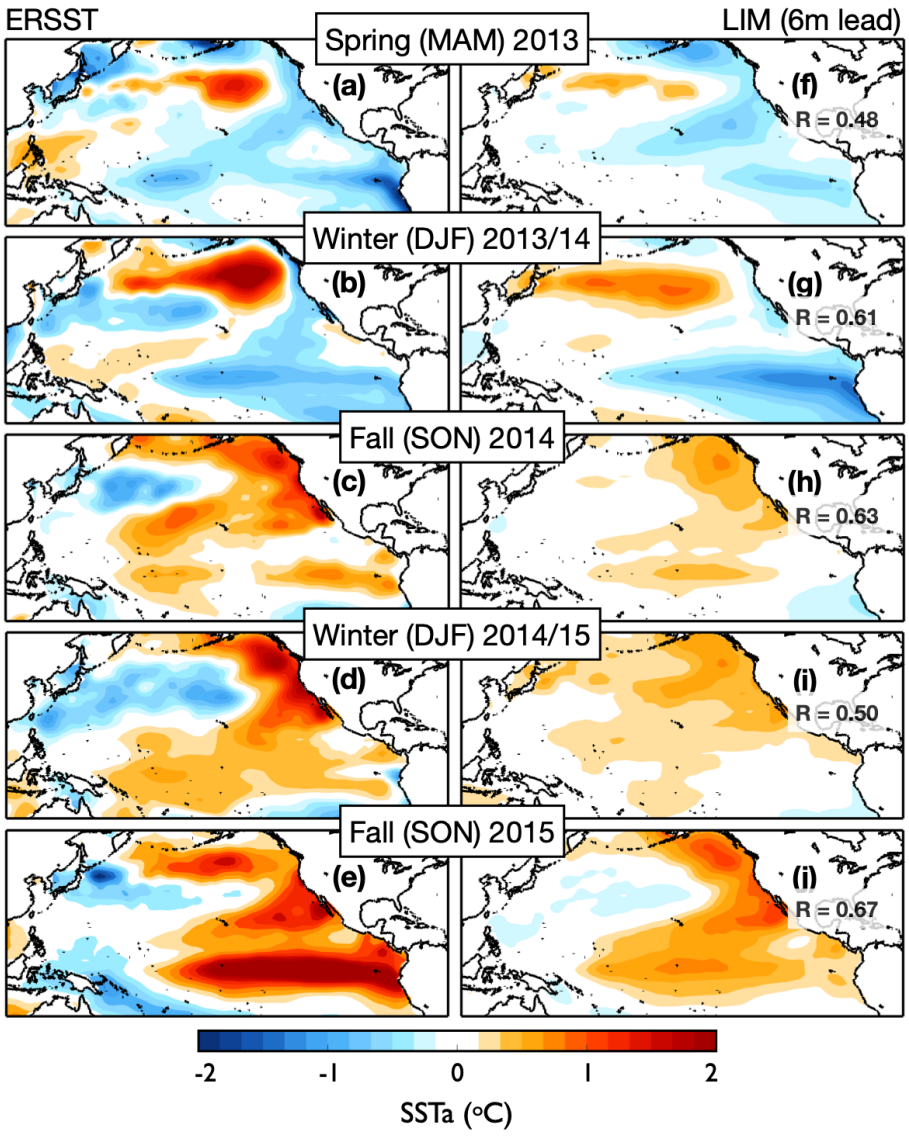

Figure 9. Evolution of seasonal SSTa, 2013-2015, from (a-e) observations, (f-j) 6-month lead cross-validated LIM predictions. (a, f) March-April-May (MAM) 2013. (b, g) December-January-February (DJF) 2014. (c, h) September-October-November (SON) 2014. (d, i) December-January-February (DJF) 2015. (e, j) September-October-November (SON) 2015.

Lastly, while we have shown that the statistical behavior of the MHW composite was captured by the millennia-long LIM simulation, perhaps the 2013-2015 MHW event was too extreme for our simple stochastically-forced linear model. Therefore, we explored whether a subset of MHWs in the LIM simulation could be found that represented even this single historical event. Using an analogue approach (e.g. Ding et al., 2018; Vandendool, 1994), we determined the 20 MHW events within the LIM simulation that had the highest spatial and temporal correlation to the 2013-2015 MHW event over its entire 32 month evolution.

In general, in an analogue approach we would search a data library for the k-member states $[\mathbf{x}(t_1') \quad \mathbf{x}(t_2') \quad \cdots \quad \mathbf{x}(t_k')]$ closest to a target state $\mathbf{x}(t)$, where k is the analogue index and t_k' is the time of the analogue in the library. However, we are interested not just in finding a good match for a single observed state, $\mathbf{x}(t)$, but in finding a match to a *sequence* of observed states during some prolonged period,

$$\mathbf{v}(t) = \begin{bmatrix} \mathbf{x}(t) \\ \mathbf{x}(t+1) \\ \vdots \\ \mathbf{x}(t+p) \end{bmatrix}, \tag{6}$$

where p is the prolonged period of the persistent anomalies denoted by $\mathbf{v}(t)$. In essence, we searched the k-member persistent anomalies $[\mathbf{v}(t_1') \quad \mathbf{v}(t_2') \quad \cdots \quad \mathbf{v}(t_k')]$ with the highest spatial and temporal correlation to the 2013-2015 MHW event over 32 months ($p = 32$, $k = 20$). The spatial and temporal correlation was defined as the correlation between the observed long vector $\mathbf{v}(t)$ and each simulated long vector $\mathbf{v}(t')$. The average of the 20 closest or "top-20" analogues, shown in Figure 10a-e, shows a similar evolution

pattern to the 2013-2015 event (R=0.71), although the intensities of the composite are not as extreme as the historical event, suggesting the importance of noise to the evolution of any individual event.

To evaluate whether our LIM ensemble was dependent upon possible climate change, we repeated the analysis by constructing a new LIM from data only over the interval 1950-1989, and then ran a separate ensemble LIM simulation. The "top-20" analogue composite from the new ensemble LIM simulation (Figure 10f-j) also captures the 2013-2015 event (R=0.7), but its amplitudes are a little weaker, which may only partly be explained by sampling. The overall similarity of both composites suggests that the 2013-2015 event evolved in a manner consistent with Pacific climate dynamics prior to the emergence of any visible climate change effects in the North Pacific. However, the pre-1990 LIM cannot entirely capture such a prolonged period of high amplitudes, suggesting some potential climate change component that remains to be quantified.

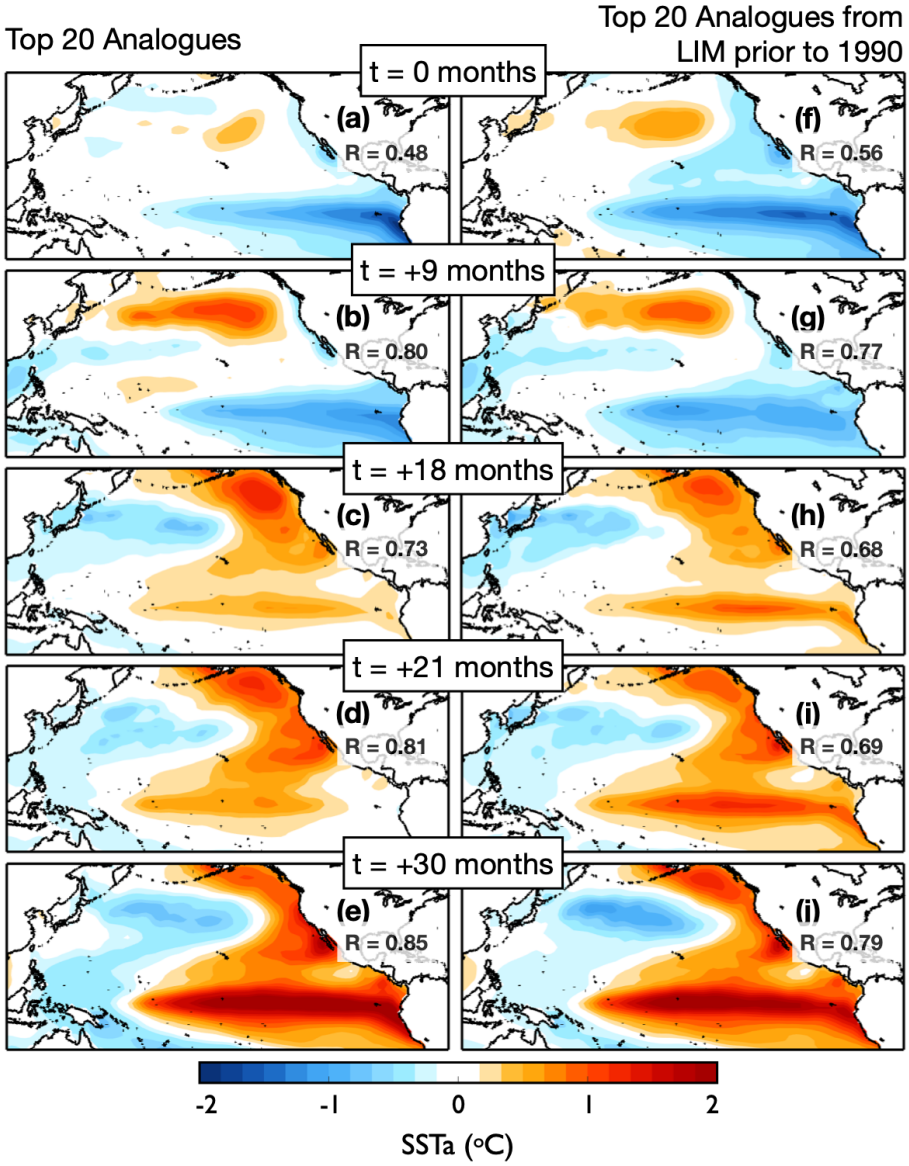

Figure 10. Composite evolution of top 20 model analogues of the 2013-2015 event within the LIM simulation.

2.6 Climate Change Impact on the Northeast Pacific Marine Heatwaves

In the previous section, the analogue composite constructed from the pre-1990 LIM ensemble has suggested some potential influence of climate change affecting the 2013-2015 MHW event. Here we investigate the climate change influence on the statistics of Northeast Pacific MHWs by (1) adding the linear trend that was previously removed (see data processing in section 2.2) back to the observation and to each of the 2000-member 70 years LIM ensemble, (2) then separating the 70-years observation and LIM ensemble into two 35-year periods. Any statistical behavior difference between the two periods, one corresponding to 1950-1984 and other corresponding to 1985-2020, is then considered a result of the climate change. [Note that all previous analysis in this chapter does not contain the linear trend.]

We first generated the IDF map for the two periods (Figure 11). Compared with the observed IDF of 1950-1984 (shading of Figure 11a), the observed IDF of 1985-2020 (shading of Figure 11b) showed overall higher frequency of extreme MHWs. Specifically, higher intensity MHWs have happened more frequently, while the frequency of longer-duration MHWs has increased only slightly (shading of Figure 11c). Statistics of the LIM ensemble (contour lines of Figure 11) is overall consistent with the observation (shading). The characteristic of high-intensity MHWs happening more frequently and longer-duration MHWs occurring slightly more frequently is reproduced by the LIM ensemble, indicating that our large ensemble LIM simulation captures the influence of climate change on the statistical behavior of MHWs. The IDF analysis also corroborates with the result from the previous section, suggesting that the extreme intensity of the 2013-2015 event may be partly contributed by the influence of climate change.

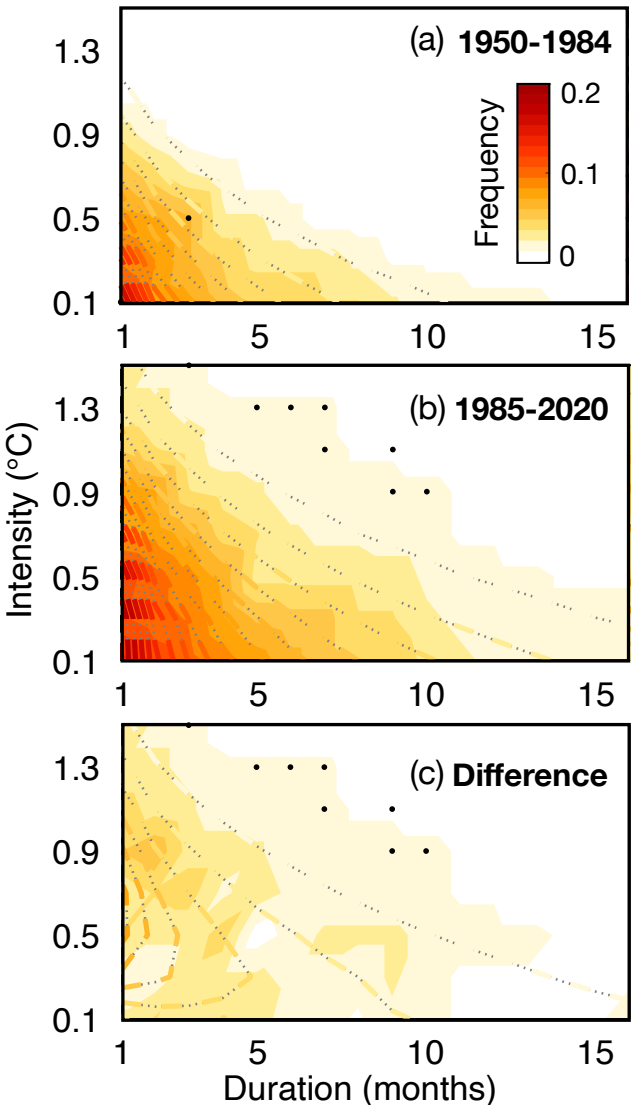

Figure 11. IDF map for (a) 1950-1984, (b) 1985-2020, (c) the difference between the (b) and (a), with the observed linear trend. Shading is the observation. Color-dashed line is the LIM ensemble average. Black dots represent the observed frequencies under those intensity-duration pairs are 95% statistically different from LIM.

Having LIM ensemble consistent with observation, we now analyze, within the LIM ensemble capacity, how the concurrent evolution of the tropical Pacific and the Northeast Pacific MHWs varies under the influence of climate change. To do so, we calculated and showed the Niño 3.4 index as a function of the Northeast Pacific index during the two periods (Figure 12). With the intensity threshold fixed as 1σ, each line represents a different duration threshold (from light orange to copper corresponds to 5 to 14 months duration threshold used in the 1950-1984 ensemble; from light green to blue corresponds to 5 to 20 months duration threshold used in the 1985-2020 ensemble; Figure 12a) used to identify the concurrent evolution of Niño 3.4 index and the Northeast Pacific index. In Figure 12b, color of the line represents a different intensity threshold, while the duration threshold is fixed as 6 months.

Compared with the concurrent evolution of Niño 3.4 index and Northeast Pacific index within the 1950-1984 ensemble (light orange to copper in Figure 12a and b), the evolution within the 1985-2020 ensemble (light green to blue in Figure 12a and b) is overall shifted to a higher intensity. While having overall higher intensity for both the Northeast Pacific index and the Niño 3.4 index, the range of the variation becomes less. To be more exact, the magnitude increase from prior to the initiation of MHW to the peak is less within the 1985-2020 ensemble. The magnitude increase of the Niño 3.4 index is also smaller. Overall, this suggest that under the influence of climate change, the mean background states may become warmer but the variance may be decreasing. Thus, the intensity of the MHWs under the influence of climate change may be more extreme, whereas the variance of the MHW evolution may be decreasing.

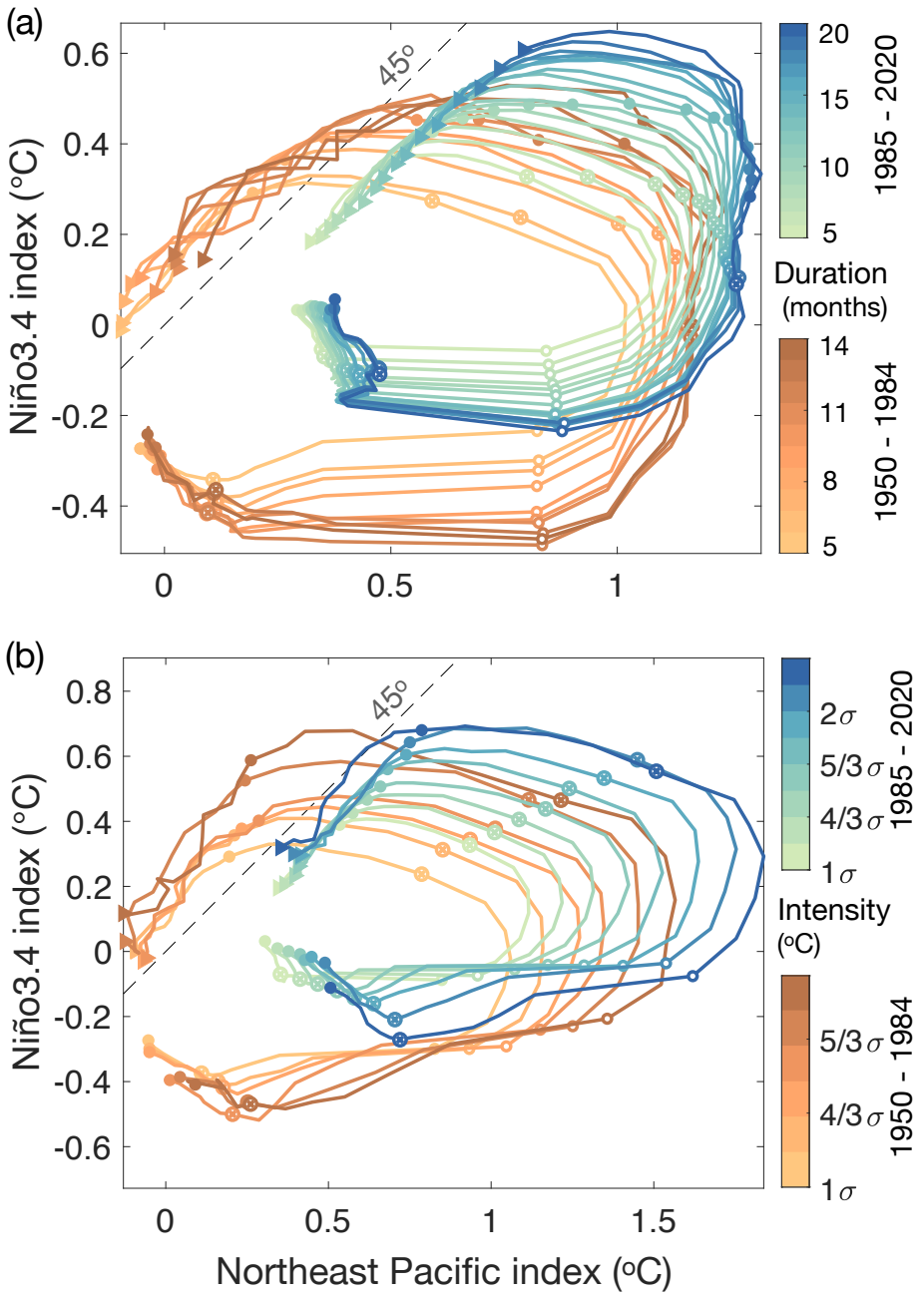

Figure 12. Niño 3.4 index as a function of the Northeast Pacific index for 1950-1984 and 1985-2020. (a) Intensity of MHWs is fixed at 1σ, while the duration increases from 5 months. (b) Duration of MHWs is fixed at 6 months, while the intensity increases from 1σ.

2.7 Conclusion

Our study explored Northeast Pacific warming events over a continuum of intensities and durations, including the evolution of conditions as extreme as occurred during the 2013-2015 MHW, suggesting that these events are a recurrent phenomenon of North Pacific dynamics. Using the ensemble LIM simulation, we reproduced the statistics of observed MHWs, notably the relative frequencies of events with different durations and intensities and their corresponding composite evolution. The LIM large ensemble was then used to diagnose relative tropical and extratropical influences on MHW intensity and duration. We find that greater MHW duration is linked to stronger La Niña during the early stages of MHW evolution and to a subsequently extended development of El Niño, suggesting that the tropics play an important role in MHW duration. In contrast, MHW intensity depends primarily on North Pacific initial conditions, suggesting that MHW intensity may be largely driven by variability intrinsic to the extratropics. Both contributed to the multi-year persistence and record-breaking intensity of the 2013-2015 MHW event.

Our analysis in terms of the potential role of climate change suggests that the mean changes in SST due to recent climate trends in the North Pacific are not a necessary requirement to explain the evolution of an event like the 2013-2015 MHW. The analysis of the ensemble LIM analogues trained with data between 1950-1989 captures MHWs that are dynamically consistent with the 2013-2015 event. Nevertheless, climate change is a contributing factor, particularly for the *prolonged severity* of the 2013-2015 MHW. Some recent studies (Laufkötter et al., 2020; Oliver, 2019) suggest that the main impact of climate change upon MHWs is through changing the mean rather than the variability, which is consistent with our approach.

Lastly, although the 2013-2015 Northeast Pacific MHW event motivated this study, the Northeast Pacific is not the only region where MHWs occur. They have been observed around the globe with various spatial and temporal scales (e.g. Benthuysen et al., 2018; Mills et al., 2013; Oliver et al., 2017), associated with different drivers. While our study focuses on Northeast Pacific MHWs and presents the LIM's ability to capture the statistics and evolution of even the more extreme Northeast Pacific MHWs like the 2013-2015 event, it also points to a promising avenue for a global assessment and understanding of MHWs.

CHAPTER 3. THE ROLE OF TROPICAL PACIFIC AND NORTH PACIFIC ON FORECASTING SEA SURFACE TEMPERATURE AND HEIGHT ALONG THE NORTH PACIFIC COASTLINE

In 0 we explored the statistical behaviors of Northeast Pacific marine heatwaves and had suggested that these marine heatwaves might have a predictable component, due to their connection to the remote tropical Pacific. Those analysis, however, focused only on the small sample size of abnormally warm time periods (i.e., the tail of probability density function) rather than the entire observed time period. Here we aimed to evaluate the forecast skill of the entire time period from LIM framework constructed by tropical Pacific and North Pacific sea surface temperature (SST) and sea surface height (SSH) anomalies. Our analysis specifically targeted four coastal regions, California Current System (CCS), Gulf of Alaska (GoA), East China Sea (ECS) and Kuroshio Extension (KE), for these are representative coastal ecosystem of the North Pacific. Our result suggested that CCS and GoA, located along the North Pacific eastern boundary, had some additional dynamical skill that were captured by the LIM, whereas the LIM was less skillful for forecasting the ECS and KE along the North Pacific western boundary. Within the framework, removing the tropical Pacific versus North Pacific anomalies, one at a time, allowed us to diagnose the role of tropical Pacific versus North pacific on the forecast of the North Pacific coastal areas. Our result indicated that the remote tropical Pacific had strong influence (at least comparable to local North Pacific influence) on the forecast skill of the two lower latitude coastal regions, CCS and ECS, whereas the influence of tropical Pacific was limited on the two further northern coastal regions, GoA and KE.

3.1 Introduction

Coastal water, generally referred to regions within 100 km offshore with less than 100 m water depth, occupies only about 7.5% of the ocean water. Yet it had been documented to have contributed to nearly 50% of the global marine fish productivity (Nellemann et al., 2008). Ecological conditions relevant to the primary productivity were found sensitive to SST and mixed layer variability (Miller and Schneider, 2000). Thus, providing a skillful forecast of these ocean conditions on a time scale relevant to ecosystem's response, i.e., at least on a seasonal scale (Jacox et al., 2020b), is a critical task.

Among all the coastal waters of North Pacific, CCS, GOA, ECS and KE are the representative regions of focus in this study (Figure 15a). CCS, GOA and ECS were defined similar to Large Marine Ecosystem (LME) (Hervieux et al., 2019; Sherman, 1986; Stock et al., 2015), as "coherent ocean areas generally along continental margins whose ecological systems are characterized by similarities in bathymetry, hydrography, and biological productivity". KE was not conventional in the definition of LME, as it was characterized by the convergent flow from the subtropical Kuroshio current of low productivity and the subarctic Oyashio current of high productivity (Qiu, 2019), which extends offshore to west of dateline. This unique characteristic leads to a defined KE covering from coastline to west of dateline, as in many previous studies (Joh and Di Lorenzo, 2019; Qiu et al., 2014 and references therein).

Seasonal prediction of the North Pacific coastal SST has been conducted through ensemble global-scale dynamical and statistical modeling systems. The state-of-the-art

North American multimodel ensemble (NMME) of coupled global climate models had shown a forecast correlation skill of ~0.5 within GoA and CCS at a 6-month lead (Hervieux et al., 2019). A recent study using a near-global LIM (Shin and Newman, 2021) had shown forecast skill within GoA and CCS comparable to NMME. 6-month-lead correlation skill of KE using the coupled global Fast Ocean Atmosphere Model (FOAM) was ~0.3 (Wu et al., 2016), which was consistent with the findings of LIMs (Alexander et al., 2008; Dias et al., 2019). Forecast of ECS (Peng et al., 2021) was conducted by the model-analog approach, which searched ocean states similar to present in the "data library" of Coupled Model Intercomparison Project phase 6 (CMIP6) and treated the subsequent evolution of those states as the forecast. This study showed that the 6-month-lead forecast skill of ECS was ~0.2-0.3.

Forecast skill of coastal SSH was less documented. It is of interest, as SSH is generally considered an indicator of the stratification and mixed layer depth and, thus, can be viewed as a proxy of the upper ocean heat content. NMME showed 6-month-lead SSH correlation skill of ~0.6-0.7 at GoA and CCS and ~0.1 at ECS and KE (Shin and Newman, 2021). The same study also compared the NMME forecast skill to the near-global LIM, and showed that LIM had comparable-to-NMME skill at GoA and CCS and higher-than-NMME skill at ECS and KE.

To understand the forecast skill contributed by local North Pacific versus remote tropical Pacific forcing, studies have developed, for instance, sensitivity tests of a dynamical model that run hindcasts driven by either local or remote forcing, i.e., one of them being full variability forcing and the other being only the climatology (Frischknecht et al., 2015). The statistical approaches were to construct the model framework of both the

tropical Pacific and the North Pacific state vectors and, by setting one of the state vectors to zero, the influence of remote tropical Pacific versus local North Pacific forcing was quantified (Dias et al., 2019).

Although the prediction skill of coastal waters is an active research area, it remains unclear the contribution of tropical Pacific versus North Pacific to the SST and SSH prediction skill of the representative North Pacific coastal waters. Thus, in this study, we (a) constructed a LIM framework of the tropical Pacific and the North Pacific SST and SSH for lead-1- to lead-12-month forecast, (b) evaluated the prediction skill of the targeted coastal waters against persistence, i.e., local memory, and (c) analyzed the influence of tropical Pacific SST and SSH versus the influence of North Pacific SST and SSH on the prediction skills.

3.2 Data and Methods

3.2.1 Data

We obtained 1958-2017 monthly SSTs from the Hadley Centre Sea Ice and Sea Surface Temperature data set (HadISST) (Rayner et al., 2003) and monthly SSHs from the European Centre for Medium-Range Weather Forecasts (ECMWF) Ocean Reanalysis System 4 (ORAS4) (Balmaseda et al., 2013). The spatial resolution was $1^{o}\times1^{o}$. The spatial domain ranged from 20^{o}S to 60^{o}N and from 110^{o}E to 60^{o}W, excluding any areas of Gulf of Mexico and the Atlantic Ocean. The SST anomaly (SSTa) and SSH anomaly (SSHa) were calculated by removing the climatological annual cycle and linear detrending.

3.2.2 Linear Inverse Model

LIM and its ensemble mean forecast was extensively introduced in 2.2.2. Here we constructed a LIM framework of North Pacific (20°N to 60°N) and tropical Pacific (20°S to 20°N) SSTa and SSHa, as followed,

$$\begin{bmatrix} \hat{\mathbf{x}}_{TP}(t+\tau) \\ \hat{\mathbf{x}}_{NP}(t+\tau) \\ \hat{\mathbf{y}}_{TP}(t+\tau) \\ \hat{\mathbf{y}}_{NP}(t+\tau) \end{bmatrix} = \mathbf{G}(\tau) \begin{bmatrix} \mathbf{x}_{TP}(t) \\ \mathbf{x}_{NP}(t) \\ \mathbf{y}_{TP}(t) \\ \mathbf{y}_{NP}(t) \end{bmatrix}, \mathbf{G}(\tau) \equiv \exp(\mathbf{L}\tau) \quad (7)$$

where **x** was leading Principal Components (PCs) of SSTa, **y** was leading principal components of SSHa, the subscript TP referred to tropical Pacific and NP was North Pacific. We first separately calculated the Empirical Orthogonal Function (EOF) space of tropical Pacific SSTa, North Pacific SSTa, tropical Pacific SSHa and North Pacific SSHa and respectively retained 8, 18, 8, 12 leading PCs, which explained 82.32%, 82.51%, 74.77% and 57.88% of each corresponding total variance. The combination of PCs was determined by EOF truncation test, i.e., testing the forecast skill sensitivity to the number of PCs retained in the system.

Estimation of **L** and forecast skill was "ten-fold" cross-validated: (a) excludes 10% of the data at a time, (b) re-estimates **L** using the remaining years and (c) computes the forecast initialized from that 10% previous excluded data. This procedure was repeated 10 times and the forecast output was concatenated in the end.

Finally, the impact of tropical Pacific forcing versus the North Pacific forcing was evaluated by setting either $\mathbf{x}_{NP}(t) = \mathbf{y}_{NP}(t) = 0$ or $\mathbf{x}_{TP}(t) = \mathbf{y}_{TP}(t) = 0$. In the former scenario, forecast was entirely contributed by the initial tropical Pacific forcing. Whereas in the latter scenario it was solely contributed by the initial North Pacific forcing. Note that

it was allowed to maintain only one of the four state vectors as non-zeros, which allowed us to examine the role of the standalone state vector (Figure 18, Figure 19).

3.3 Prediction Skill Compared to Persistence

We first computed the persistence skill of SSTa at 3-, 6-, 9-, and 12-months lead (Figure 13a), i.e., the correlation between one SSTa time series and the lag-τ-months SSTa time series. This is considered a forecast based on only the local memory. Persistence showed forecast skill gradually decreasing over lead time, indicating that the "present" local memory played less of a role on the forecast skill over time. Areas with remaining forecast skill at 9- and 12-month lead covered from south California to the equatorial Pacific around dateline, resembling the pattern of PMM. Forecast skill was also seen with a pattern that extends from Peru to the equatorial Pacific around dateline, resembling the pattern of SPMM. These patterns were consistent with studies that suggest PMM and South PMM as important precursor dynamics (Chiang and Vimont, 2004; Zhang et al., 2014).

Compared with persistence, LIM showed additional forecast skill within tropical Pacific (Figure 13b, c), which suggests that the precursor dynamics were captured by our LIM framework and, thus, transformed into forecast skill of the tropical Pacific. LIM also showed, to some degree, improved forecast skill along the North Pacific eastern boundary. This might be a result of incorporating the remote tropical forcing in the modeling system, as ENSO had been diagnosed as a source of predictability along the eastern boundary (Jacox et al., 2019a).

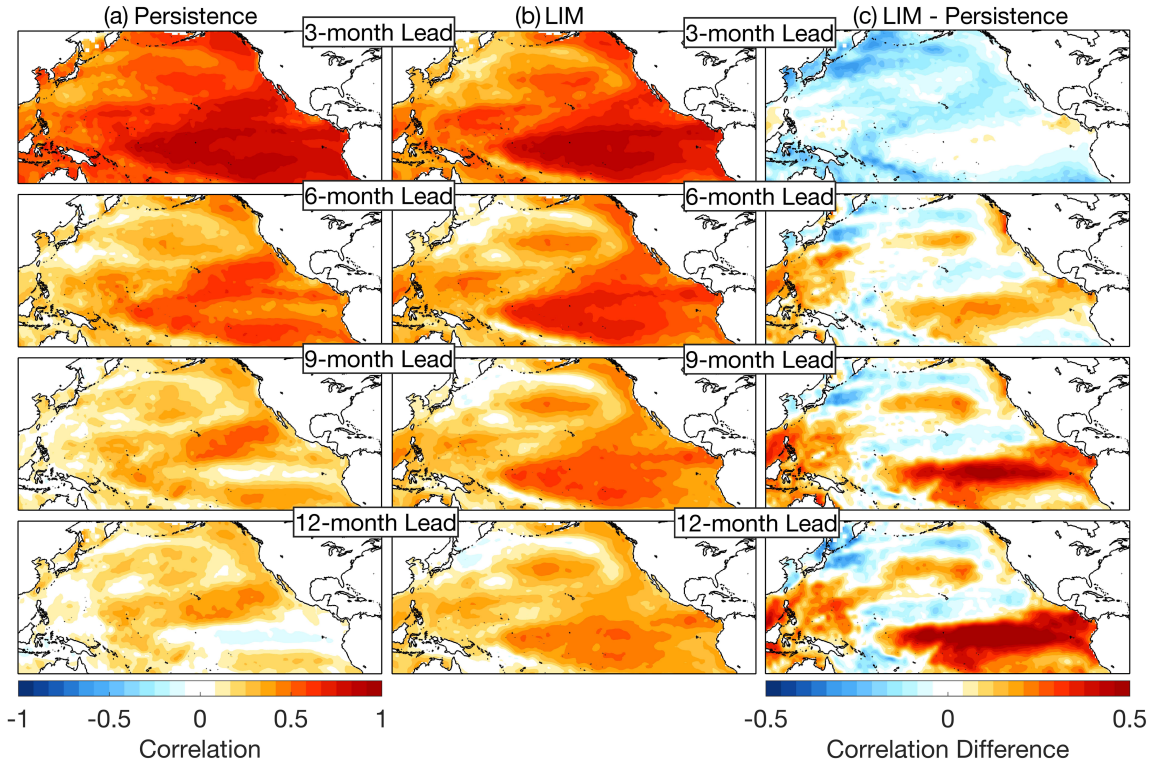

Figure 13. SSTa forecast skill of (a) persistence, (b) LIM, and (c) difference between LIM and persistence for 3-, 6-, 9-, 12-months lead.

We then examined the forecast skill of SSHa (Figure 14). Besides having gradually decreasing skill over lead months, persistence (Figure 14a) showed correlation skill remaining to be quite high above the latitude of KE. This suggest that SSHa of the higher latitude North Pacific might carry long term ocean memory, which might be the dominant source of SSHa predictability within the area.

Compared with persistence, LIM showed additional forecast skill within the tropical Pacific and along the North Pacific eastern boundary (Figure 14b, c), potentially a result of ENSO and the propagation of coastally-trapped Kelvin waves. North of Japan, LIM's forecast skill was slightly worse than the high persistence skill, which also emphasized the dominant role of local memory within those areas.

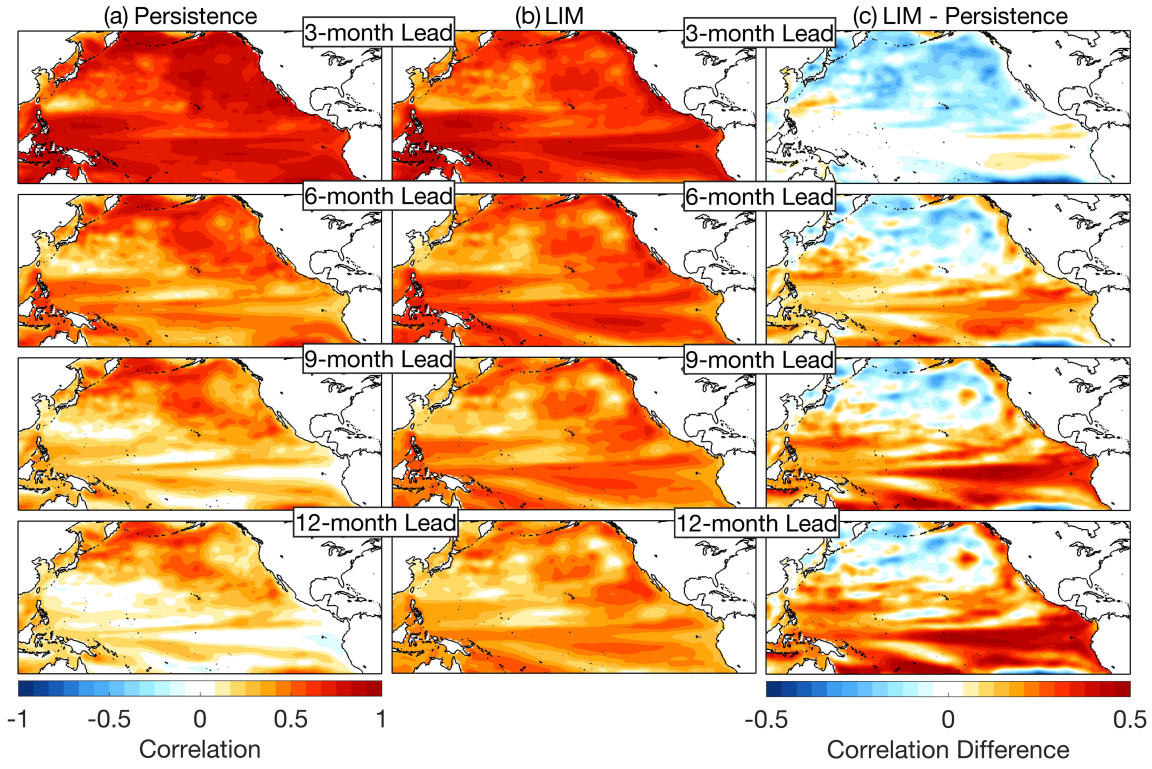

Figure 14. SSHa forecast skill of (a) persistence, (b) LIM, and (c) difference between LIM and persistence for 3-, 6-, 9-, 12-months lead.

Then LIM and the persistence skill were spatially averaged within each targeted coastal regions (Figure 15). CCS was defined within 132°W-110°W, 28°N-50°N; GoA was defined within 158°W-130°W, 50°N-59°N; ECS was defined within 116°E-130°E, 22°N-40°N; KE was defined within 138°E-164°E, 30°N-42°N (Figure 15a). In GoA, LIM's SSTa and SSHa forecast skill (thick solid line and thick dash line of Figure 15b) were lower than persistence (thin solid line and thin dash line) for <6 lead months. For lead months ≥ 6, LIM's forecast skills were higher than persistence, suggesting our LIM might have captured the remote forcing dynamics that contributed to the forecast skill. In CCS (Figure 15c), LIM's forecast skills were higher than persistence for lead months ≥ 4. This suggest that CCS might be strongly influenced by remote forcing and that influence reached to the low latitude CCS earlier than the high latitude GoA.

In ECS (Figure 15d), the LIM and persistence skill were comparable from lead-1 to lead-12 months, and both skills decreased rapidly over lead months. This suggest that neither was ECS subject to local memory nor did our LIM framework capture any useful information that contributed to the forecast skill of ECS. It might also indicate that ECS was shielded from the remote forcing. In KE (Figure 15e), LIM's skill was either comparable to or lower than the persistence skill, potentially due to the convergent flow containing large variability of mesoscale eddies and, thus, was considered as noise within the LIM framework.

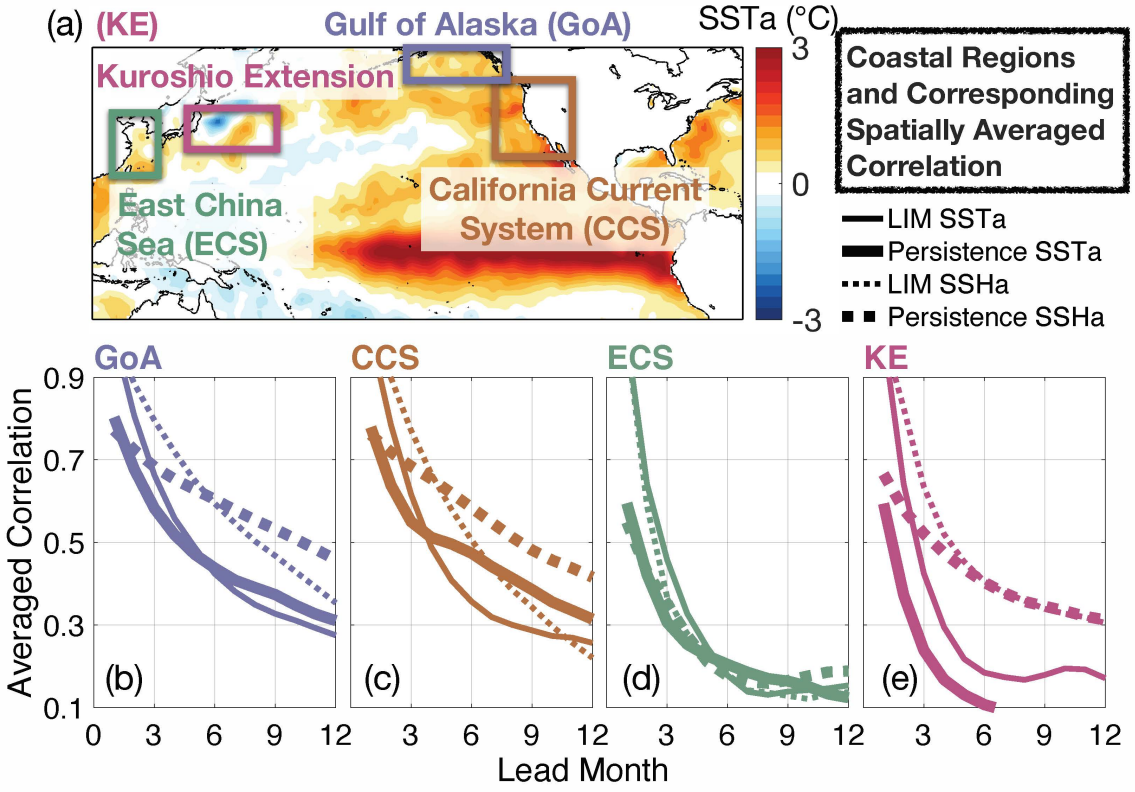

Figure 15. Coastal regions of interest (a) and their corresponding spatially averaged forecast skill (b-e).

3.4 Influence of Tropical Pacific versus North Pacific

To better understand the forecast skill of the representative coastal regions, we first evaluated the SSTa forecast skill contributed by North Pacific forcing versus tropical Pacific forcing (Figure 16). Under the contribution of tropical Pacific only, at 3-month lead (first row of Figure 16a), tropical Pacific influence was largely contained within the tropical Pacific, as the correlation skill within tropical Pacific was much higher than the skill outside tropical Pacific. At 6-month lead (second row of Figure 16a), forecast skill within North Pacific, especially along the coastal waters, increased as the influence from remote tropical forcing became stronger. At 9- and 12-month lead (third and fourth row of Figure 16a), the forecast skill gradually decreased within both the tropical Pacific and the North Pacific.

Under the contribution of solely the initial North Pacific forcing (Figure 16b), it was seen that forecast skill along the North Pacific eastern boundary was initially high at 3-month lead, and gradually decreased over lead months. Starting from 6-month lead, the forecast skill along the North Pacific eastern boundary was comparable between the skill contributed by the tropical Pacific and the skill contributed by the North Pacific. This indicated that the tropical Pacific was the source to the additional forecast skill captured by LIM.

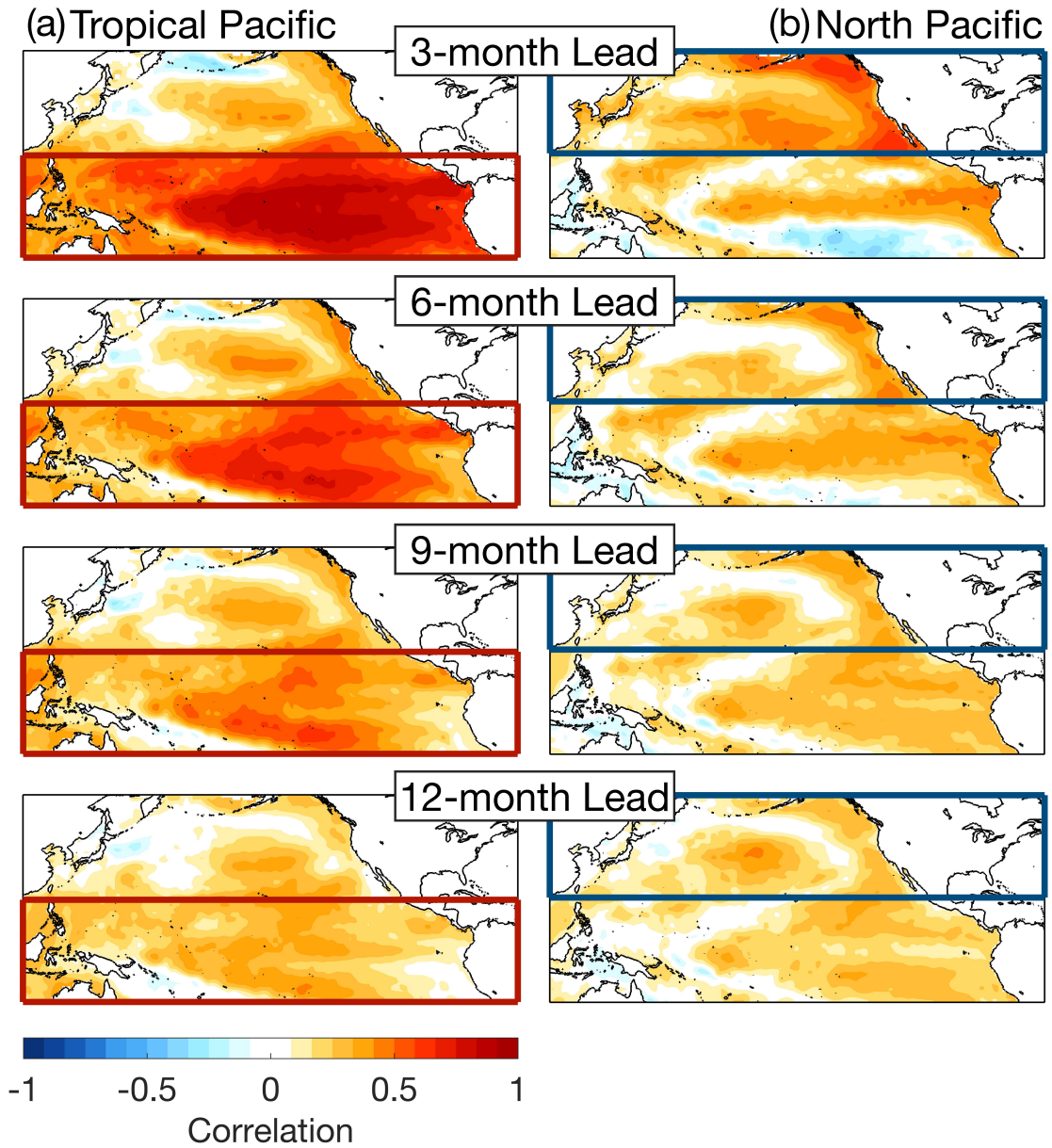

Figure 16. SSTa LIM forecast skill contributed by (a) tropical Pacific, or (b) North Pacific at 3-, 6-, 9-, 12-lead months.

In terms of tropical Pacific influence on the SSHa forecast skill (Figure 17a), we saw high forecast skill within tropical Pacific at 3-month lead, which gradually decreased over lead months. Tropical Pacific forcing also contributed to high forecast skill along the eastern boundary of North Pacific, which was an indication of the coastal Kelvin waves carrying tropical Pacific information northwards, steered by the continental boundary.

North Pacific forcing, on the other hand, was very persistent within North Pacific (Figure 17b). The persistent high correlation pattern was similar to the simple persistence model (Figure 14a), which suggest that SSH of the large area of North Pacific, except along the eastern boundary, was dominated by local memory.

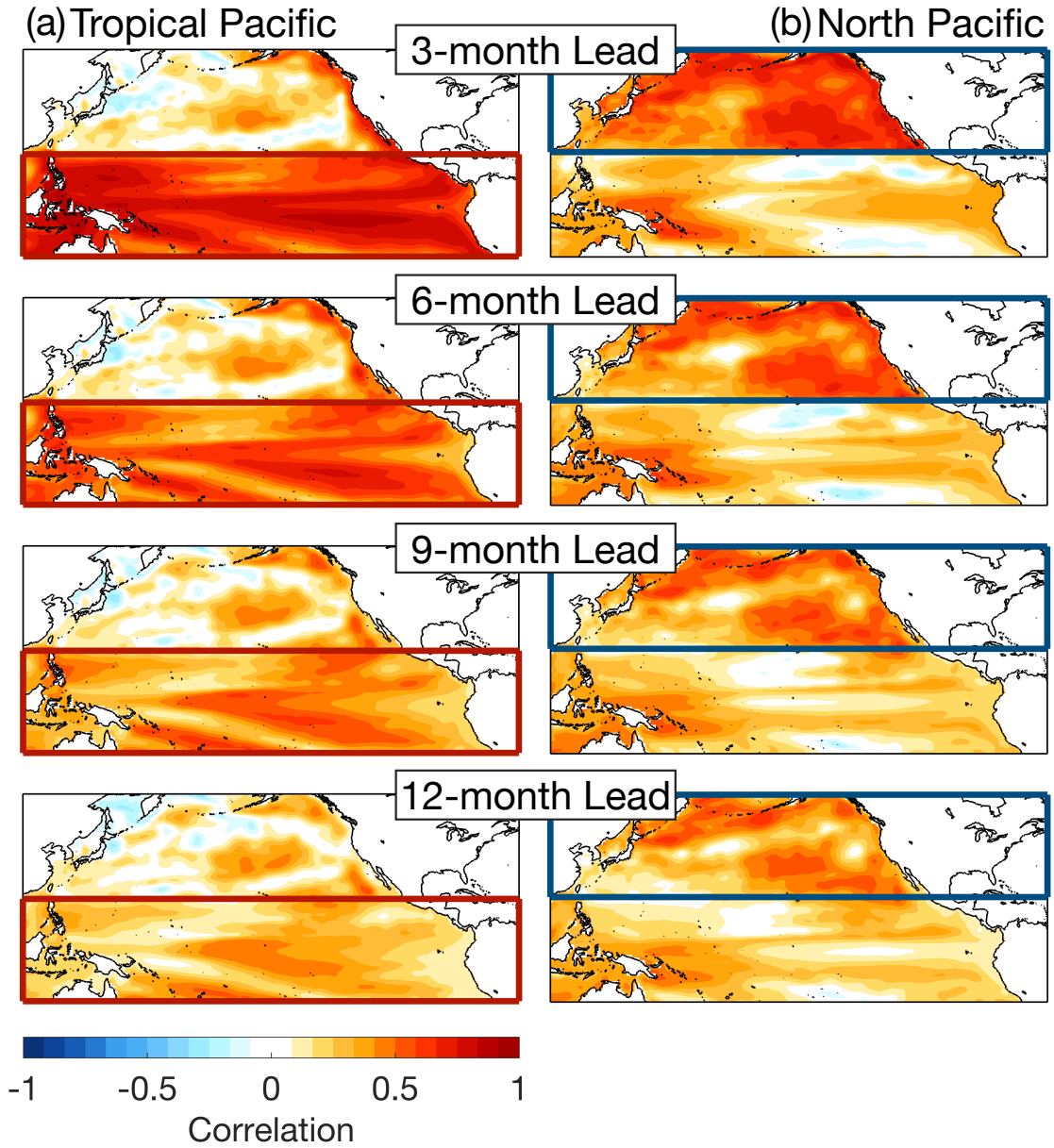

Figure 17. SSHa LIM forecast skill contributed by (a) tropical Pacific, or (b) North Pacific at 3-, 6-, 9-, 12-lead months.

We further split the forecast skill contributed by tropical Pacific into forecast contributed by tropical Pacific SSTa versus contributed by tropical Pacific SSHa (Figure 18a, b). Interestingly, while in Figure 16 we showed tropical Pacific contributed to the additional dynamical forecast skill along the North Pacific easter boundary, here the result showed, at California and south of California, the additional skill was contributed by tropical Pacific SSTa (Figure 18a), whereas at north of California, the additional skill was from tropical Pacific SSHa (Figure 18b).

Similarly, influence of North Pacific was split into influence of North Pacific SSTa versus North Pacific SSHa (Figure 18c, d). Our result showed North Pacific SSTa had only limited influence (Figure 18c), consistent with findings that suggest midlatitude extratropical SSTa was largely driven by weather noise and, thus, intrinsically not predictable (Frankignoul and Hasselmann, 1977; Hasselmann, 1976). North Pacific SSHa (Figure 18d), on the other hand, was able to contribute to the SSTa forecast skill along the North Pacific eastern boundary. This might be related to SSH being a proxy of the thermocline depth and upper ocean heat content and, therefore, SSH-contributed to SST forecast might be considered a result of the influence of below surface ocean memory.

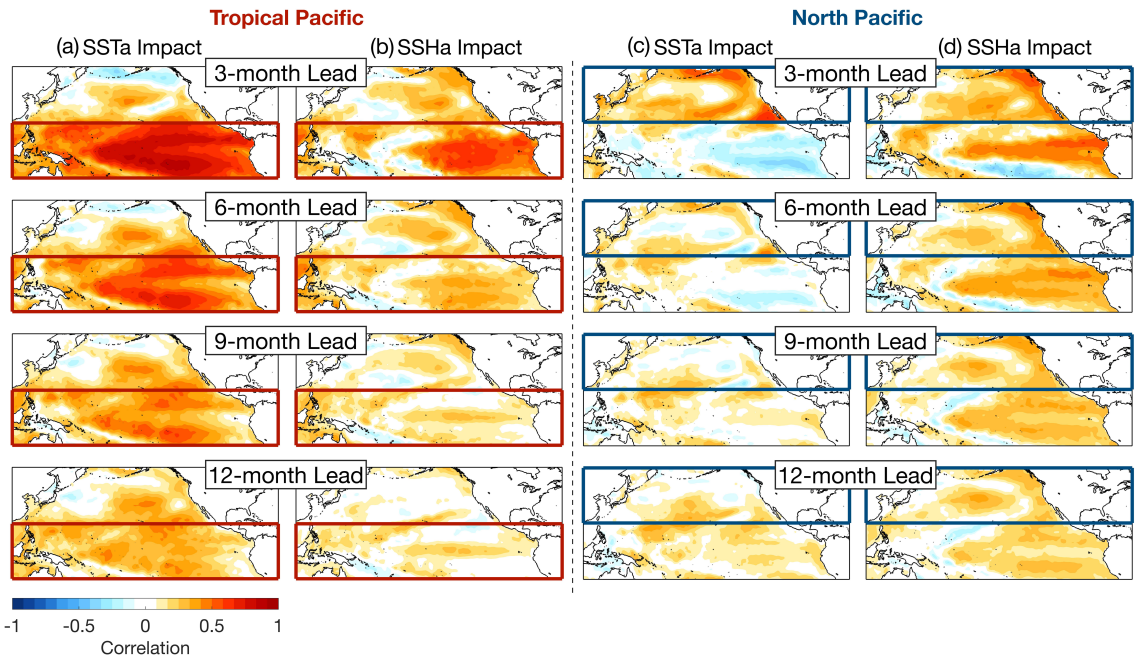

Figure 18. LIM forecast skill of SSTa at 3-, 6-, 9-, 12-month lead, by retaining only one non-zero state vector: (a) tropical Pacific SSTa; (b) tropical Pacific SSHa; (c) North Pacific SSTa; and (d) North Pacific SSHa.

In terms of tropical Pacific SSTa versus SSHa influence on SSHa forecast (Figure 19a, b), it is seen that tropical Pacific SSTa contributed to the additional forecast skill of SSHa along the North Pacific eastern boundary, more than the contribution from tropical Pacific SSHa.

As for North Pacific SSTa versus SSHa influence on SSHa forecast (Figure 19c, d), North Pacific SSTa had overall very limited influence, which corroborated with the unpredictable nature of the midlatitude SSTa (Frankignoul and Hasselmann, 1977; Hasselmann, 1976). North Pacific SSHa generated very persistent forecast skill, which indicated a dominant role of North Pacific subsurface ocean heat content on the persistent forecast skill.

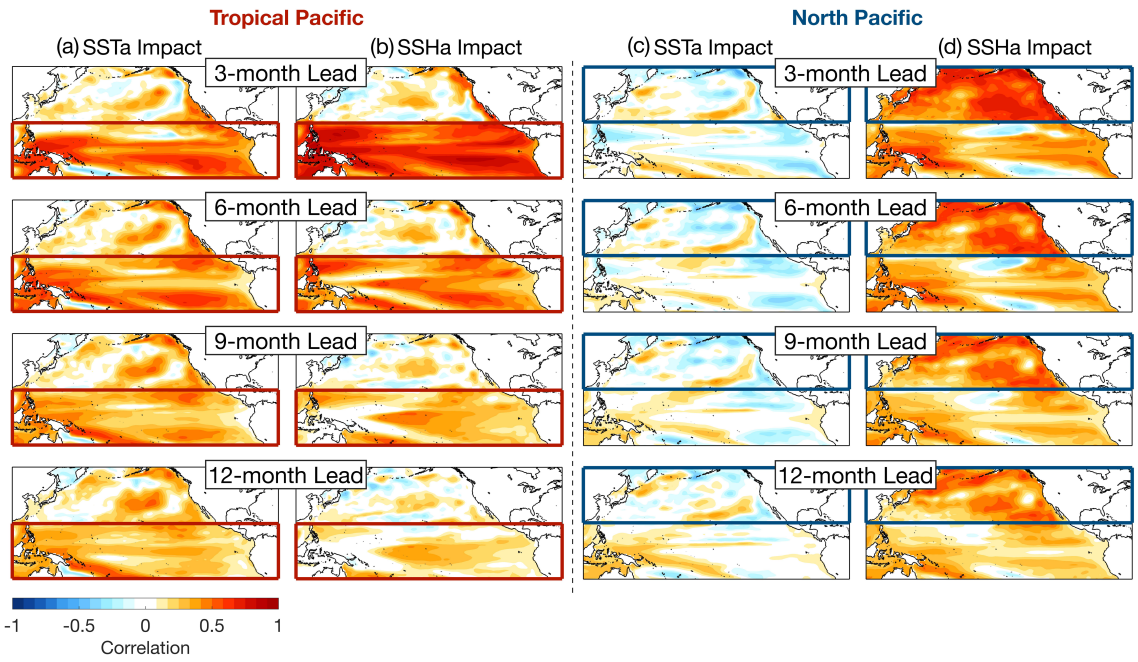

Figure 19. LIM forecast skill of SSHa at 3-, 6-, 9-, 12-month lead, by retaining only one non-zero state vector: (a) tropical Pacific SSTa; (b) tropical Pacific SSHa; (c) North Pacific SSTa; and (d) North Pacific SSHa.

Lastly, the correlation skills contributed by initial tropical Pacific forcing versus by initial North Pacific forcing were spatially averaged within each targeted coastal regions (Figure 20), with the full LIM forecast skill superimposed (i.e., full LIM curves identical to Figure 15). In GoA, under the influence of North Pacific forcing, the SSTa and SSHa correlation skill was initial high and comparable to the skill of full LIM at lead-1 month (blue curves compared to purple curves in Figure 20a). Then the correlation skill contributed by North Pacific forcing gradually decreased as the lead months increased. On the other hand, under the influence of tropical Pacific forcing, the correlation skill gradually increased from lead-1 month to lead-6 month and then decreased afterwards (red curves), suggesting the first increasing, then decreasing influence on GoA forecast from the remote tropical Pacific. The tropical Pacific contributed forecast skill was lower than the North Pacific contributed forecast skill (red curves compared to blue curves), indicating that the forecast skill of GoA was dominated by the local North Pacific forcing.

In CCS, the result was similar (Figure 20b). The difference was that tropical Pacific influence reached to a peak at lead-4 months, compared to the lead-6 months in GoA. This was a result of CCS located at a lower latitude than GoA. Another difference was that tropical Pacific influence became comparable to or slightly higher than the North Pacific influence at lead-6 months, which corroborates with the findings of Jacox et al. (2019a) that linked the CCS forecast skill to the ENSO variability.

In ECS and KE, we have shown in previous analysis that the LIM forecast skill was at most comparable to persistence (Figure 15d, e). Thus, it was expected that the North Pacific forcing, in essence equivalent to local memory, dominated the LIM forecast skill. This was the case for KE (see that the blue curves almost overlapped with the pink curves,

and that the red curves were almost constant at 0). In ECS, however, tropical Pacific influence on SSTa became stronger than the North Pacific influence, starting from lead-5 months, (despite that both tropical Pacific and north Pacific influence were very weak), suggesting some level of dominant control from tropical Pacific.

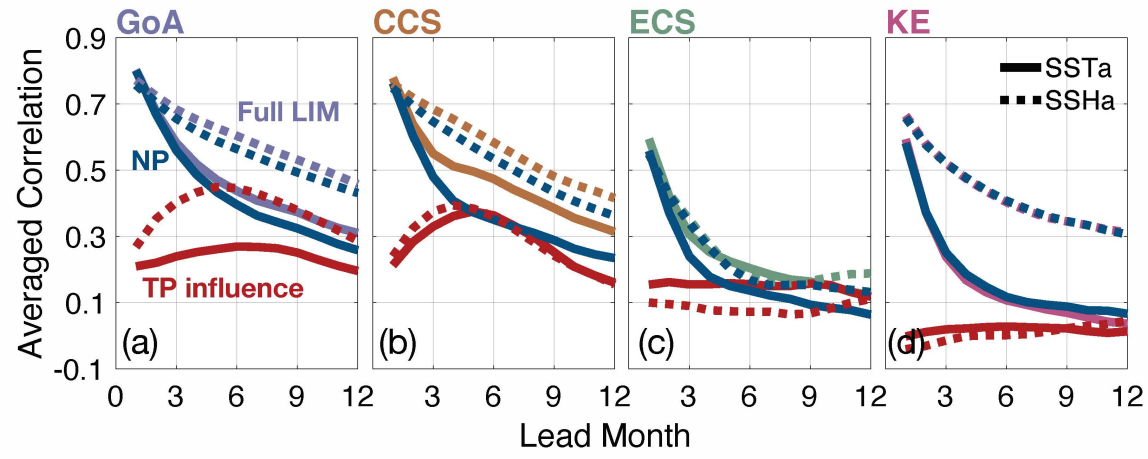

Figure 20. Spatially averaged SSTa (solid lines) and SSHa (dash lines) forecast skill of the full LIM (color identical to the region name), tropical Pacific LIM (red) and North Pacific LIM (blue).

3.5 Conclusion

In this study we have constructed a LIM framework of North Pacific and tropical Pacific SST and SSH to analyze the forecast skill of SST and SSH at coastal waters of North Pacific and to understand the role of tropical Pacific versus North Pacific on the forecast. Our result suggested that the constructed LIM captured large-scale dynamics and, hence, provided additional forecast skill than the ocean memory persistence along the eastern boundary of North Pacific, whereas the forecast skill along the western boundary was largely contributed by the local memory.

By only retaining the tropical Pacific anomalies versus the North Pacific in the LIM system, we examined the forecast skill solely contributed by tropical Pacific forcing versus by North Pacific forcing. Our result showed that the improved forecast skill of SST and SSH along the eastern boundary of North Pacific was contributed by tropical Pacific forcing, which corroborates with former studies that linked the forecast skill of CCS to the ENSO variability (Frischknecht et al., 2015; Jacox et al., 2019a). Furthermore, retaining only one of the four state vectors (e.g., tropical Pacific SST only) in the LIM system allowed us to differentiate the influence from SST versus from SSH. We showed that North Pacific SST provided very limited forecast skill, consistent with the unpredictable nature of the midlatitude extratropics. Whereas North Pacific SSH was very persistent and, hence, provided long term memory and forecast skill along the eastern boundary.

This study has not considered the seasonal variation of the forecast skill (e.g., forecast initialized from January versus from July) and how the tropical versus North Pacific forcing acts onto the seasonal variation. To accurately represent the seasonal

variation, one may further assess the significance of the seasonal variation and compare the LIM constructed by the full records with the LIM that includes annual cycle, i.e., cyclostationary LIM, similar to the approach taken by a recent study on impact of annual cycle on ENSO variability in tropical Pacific (Shin et al., 2021). Whether our short historical record was enough to build a cyclostationary LIM of North Pacific and tropical Pacific and whether that was necessary remains to be explored. Overall, our current LIM framework provides a robust assessment based on the entire record and serves as a baseline for a future cyclostationary LIM study.

CHAPTER 4. THE NEAR-REAL TIME PREDICTION AND PREDICTABILITY DYNAMICS OF INNER-SHELF CIRCULATION AROUND PT. SAL, CALIFORNIA

While the low-dimensional empirical LIM captures the large-scale ocean dynamics in the North Pacific (Newman et al., 2016) and their coastal footprint on scales of ~100 km, ocean processes near the coast at scales ~10 km to 100 m are not well-resolved in climate prediction models and data. To improve predictability along the coastline, where coastal processes dominate the variability, ocean models with fine resolution becomes necessary to resolve multi-scale coastal processes and their interactions with shallow bathymetry and complicated coastline (Jacox et al., 2019a).

An experimental forecasting system for the inner shelf circulations around Pt. Sal, California, was implemented using a multi-scale nesting configuration of the Regional Ocean Modeling System (ROMS), integrated in the Coupled-Ocean-Atmosphere-Wave-Sediment-Transport (COAWST) modeling system. The system was operational from September 1 to November 30, 2017 to assist the observational campaigns and in situ data collection of the Office of Naval Research (ONR) Inner Shelf Dynamics DRI field experiment (Kumar et al., 2020). Forecast of ocean conditions were conducted daily through the downscaling of several nested COAWST simulation grids (3km → 1km → 600m → 200m), each forced with the COAMPS 2-days atmospheric forecasts at hourly resolution. By comparing the field observations to the model forecasts, we present an assessment of the skill of the COAWST forecasts focusing on the 200-meter scale.

To further diagnose the dynamics underlying the model forecast skill, we generated a set of ensemble simulations of the COAWST Pt. Sal modeling framework with different configurations of boundary and surface forcing conditions. Using this ensemble, we analyze and quantify the sources of predictability (e.g. deterministic vs. internal variability) that originate from knowledge of the open ocean boundary conditions, surface forcings, and initial conditions. We find that the initial conditions carry little skill beyond 2 days and that the largest fraction of dynamical skill is associated with knowledge of the surface and boundary conditions. This suggest that direct data assimilation to initialize the ocean model state may not be required for an operational ocean forecast in the inner shelf.

4.1 Introduction

Point Sal, a 5-kilometers coastal headland, is located in the Santa Maria Basin along the central California coast (Figure 21). Due to the fact that the shoreline orientation and the local bathymetry rapidly varies in the alongshore direction adjacent to Point Sal, the dynamic interaction between winds, sub-mesoscale eddies, surface and internal waves, mixing and surfzone processes can lead to complex three-dimensional local circulation near Point Sal (Kumar et al., 2019). Thus, although the circulation near Point Sal is primarily wind-driven (Strub et al., 1987), the combined effect from the ubiquitous coastline irregularity makes it the key interest of a multi-institutional effort supported by the Office of Naval Research Inner Shelf Departmental Research Initiative (Inner-shelf DRI).

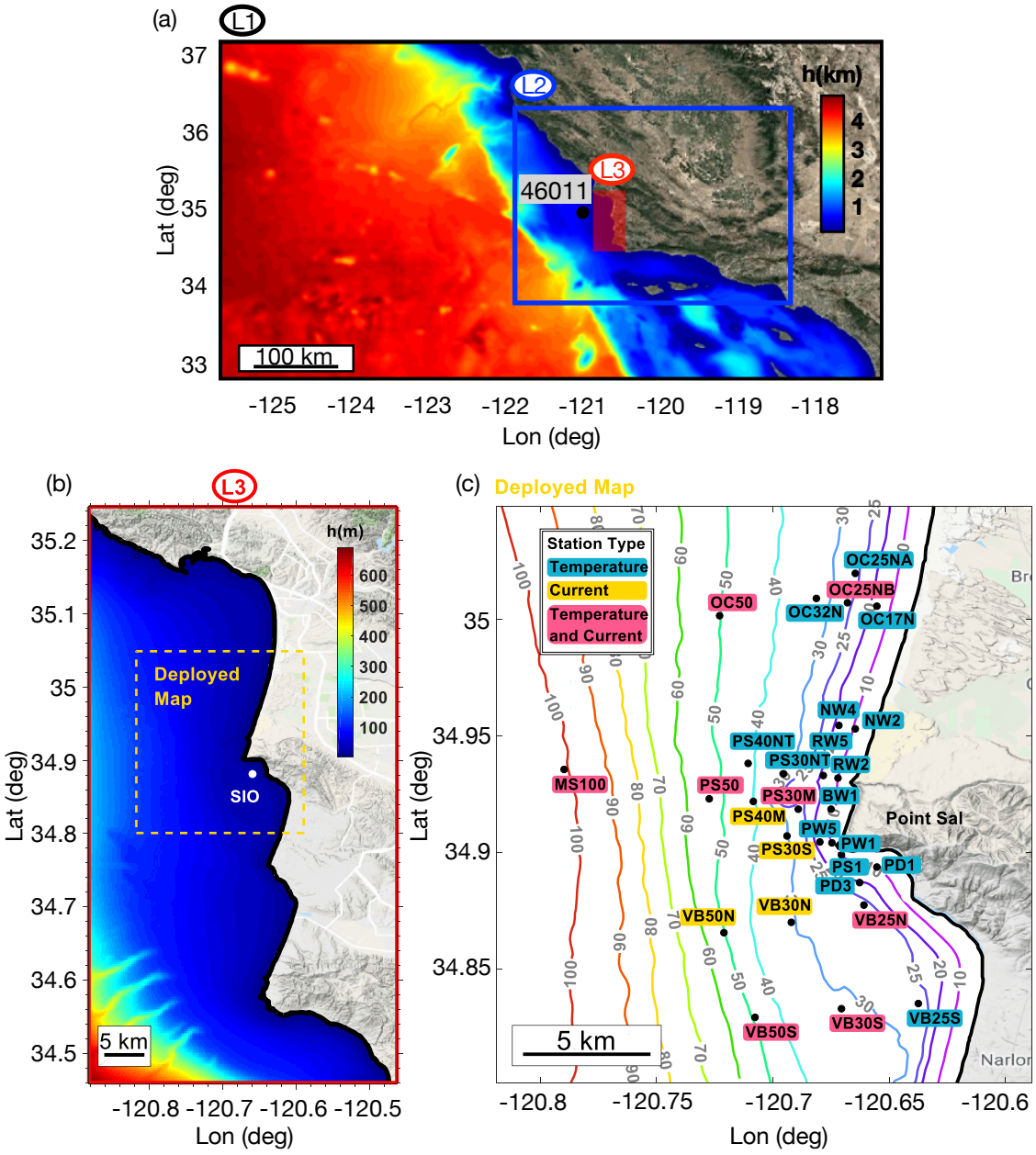

Figure 21. Down-scaling nested grids and locations of in-situ measurement. (a) Modeling scheme downscales from 1km (L1), 600m (L2) to 200m (L3). The black dot marks the location of the wind station 46011. (b) Enlarged map for the 200m grid. White dot marks the location of the wind station SIO. Yellow dash box marks the range of deployed in-situ measurement. (c) The location of Point Sal and the deployed instruments relevant to this study during 2017 field measurement campaign.

To better understand and predict the exchange of water properties across the inner shelf over a range of temporal and spatial scales, the Inner-shelf DRI has launched an ongoing study on the ocean circulation in the vicinity of Point Sal using both the measurement approach and modeling approach. A study focused on the effect of wind relaxation on the generation of coastal buoyant plume (Suanda et al., 2016) shows that while an equatorward wind combined with Coriolis leads to cold water upwelling from the bottom to the nearshore surface, wind relaxation, on the other hand, is a favorable condition for a poleward propagation of warm water from the southern California. This poleward propagating warm plume can reach to Point Sal, although the width and the temperature of the plume decrease slightly. There are also studies on barotropic and baroclinic tides (Suanda et al., 2017), the generation and propagation of internal tide near Point Sal (Kumar et al., 2019).

In Fall 2017, the Inner-shelf DRI organized a comprehensive field measurement experiments, including airborne thermal and radar remote sensing, drifting measurement platforms and in-situ moorings. The portion of the relevant measurements to this study is mapped in Figure 21c. To assist the in-situ measurement and to better understand the dynamics, an ocean forecast experiment system has been developed in this study to automatically predict the ocean state evolution for the future 48 hours on a daily basis.

With the explosive growth of population and urban concentration near coastal regions, the necessity of closely monitoring and predicting the ocean state brings attention to scientists and researchers in oceanography and coastal engineering. But it was not until the late 1990s that the concept and the feasibility of developing a worldwide ocean observational program emerged and was broadly discussed (Harrison and Smith, 2002;

Traon et al., 1999). Since then, forecasting future ocean conditions has undergone a rapid development and becomes operational in many oceanographic institutions, including the National Oceanic and Atmospheric Administration (NOAA) in USA, the Commonwealth Scientific and Industrial Research Organization (CSIRO) in Australia with the BLUElink project (Brassington et al., 2007), the wide MERSEA Integrated Project in Europe: in France with MERCATOR (Bahurel, 2006; Drevillon et al., 2008); in the UK with FOAM (Bell et al., 2000); in Italy with the MFS –Mediterranean Ocean Forecasting System (Pinardi et al., 2003); and in Norway with TOPAZ (Brusdal et al., 2003).

With these worldwide and nationwide ocean operational forecast systems made available, along with the advances in more accurately measuring coastline and nearshore bathymetry, there are also many developing and developed regional ocean forecast system focusing on targeted coastal area. Marta-Almeida et al. (2011) developed a Python engine, named the Operational Ocean Forecast Engine (OOFϵ), for automating regional and coastal ocean forecasts on a daily basis. This Python engine is developed to automatically execute the generation of forcing, simulation of ocean circulation using ROMS and analysis of simulation results in a sequence. Marta-Almeida et al. (2010) then utilized this python engine as a tool in developing a regional operational ocean forecast system in Brazil. This forecast system went through a long-period of model spin-up to adjust the model for operationality, but the resolution of the forecast is only ~9km in the alongshore direction and 2km near the coast to 12 km offshore in the cross-shore direction. Zhang et al. (2012) used the OOFϵ engine to provide nowcast and a five-day forecast, which covers the entire Texas-Lousiana continental shelf and slope in a higher resolution: ~500m near the coast and ~1-2km on the outer slope area. The lateral climatological forcing is obtained from the

Hybrid Coordinate Ocean Model (HYCOM) nowcast/forecast system (Smedstad et al., 2010), a more up-to-dated hybrid ispycnal-sigma-pressure coordinate ocean model.

A regional ocean forecast system consists of an ocean model to carry on the simulation of ocean circulation, realistic initial forcings and lateral boundary forcings to serve as model inputs. Error is inevitable if the model formulation is an imperfect approximation of the physical processes of the nature or if the uncertainty in forcings causes the error to propagate from the forcings and evolve and grow in the system. To what extent a model can represent the nature is not necessarily quantifying the predictability of nature. Instead, it is estimating the predictability limits for the numerical model to simulate and predict nature (Branstator and Teng, 2010). Without losing generality, to the extent that a model is a good surrogate for nature, the sensitivity and uncertainty of forcings becomes crucial for a credible prediction and a useful assessment. There are three types of forcings in a regional model: (1) initial forcings, (2) lateral boundary forcings and (3) surface atmospheric/external forcings. The first one is an initial-value problem, referred to as the predictability of the first kind (Lorenz, 1963), which is essentially the prediction of evolution given some knowledge of its initial state. The second and the third are boundary-value problems, referred to as the predictability of the second kind (Lorenz, 1975), which is monitoring how the dynamical system responds to the continuous changing forcings. Consider a state variable in a unit area model as $s(x, y, z, t)$, initial forcing represents $s(x, y, z, 0)$, surface external forcing represents $s(x, y, 0, t)$ and the lateral boundary forcing corresponds to $s(0, y, z, t)$, $s(1, y, z, t)$, $s(x, 0, z, t)$ and $s(x, 1, z, t)$, assuming x, y are within a normalized range from 0 to 1. Therefore, the latter two forcing types are

considered separately because the lateral boundary forcings exist when a regional model is applied.

Recently, the predictability dynamics of models has drawn increasing attention. Ezer and Mellor (1992) studied the impact of surface atmospheric forcing on the variability of ocean circulation in Gulf Stream by applying non-zero wind forcing but zero heat flux or vice versa. They also suggested that the effect on bottom layer variability is less related to the surface forcing but more directly caused by the fluctuations from the lateral boundaries. Wei et al. (2008) perturbed the initial conditions to form an ensemble global forecast system so that the forecast error explained by the perturbed initial conditions was studied. They focused on optimizing the choice of initial ensemble perturbations. But the effect from surface external forcing was not considered. In fact, initial-value predictability itself is a topic widely discussed (Sriver et al., 2015; Teng and Branstator, 2011; Wei et al., 2008). Teng and Branstator (2011) studied this initial-value problem to analyze the decadal predictability of sea surface and subsurface temperature (within 300m). Their study showed that integrated subsurface temperature is less chaos and, thus, has longer temporal predictability. On the other hand, Chen et al. (2015b) studied the effect of atmospheric forcing versus internal ocean advection on the warming along Northeast U.S. continental shelf in 2012 and found that temperature increase in that region is largely controlled by the net air-sea heat flux, because ocean advection was cooling the water column, counteracting the air-sea heat flux. Sieck and Jacob (2016) classified the circulation type of the lateral boundary forcing to study the internal variability related to the variability of the surface boundary forcing, specifically, the sea level pressure.

A regional model system is commonly expected to have all three types of forcings: initial, lateral boundary as well as surface external forcings. Therefore, when considering the influence of forcings, it is, at least, nontrivial to quantify the importance of each type of forcings and their time scale of domination in the model system. Ezer and Mellor (1992) suggested that without proper surface forcing, model showed less realistic Gulf Stream separation. Including the boundary inflow also played a role in improving the Gulf Stream variability. They concluded that the model domain should be extended to reduce the impact from the boundary forcing to the targeted interested area. Reichler and Roads (2003) showed that initial forcing alone was important up to 2-month lead time. Whether boundary forcing played a significant role compared with initial forcing depended on the strength of boundary forcing, i.e., whether strong El-Nino Southern Oscillation existed during prediction. Wu et al. (2005), on the other hand, suggested that the impact of initial forcing decreased with the increasing simulation time length, while the impact from the boundary forcing showed no significant trend and yet could reach to the interior model domain. Branstator and Teng (2010) indicated that the impact of the initial forcing would eventually be overcome by the boundary forcing. Beyond 10 years, the climate system became solely a boundary-value problem. Corti et al. (2015), however, showed that the predictability arose mainly from the external forcing for prediction time scale longer than 1 year. Depending on the region, the domination time scale of initialization varied. Among all these studies, boundary forcing is commonly interchangeable with external forcing, surface forcing, atmospheric forcing, especially for predictability study on a global model. In our study, we aim to cleanly separate the three types of forcing and individually quantify their contribution to the forecast error as time evolves, and to gain a better understanding of the

temporal control and spatial control from each forcing compared with the intrinsic model dynamics.

The study herein presents the development of a multigrid ocean forecast system that downscales to a resolution of 200m (3km → 1km → 600m → 200m; Figure 21) in its highest resolution grid. The 200m grid covers the vicinity of Point Sal. The forecast system was automated to predict 2-day ocean circulation on a daily basis. The validation of the forecast result was assessed by comparing the 200m forecast with the observation collected in the 2017 Inner-shelf DRI field campaign. Then the predictability dynamics of the ocean forecast was studied by ensemble perturbation of the initial forcing, boundary forcing and surface atmospheric forcing. The layout of the following sections is: (section 4.2) methodology including the development of the ocean forecast system and the experiment setup for predictability dynamics; (section 4.3) assessment of ocean forecast compared with observations; (section 4.4) predictability feasibility of the forecast system.

4.2 Methodology

4.2.1 Development of the Ocean Forecast System

The numerical model implemented in the ocean forecast system was the Regional Ocean Modeling System (ROMS). ROMS is a three-dimensional, free-surface, bathymetry following numerical model, which solves the finite-difference approximations of the Reynolds Averaged Navier Stokes equations with hydrostatic and Boussinesq approximations (Haidvogel et al., 2008; Shchepetkin and McWilliams, 2005).

The modeling system here was composed of four nested model domains with one-way nesting and off-line techniques (Mason et al., 2010). The details of the model set-up and the effectiveness of simulating ocean circulation were described and validated in Suanda et al. (2016). Model bathymetry was interpolated from 1-arc second bathymetry provided by the NOAA National Centers for Environmental Information, U.S. Coastal Relief Model (CRM; http://www.ngdc.noaa.gov/mgg/coastal/crm.html; retrieved on April, 2017). The grid resolution as aforementioned was from **L0**: Δx = 3km, **L1**: Δx = 1km, **L2**: Δx = 600m, **L3**: Δx = 200m. Because this is a collaboration project among multi-institutions supported by Inner-shelf DRI, the ocean forecast of **L0** and **L1** was implemented through the open-source Rutgers ROMS in University of Santa Cruz. The ocean forecast of **L2** and **L3** was implemented through the ROMS module from the open-source Coupled Ocean Atmospheric Wave and Sediment Transport (COAWST) modeling system (Warner et al., 2010) in Georgia Institute of Technology.

The surface atmospheric forcing was obtained from the Coupled Ocean-Atmosphere Mesoscale Prediction System (COAMPS) (Doyle et al., 2009; Hodur et al., 2002) Real-Time Forecasts for Central and Northern California in Support of the Central and Northern California Ocean Observing System (CeNCOOS), developed and maintained by Naval Research Laboratory. The COAMPS Real-Time Forecast provides a 48-hour forecast on atmospheric forcing on a daily basis (https://www.nrlmry.navy.mil/coamps-web/web/cencoos; retrieved during September and November 2017). The spatial resolution is 4km and temporal resolution is hourly in the COAMPS forecast. The obtained surface atmospheric forcing is then interpolated and applied in the ocean circulation forecast of each grid.

The initial and lateral boundary forcing was provided by the eddy-resolving, real-time global and basin-scale ocean hindcast, nowcast, and prediction systems using the HYbrid Coordinate Ocean Model (HYCOM; https://www.hycom.org/; retrieved from September to November 2017) (Chassignet et al., 2009; Chassignet et al., 2007). The HYCOM nowcast/forecast system runs in real time at the Naval Oceanographic Office. The global nowcast/forecast system has a horizontal resolution of 1/12^{o}.

The experimental forecast system was carried out on a daily basis (Figure 22a) starting from August 23, 2017 to November 15, 2017. For instance, on August 23, 2017, a forecast experiment was implemented to predict the ocean circulation from 00:00:00 PST, August 23, 2017 to 00:00:00 PST, August 25, 2017. Simulated ocean circulation of the middle (00:00:00 PST, August 24, 2017) was extracted as the new initial forcing for the next forecast experiment. Then on August 24, 2017, a following forecast experiment was carried out to predict ocean evolution for the following 48 hours starting from 00:00:00 PST, August 24, 2017. All in all, the forecast experiments were implemented in a way such that the initial forcing of a today's experiment was extracted from the middle of a yesterday's experiment.

In each forecast experiment (Figure 22b), the forecast started from the downloading and interpolation of initial and lateral forcing from HYCOM and atmospheric forcing from COAMPS. Forecast ocean circulation, forced with these forcing, was simulated using the Rutgers ROMS on **L0** grid. Then, the lateral boundary forcing of the **L1** grid was interpolated from the simulated ocean trajectories of the **L0** grid, whereas the initial forcing and the atmospheric forcing were interpolated from the forcing of **L0** grid. Once the simulation of **L1** grid was completed, results were transferred from University of Santa

Cruz to Georgia Institute of Technology to continue the simulation for the **L2** and **L3** grid, consecutively. Simulation results from the **L3** grid were processed and transferred to the experimental forecast website (http://www.oces.us/onr/), where the latest forecast, as well as the historical forecast, the forcing and simulation results were stored and available for downloading. Every day, the forecast was completed and made available on the website around 17:00:00 PST. Extensive work and close collaboration between Georgia Institute of Technology and University of Santa Cruz was devoted to this project for automating and delivering the comprehensive experimental forecast system.

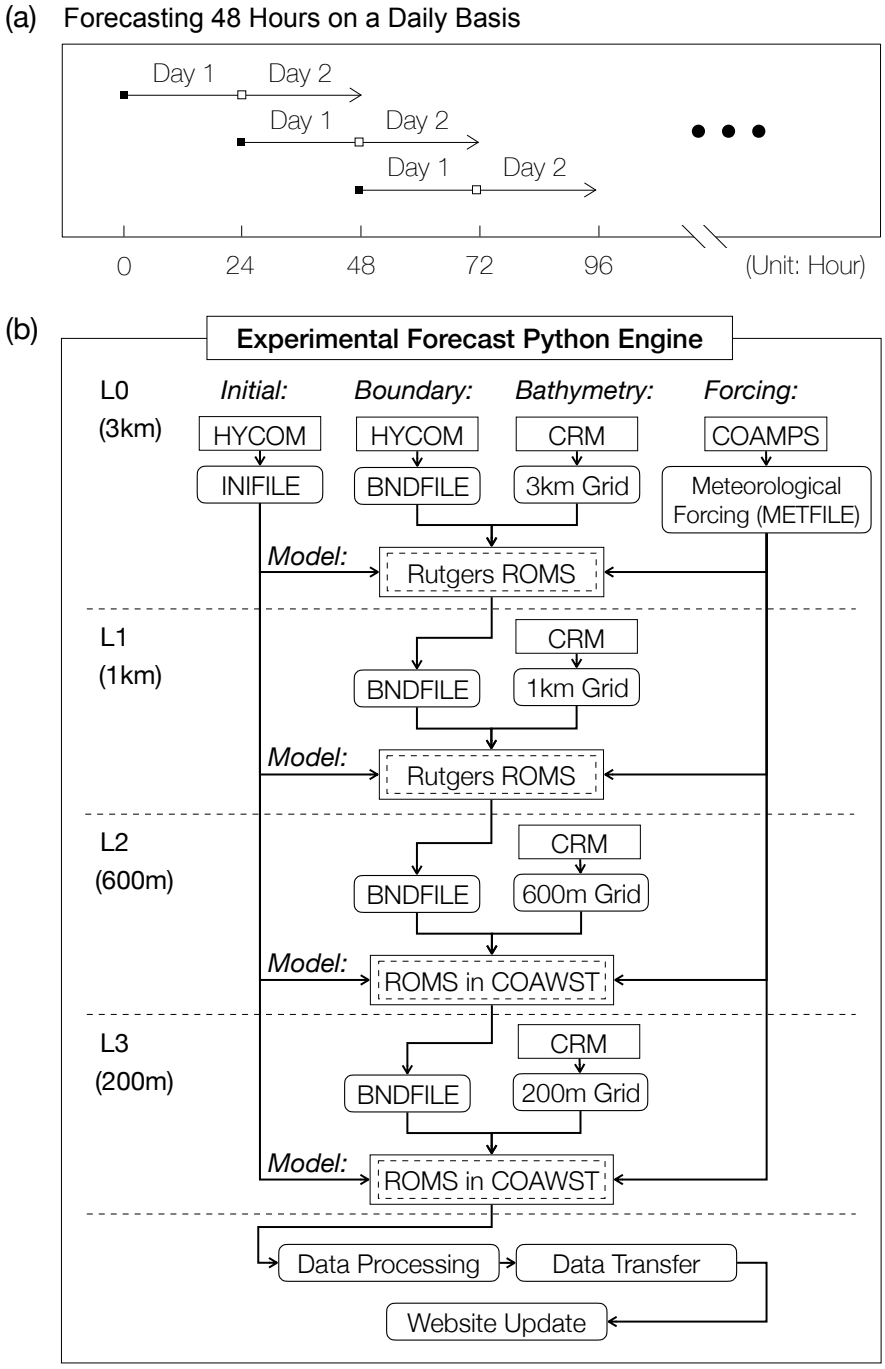

Figure 22. (a) Timeline of the daily 48-hour experimental forecast system. (b) Scheme of the experimental forecast system within each daily experiment.

4.2.2 Experimental Setup for Predictability Dynamics

Some recent studies have used ensemble-based approaches to quantitatively measure predictability with perturbed forcings assuming the model yields perfect projections without perturbation (Branstator and Teng, 2010; Corti et al., 2015; Reichler and Roads, 2003; Sieck and Jacob, 2016; Sriver et al., 2015; Teng and Branstator, 2011; Tommasi et al., 2017; Wu et al., 2005). To account for the uncertainty induced by initial forcings, initial forcings were commonly extracted from different time stamps of the control simulation and applied at the predetermined starting point, while other boundary conditions were held fixed, to analyze the evolution and the deviation limit from the perfect model. The atmospheric perturbation or the boundary perturbation were conducted by swapping forcings to different time periods taken from the control simulation (Corti et al., 2015) or by slightly offsetting the continuous changing physical parametrization in each ensemble experiment (Teng and Branstator, 2011).

Here we assume the forecast trajectories from the developed ocean forecast system as the perfect surrogate of nature and obtain the daily cycle of the input variables by averaging the field at each hour. These experiments were divided into three groups (Table 2): (1) initial forcings group (IC), in which identical initial forcings were applied at 00:00:00 of each day from August 1st, 2017 to November 8th, 2017, each ensemble simulation lasted for 10 days, and, in total, this formed 100 ensemble members; (2) boundary forcings group (BC), in which the boundary forcings of the daily cycle were implemented at the 100 predetermined starting times the same as IC; (3) surface atmospheric forcings group (SBC), in which surface forcings of the daily cycle were applied. Each member of ensemble experiment lasted for 10 days and all started from the

same 100 predetermined time points. In these three groups, other conditions were held fixed to minimize the effect of other uncertainties, such as different model structures, grid resolution, parameters, and forcings. Using these 300 ensemble experiments, we hope to answer the following questions: to what extent is predictability dominated by the initial forcings? If exists, when and how will the boundary forcings and the surface forcings gain over the domination against the initial forcing?

To answer these questions, it is important to choose the appropriate state variables. Branstator and Teng (2010) mentioned that one of the inadequacies of predictability investigations is the limitation in the selection of state variables. Sea surface temperature (SST) is usually used as the indicator, but the subsurface quantities are more predictable (e.g., Griffies and Bryan 1997a) because the weather noise can be shielded to some extend and the predictable fluctuations can be isolated. Thus, this predictability study focuses not only on SST but also on bottom temperature (BT), as well as surface currents (SU, SV) and bottom currents (BU, BV).

Table 2. Summary of ensemble experiments with one type of forcing varied while fixing the other two. Each ensemble experiment has 100 members of 10-days simulation.

Ensemble Experiments	Input Initial Forcing	Input Boundary Forcing	Input Surface Boundary Forcing
IC	Diurnal Signal	Control Simulation	Control Simulation
BC	Control Simulation	Diurnal Signal	Control Simulation
SBC	Control Simulation	Control Simulation	Diurnal Signal

4.2.3 Predictability Metrics

4.2.3.1 RMSD

Another aspect that is at least equally important as designing the ensemble experiments and targeting the proper variables is the metrics used to quantify predictability. The most commonly employed metric to quantify how much the ensemble differs from the control simulation is the root-mean-square difference (RMSD).

4.2.3.2 Correlation

However, using RMSD is not enough to measure the difference caused by perturbing forcings. Considered an extreme situation where two trajectories (e.g., $\mathrm{y(t)} = \sin(t)$ and $\hat{y}(\mathrm{t}) = \sin(t) + 1$) are identical with a constant unit bias, the RMSD between the two trajectories is 1, which is large given that the true trajectory $y(t)$ varies between -1 and 1. Thus, using RMSD as the only measure may send a misleading message that the two trajectories have significant difference with the order of magnitude similar to the trajectory variability.

To avoid such situations, it is helpful to include correlation as a supplementary metric. In the above situation, the correlation between the two trajectories is 1, indicating that the forecast trajectory is highly correlated with the true trajectory and thus, may still be considered as a good forecast capturing the dynamics of the nature.

4.2.3.3 Relative Entropy

While the RMSD measures the scale/magnitude of the difference between two trajectories and correlation measures the dynamical similarity, we need one more metric to summarize the mean signal difference and the spreading of error, i.e., the relative entropy (Kleeman, 2002) from information theory. In a dynamical system, suppose the prediction distribution is p, the climatological distribution is q, relative entropy (also called Kullback-Leibler divergence) (Kullback and Leibler, 1951) is defined to be

$$\mathrm{R(p,q)} = \int p \ln\left(\frac{p}{q}\right) dV \tag{8}$$

where V is the probability domain.

Relative entropy is a measure of how one probability distribution differs from a second, reference probability distribution. One merit of using this metric is that it combines the information from the relative dispersion and the mean into measuring how different the prediction distribution is from the climatology. Another attractive property is, for predictions of a Markov process, R always decreases monotonically with time. When R asymptotes to zero, it indicates that the impact or the additional information carried by the specification of forcing is lost (Kleeman, 2002).

With large enough sample size, the distributions p and q are approximately Gaussian. For the multivariate Gaussian distribution, R can be expressed as,

$$\mathrm{R} = \frac{1}{2}\left\{\ln\left(\frac{\det(\Sigma_q)}{\det(\Sigma_p)}\right) + tr\left[\Sigma_{\mathrm{p}}(\Sigma_q)^{-1}\right] + (\mu_p - \mu_q)^T(\Sigma_q)^{-1}(\mu_p - \mu_q) - n\right\} \tag{9}$$

in which n is the dimension of the state vector, μ is the n-dimensional mean vector, Σ is the n × n covariance matrix.

4.3 Assessment of the PILOT Forecast Experiments

The temperature anomaly from the 24 mooring locations at -5 m depth (Figure 23) showed that the model temperature compared well to the observed temperature with an overall bias of ~1°C. The correlation was between 0.7 and 0.9. In general, model temperature captured the pattern and large temporal scale variability of the observed temperature. Along the 10m depth contour (NW2-RW2-BW1-PW1-PS1-PD1; see Figure 21 compared with Figure 23), observed temperature has stronger high frequency variabilities (diurnal, semi diurnal and other high frequency variabilities) except PD1, which was located on the south of Pt. Sal. Because it was located inside the bay-like region, the temperature fluctuation was more relaxed (less high frequency) compared with others. Across the transect north of Pt. Sal (OC50-OC32N-OC17N), across the transect near Pt. Sal (MS100-PS50-PS30M-BW1) and across the south transect (VB50S-VB30S-VB25S), the high frequency variability of observed temperature increased from offshore to onshore. While the low frequency variability and the pattern of the observed temperature were well captured by the forecast system, the high frequency variability near the coastline was not so well captured. This could imply a possible effect from waves, especially the tidal wave. In general, the high frequency variability of observed temperature was substantially larger than the high frequency variability of model temperature as indicated by S_m^2/S_o^2.

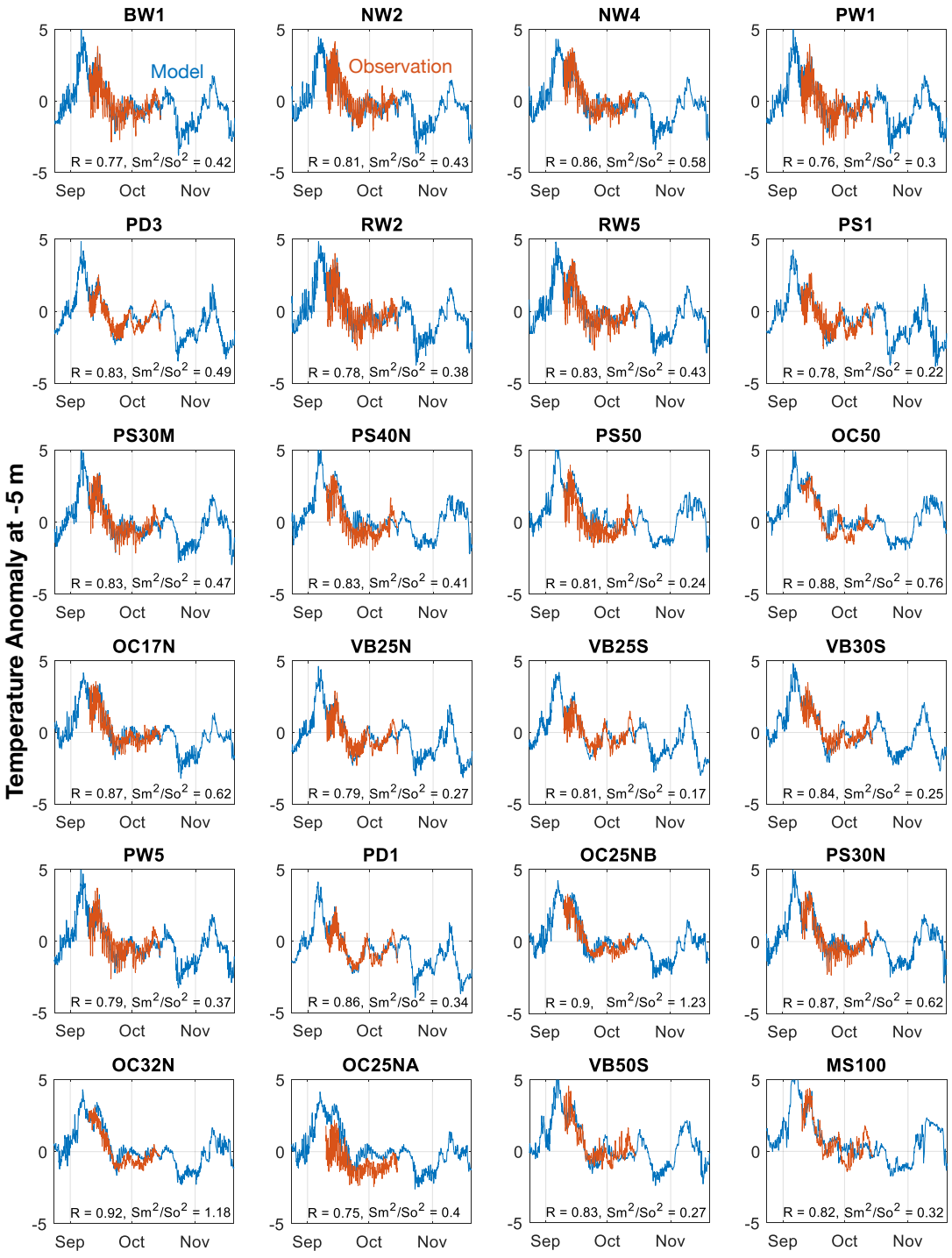

Figure 23. Temperature anomaly of 24 mooring sites at -5 m depth. Temperature anomaly was calculated by removing the regional mean temperature of 15.56°C from model temperature time series and removing the observational mean temperature of 14.70°C from observed temperature. R is the correlation coefficient, S_m^2/S_o^2 is the fraction of model temperature residual (total temperature subtracts the subtidal temperature) variance over observed temperature residual variance.

Temporal averaged stratification at the 24 mooring locations (Figure 24) also showed that the model stratification compared better with observed stratification in deeper innershelf mooring locations. The RMSE increased from offshore to onshore (OC50-OC32N-OC17N, MS100-PS50-PS30M-BW1, VB50S-VB30S-VB25S). In shallower mooring locations, model temperature was more stratified and less energetic than the observed temperature, which was consistent with the analysis drawn from the temperature time series at -5 m depth.

The peak temperature gradient revealed the depth where temperature dropped most significantly. According to the model stratification, these peak temperature gradients are mostly within 2- to 3-meter depth from the water surface. According to the observed temperature stratification, e.g., PW1, the depth of the peak temperature gradient was slightly deeper. In some other mooring locations, e.g., OC25NA, there were no obvious maximum temperature gradient. As shown, thermoclines in these mooring locations were brought to the surface possibly by upwelling, considered that the modeling and field measurement period is upwelling favorable.

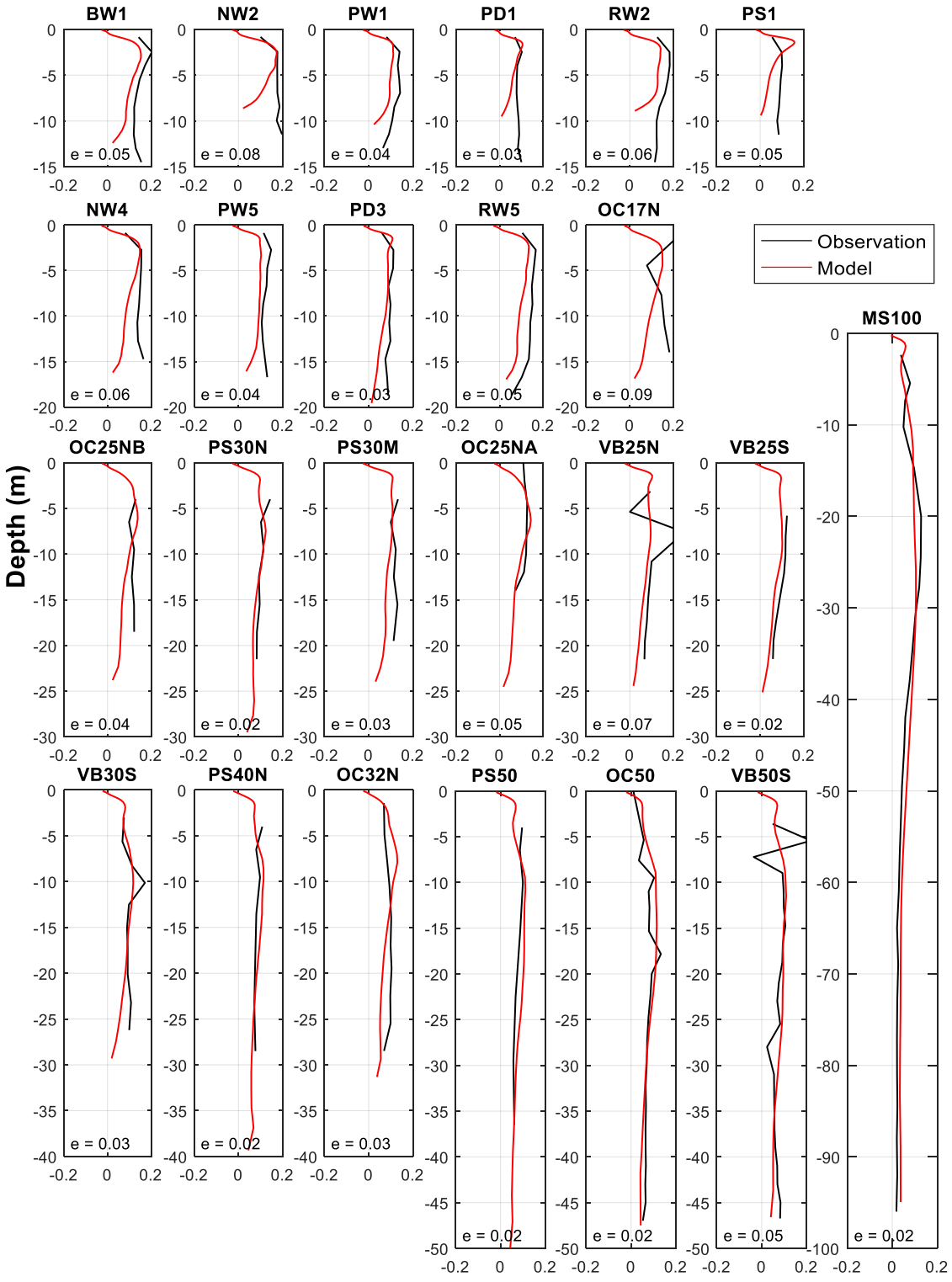

Figure 24. Temporal averaged stratification (dT/dz) profile at 24 mooring sites. e is the root mean square error between the model temperature and observed temperature.

Rotary velocity (u, v) spectra, separating clockwise (CW) and counterclockwise (CCW) motions (Gonella, 1972), were calculated for the depth averaged currents at mooring locations. There was no distinct asymmetry between CW and CCW motions in these mooring locations (not shown) potentially due to a stronger frictional response in the inner shelf (Kumar et al., 2015). Thus, the two motions were combined into the total rotary spectra (Figure 25).

In general, the observed total rotary spectra showed distinct peaks at diurnal and semidiurnal frequencies. Across the transect (MS100-PS50-PS40M-PS30M) near Pt. Sal., the energy density related to the diurnal frequency increased to the magnitude in the semidiurnal frequency, indicating a growing influence from the surface heat flux and diurnal wind oscillation. The same pattern was shown at PS30S closer to Pt. Sal. and across the transect (OC50-OC25NB) north of Pt. Sal. However, across the transect (VB50N-VB30N-VB25N) south of Pt. Sal., the energy related to the semidiurnal frequency became more significant from offshore to onshore. This pattern of the energy of semidiurnal frequency higher than the energy of diurnal frequency was also shown further south of Pt. Sal. (VB50S-VB30S). The increasing energy in the semidiurnal frequency might be contributed by the bay-like bathymetry featured by a sharp direction change in coastline and leading to higher resonance in the semidiurnal frequency. Overall, the energy related to the semidiurnal frequency became more prominent from the north to the south.

Comparisons between the model and the observation showed that the model slightly overestimated the energy in the low frequency band, i.e., the subtidal band (up to the diurnal frequency). Modeled and observed rotary spectra compared well in the diurnal band and in the semidiurnal frequency band. In the high frequency band (referred to frequencies

higher than the semidiurnal frequency band), modeled rotary spectra were weaker than the observed, consistent with Figure 23, potentially due to the lack of high-frequency surface and boundary forcing, and the limitation of the hydrostatic approximation, which might restrict the high-frequency variability (Kumar et al., 2015).

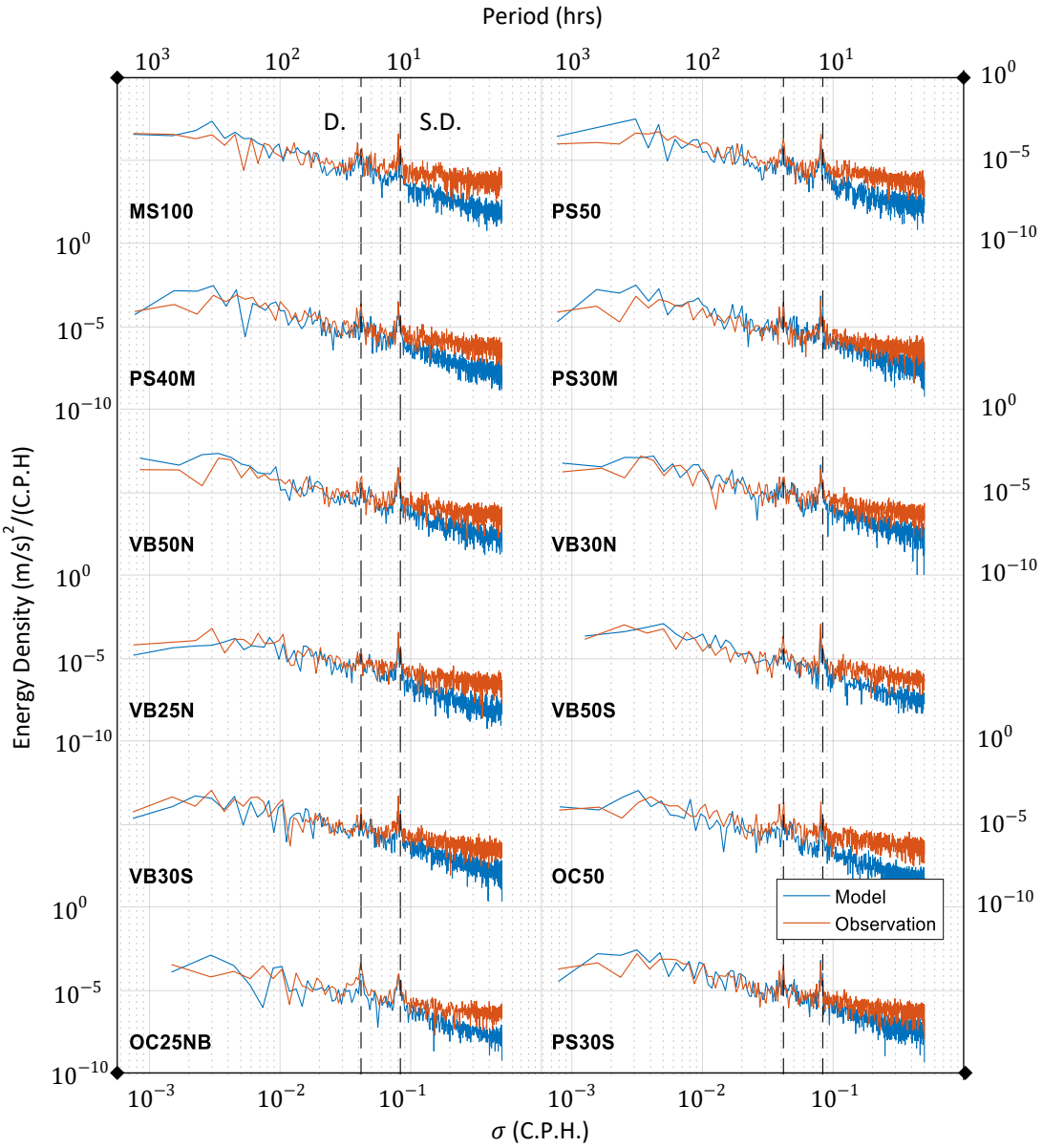

Figure 25. Total rotary spectra of the depth-averaged currents at mooring locations as a function of frequency (bottom axis) and period (top axis). Dashed lines represent diurnal frequency and semidiurnal frequency, respectively.

A summary assessment of model data comparison was shown in a Taylor diagram (Taylor, 2001) in which the standard deviations between the forecast and observed fields, their correlations, and their RMS difference were displayed (Figure 26). Statistics of the modeled temperature was closely concentrated inside a compact range, suggesting the stability of the temperature forecast. The normalized standard deviation varied from 0.8 to 1.2 with a mean difference of 25% from the reference point (unit standard deviation). Normalized RMS difference changed from 0.4 to 0.7, which was within one order of magnitude difference. The correlation was between 0.75 and 0.93, suggesting the modeled temperature were well correlated with the observation.

The modeled temperature was in general better simulated than the modeled currents. Statistics of modeled currents were in a broader range, especially in terms of the standard deviation. Across-shelf currents had standard deviations from 0.5 to 0.7 and along-shelf currents from 0.8 to 1.7, indicating that the across-shelf currents were underestimated and the along-shelf currents were overall overestimated. For correlation, along-shelf currents had correlations from 0.28 to 0.62, whereas the across-shelf currents had correlations from 0 to 0.45, suggesting the along-shelf velocities were better simulated. Along-shelf currents had RMS difference from 0.8 to 1.2, whereas across-shelf currents had RMS difference from 0.8 to 1.5, indicating that there was in general one order of magnitude difference between the model and observation. The deviation of the modeled trajectories from the observations might be partly owed to the unresolved internal variability, imperfect initial and forcing conditions.

As strong temporal coherence existed in the observed fields, meaning the potentially high similarity between today's field and tomorrow, we produced a surrogate forecast by

sliding the field of today to tomorrow, i.e., persistence 1-day forecast. Similarly, if we slid the field of today to the day after tomorrow, we obtained the persistence 2-day forecast. The persistence forecast (both 1-day and 2-day) had similar standard deviation but large variability in terms of correlation and RMS difference. Compared with model data comparison statistics, persistence 1-day forecast had almost perfect (~1) scale of standard deviation in all mooring locations, comparable correlation scale and comparable RMS difference scale. Persistence 2-day forecast had inferior statistics compared with persistence 1-day forecast. Correlation from temperature mooring stations decreased to as low as 0.5 and the RMS difference increased to as high as one magnitude difference. Overall, the performance of the model system on forecasting the future 24-48 hours was comparable with persistence 1-day forecast and was better than the persistence 2-day forecast, indicating the robustness and validity of our modeling framework.

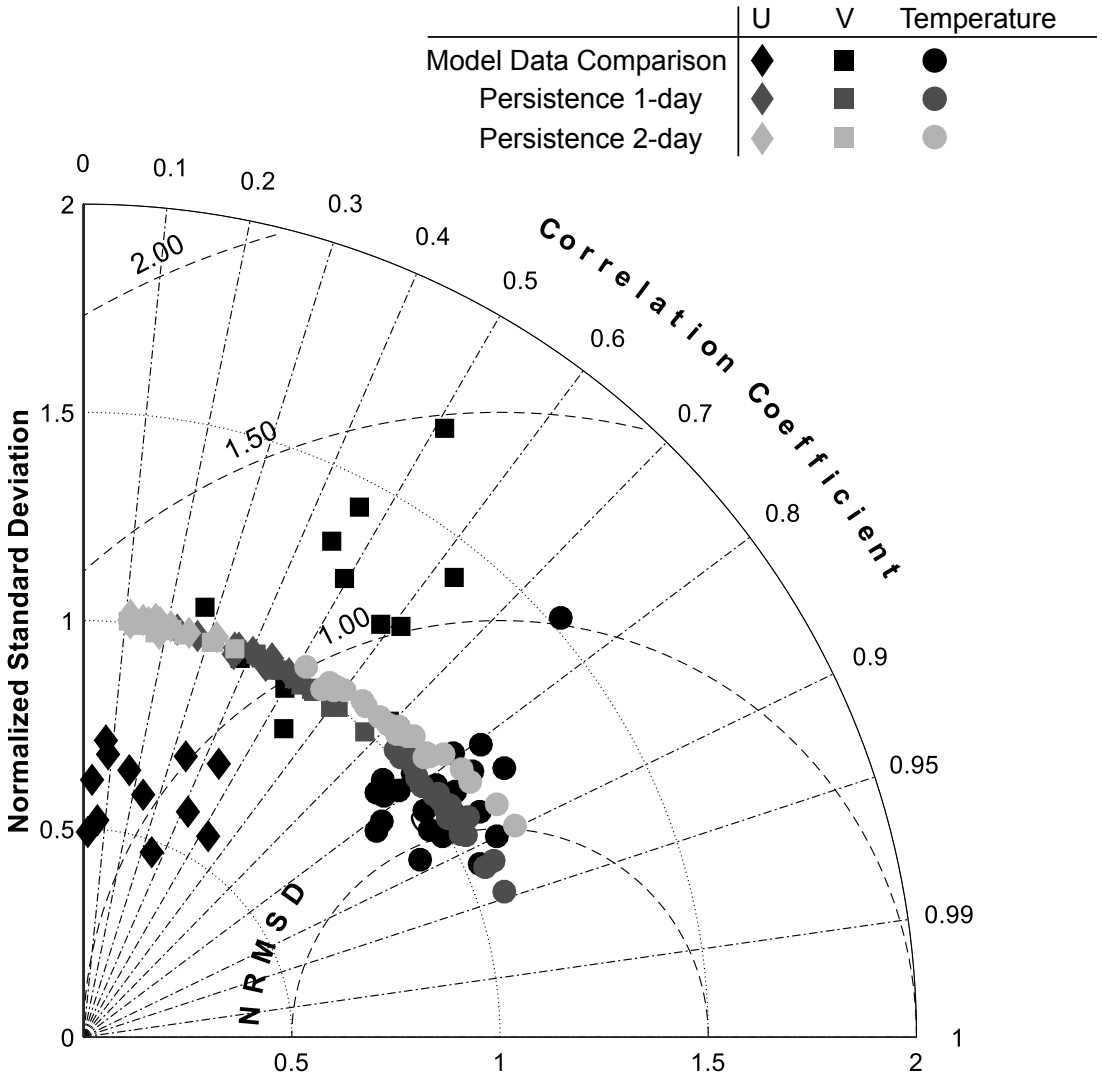

Figure 26. Taylor diagram to summarize the statistics of the forecast variables, including temperature (circle) of 24 stations, across-shelf (u; diamond) and along-shelf (v; square) current of 12 stations (locations as shown in Figure 21). Black color of the symbols represents the statistics calculated based on our second-day forecast (24–48-hour forecast) of the multi-grid forecast system. Dark gray represents the 1-day persistence forecast, and light gray represent the 2-day persistence forecast. The radial distances from the origin (0, 0) are proportional to the standard deviation of model normalized by the standard deviation of observation; the radial distances from (1, 0) represents the RMSE between the model and observation and normalized by the standard deviation of the observation; the azimuthal positions indicate the correlation coefficient.

4.4 Predictability of the Forecast System

4.4.1 Temporal Control of Input Forcings

To quantify the potential predictability induced by forcings as a function of the elapsed time, the RMS difference was analyzed between ensemble experiments and the control simulation for targeted variables (Figure 27). IC ensemble experiments were designed to replace the original initial forcing with the diurnal signal, resulting in huge differences to the control simulation at the start of modeled trajectories (Figure 27), consistent with the finding of Corti et al. (2015). As time elapsed, the impact of initial forcing was weakened rapidly and the difference between IC ensembles and the control simulation continuously decreased.

For the BC ensemble experiments, the boundary forcing was replaced by the diurnal signal while other forcings were identical as used in the control simulation. As such, the RMS difference was minimum at the beginning of elapsed time. As time evolved, the "wrong" boundary forcing continuously dragged the model trajectories away from the control simulation, resulting in increasing RMS difference. Similarly, the SBC ensemble also showed minimum RMS difference at the beginning and gradually increased with time.

Comparing the bottom variables (Figure 27b, d, e) with the surface (Figure 27a, c, f), the surface variables showed clear fluctuation of the RMS difference in the diurnal frequency (i.e., fluctuated every 24 hours), whereas the diurnal fluctuation was much less significant for those bottom variables.

Besides, it also showed a scale difference in the error induced by different types of forcing. Among the three groups of ensemble experiments, BC showed the largest growing error and the largest error variability (red line and shading in Figure 27), followed by SBC (black line and shading) and IC (blue line and shading). More specifically, we observed, for SST and BT, RMSE gradually changed as time evolved, indicating that the initial forcing still played a role on the temperature trajectories after some time. However, for both surface and bottom currents, there showed a prompt change immediately after the model initialized, suggesting that currents were extremely sensitive to the boundary forcing and less so to the initial forcing.

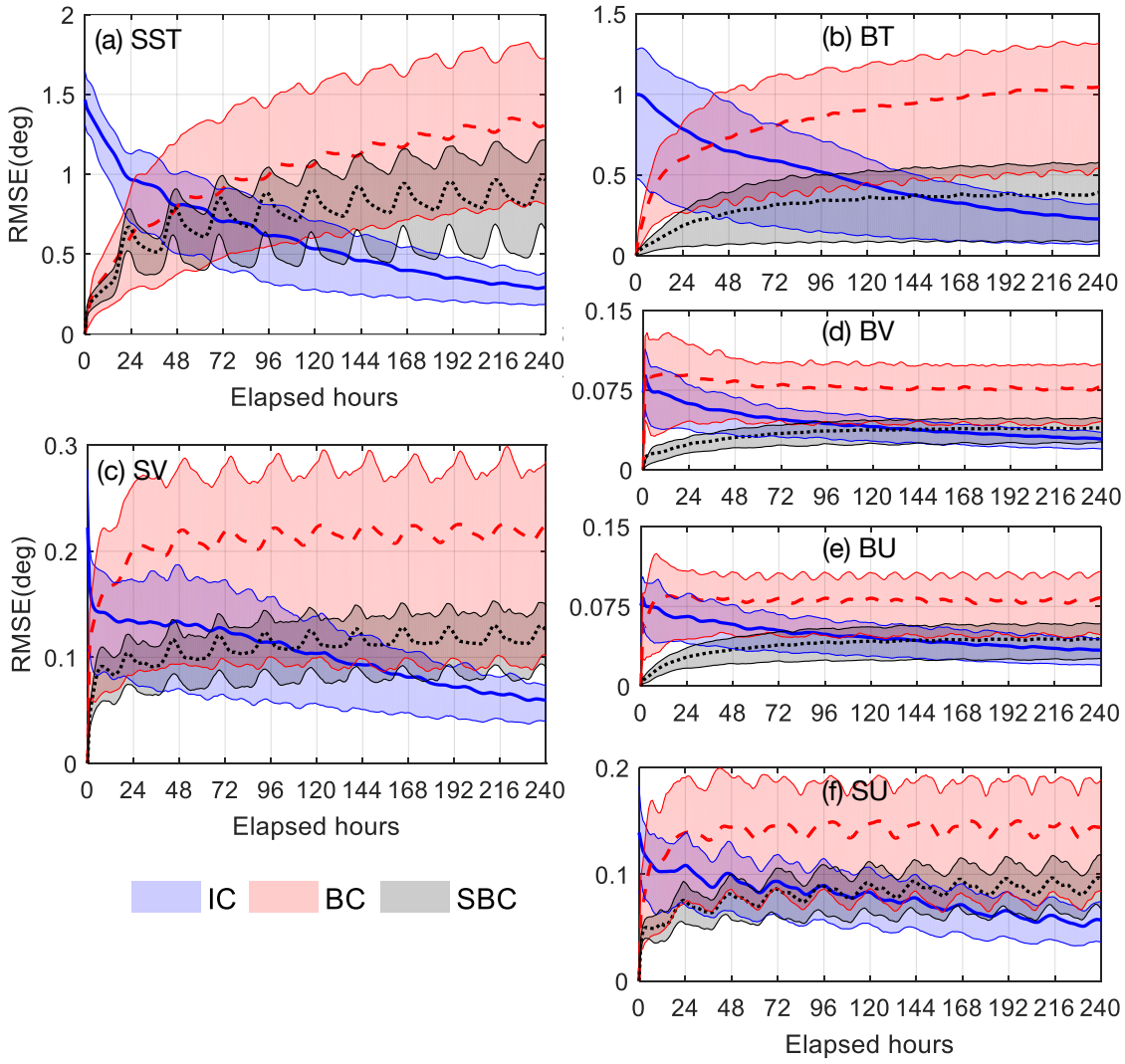

Figure 27. Ensemble mean and the 90% confidence interval of spatially-averaged RMS difference of targeted fields as a function of elapsed time. Targeted fields included (a) sea surface temperature (SST), (b) bottom temperature (BT), (c) surface along-shelf current (SV), (d) bottom along-shelf current (BV), (e) bottom cross-shelf current (BU) and (f) surface cross-shelf current (SU). RMS difference was between ensemble experiments and the control simulation.

The correlation of temperature (Figure 28a) between ensemble experiments and the control simulation showed that varying the initial forcing led to a broad range of correlation at the beginning of elapsed time, with worse correlation near the surface and near perfect correlation close to the topography bottom. As time continued to evolve, near the surface, the correlation improved greatly, whereas bottom temperature remained highly correlated. This indicated that the model initialization had a greater impact on the surface at the beginning of prediction, making the model trajectories start from a state with little similarity to the control simulation, whereas the bottom temperature was more robust and stable.

When the boundary forcing changed, surface temperature started to diverge from the "perfect" trajectory, worsening the correlation as time elapsed. However, the bottom temperature remained highly correlated to the control simulation, suggesting that the influence of boundary forcing on the bottom temperature was very limited. A similar pattern was shown by the SBC experiments. Also, the level of correlation decrease under the influence of surface forcing was weaker than the impact from the boundary forcing.

Overall, in terms of correlation, varying the forcings had little impact on the bottom temperature and growing impact from the bottom to the surface. Teng and Branstator (2011) also showed that the depth-integrated subsurface temperature had stronger and longer predictability than SST. Similar to the finding from the RMS difference analysis (Figure 27), IC showed largest initial error which decreased over time, whereas BC and SBC showed growing error and variability with error magnitude of BC exceeding SBC.

The correlation of the principal current component (along-shelf current) between ensembles and the control simulation (Figure 28b) showed a similar pattern: IC had worse correlation at the beginning and the correlation improved as time elapsed; BC and SBC had the perfect correlation at the beginning and then the correlation decreased. The difference between currents and temperature was that there was a narrower range of correlation variability over depth. This indicated that there was less variation of correlation over depth for current. Moreover, this suggested that the bottom currents were strongly affected by the forcings compared with bottom temperature.

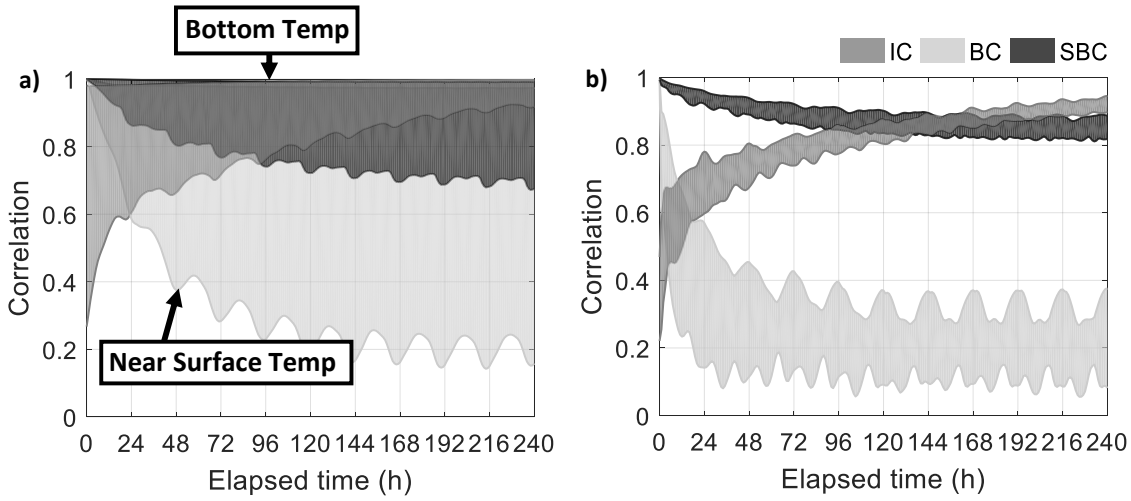

Figure 28. Correlation of (a) temperature and (b) currents between ensemble experiments and the control simulation from the bottom to the surface. The shaded areas represent the range and limits of the correlation.

As mentioned in 4.2.3, relative entropy considers both the mean signal and spreading in measuring the difference between predicted distribution and the distribution of control simulation. Due to the computation limitation in calculating an extremely large covariance matrix of a variable, we used kernel EOF (Schölkopf et al., 1997) to decompose the variable into its principal components. Total variance explained by principal components suggested that using the largest principal component (1PC) explains 75% of the total variance, while adding the second largest component (2PC) increased the variance explained by 11%. In general, the spatial distribution of the variance reconstructed from 1PC captured the total spatial pattern well (not shown). Thus, 1PC was considered sufficient for calculating the relative entropy.

Relative entropy of SST between IC and the control simulation (Figure 29a) was decreasing monotonically, asymptotically and rapidly to zero, suggesting that the impact of initialization dominates the field on the first day. Afterwards, the ensemble distribution became identical to the "perfect" model in the statistical aspect, meaning the domination of initialization vanishes. As an example, Branstator and Teng (2010) also showed the monotonic decrease in the relative entropy caused by the model initialization. But they studied the decadal predictability and concluded that the predictability impact could be up to 9 years. However, our study showed that the predictability of initialization was only about 1 day in a fine resolution regional model.

In the case of BC, the relative entropy was almost zero at the beginning of simulation period, suggesting that the ensemble distribution of BC began from being identical to the distribution of the "perfect" model. After that, relative entropy started to show fluctuation in diurnal frequency, indicating that SST started to react to the diurnal

signal continuously input to the system. Similarly, changing surface boundary forcing also led to zero relative entropy at the beginning and this entropy increased and fluctuated afterwards. According to relative entropy, BC and SBC shared a similar scale of predictability control of the system.

Relative entropy of BT (Figure 29b) showed that the impact of the initialization dropped down monotonically with time but did not vanish until after 5 days of simulation, showing a longer persistence of the initial forcing. Besides, relative entropy from BC increased over time, suggesting that the impact of the boundary forcing became the most significant. Whereas surface boundary forcing had minimum effect on BT throughout the simulation period.

Relative entropy of the currents (Figure 29c, d, e, f) showed that the surface forcing and the initial forcing had very limited impact, meaning the ensemble distribution of the SBC and IC was highly similar to the control simulation. Currents were strongly and potentially solely controlled by boundary forcing.

Overall, for the surface temperature, initial forcing had the strongest predictability impact over the other two conditions at the beginning, surface boundary forcing and boundary forcing shared the similar importance of predictability control afterwards; for the bottom temperature, surface boundary forcing had the least impact on predictability; for the currents, boundary forcing dominated the process of current trajectory evolution.

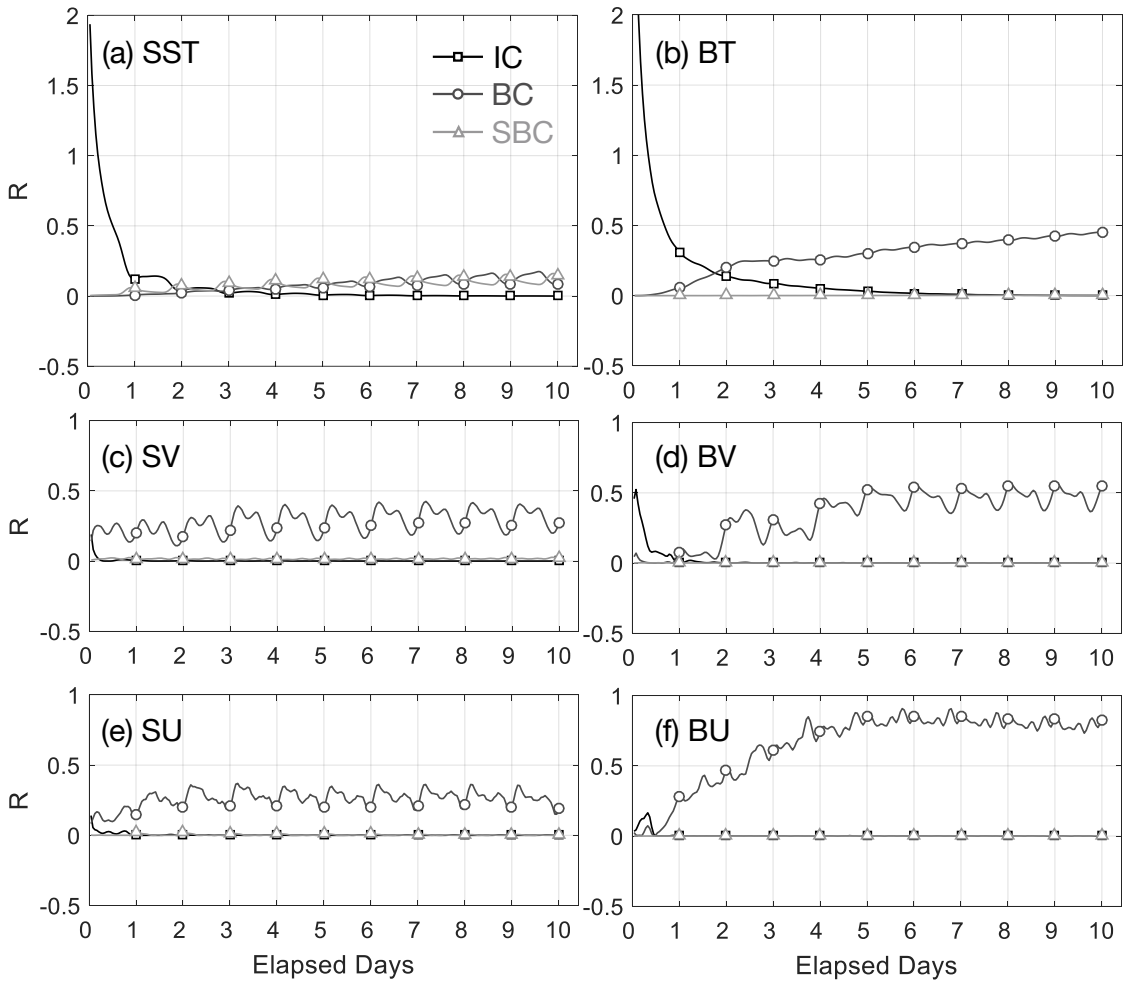

Figure 29. Relative entropy of (a) SST, (b) BT, (c) SV, (d) BV, (e) SU and (f) BU as a function of elapsed time.

4.4.2 Spatial Control of Input Forcings

In the previous analysis, spatially averaged and distribution integrated fields were analyzed to understand the temporal importance of initial, boundary and surface forcings. Here we quantified the spatial control to understand what area was more significantly affected by a specific type of forcing. We first calculated and showed the spatial distribution of RMS difference of SST between IC, BC, SBC and control simulation at different time stamps relative to the initialization (Figure 30).

For the IC ensembles, the RMS difference was significant at the beginning of the prediction period and then the error decreased as the modeled trajectories progressed (Figure 30a, d, g, j, m, p). More specifically, at 0.5 days after the initialization, the error was overall large within the entire simulated region (Figure 30a). Afterwards, the error gradually decreased along the southern and western boundary of the simulated region, and that decrease along the boundary gradually extended to the inner region (Figure 30d, g, j, m, p). The decrease of error extending from the southern boundary to the inner region was more pronounced than the decrease along the western boundary, suggesting the simulated region was more significantly affected by current flowing in and out of the southern boundary.

The BC ensembles showed patterns opposite to the IC ensembles (Figure 30b, e, h, k, n, q). At 0.5 days after the initialization, apparent RMS difference (>0.5 deg) started to appear along the southern and the western boundary (Figure 30b). And the error gradually propagated into the inner region (Figure 30e, h, k, n, q), especially through the southern boundary. Thus, this suggested that the flow from the south boundary had strong and large

variability and the impact penetrated to the very interior domain, making regions south of Point Sal under great influence from the south boundary forcing. Along the coastline north of Point Sal was protected from the influence of the boundary forcing possibly due to the "perfect" surface forcing.

SBC experiments showed very limited RMS difference within the entire simulated region at 0.5 days (Figure 30c) and along the southern and the western boundary afterwards (Figure 30f, i, l, o, r) due to the impact of "perfect" initial forcing and boundary forcing. The surface boundary forcing was mainly affecting the interior domain, more pronounced along the coastline north of Point Sal, which was shielded from the influence of boundary forcing.

Overall, initial forcing was only most pronounced within the entire simulated region for a short time after model initialization, whereas, afterwards, boundary forcing and surface boundary forcing shared the control of the simulation, with boundary forcing controlling large areas extending from the southern and the western boundaries and the surface forcing controlling the interior.

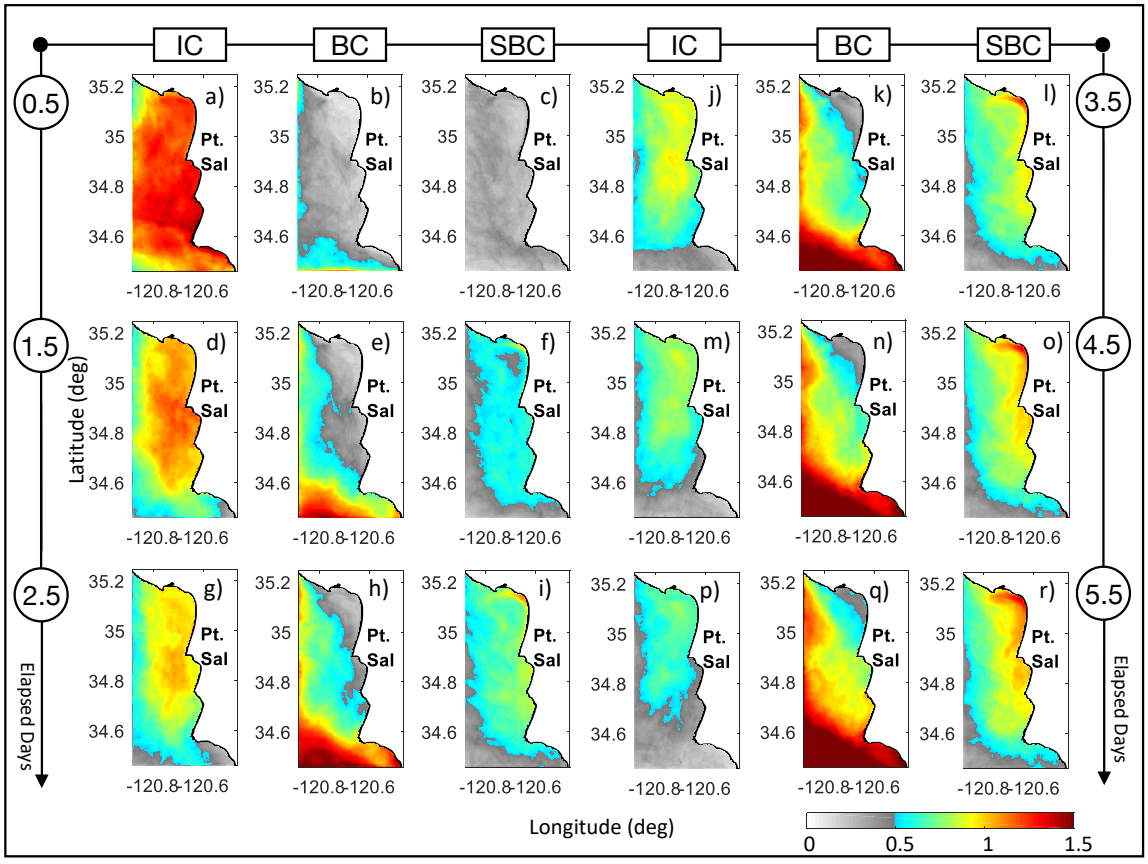

Figure 30. Spatial Distribution of Ensemble Averaged RMS difference of SST at each geographic location at different time steps from 0.5 days, 1.5 days, 2.5 days, 3.5 days, 4.5 days to 5.5 days. RMS difference of SST is ensemble-averaged for each group of ensemble experiments.

To give a definite answer as to which forcing had the strongest influence at a specific place and time, we defined a cross-over time (Figure 31, Corti et al. (2015)) as the timing when the impact of initial forcing was exceeded by the impact of surface boundary forcing (i.e., when the RMS difference from SBC ensembles became larger than that from IC), denoted as $\frac{SBC}{IC}$ and the timing when the impact of initial forcing was exceeded by the impact of boundary forcing, denoted as $\frac{BC}{IC}$. Calculating the cross-over time at each geographic location, we obtained a spatial map showing the relative importance of different forcings in the entire simulated region (Figure 32).

For SBC experiments targeting SST (Figure 32a), the cross-over time was nearly 2 days along the southern and the western boundary, and gradually increased to about 4 days near Point Sal and north of Point Sal. However, that short cross-over time along the boundary was not an indication of the influence of surface boundary forcing but the result of strong influence of boundary forcing, which we showed in Figure 30. From Figure 30 we demonstrated that the surface boundary forcing mainly had its influence in the interior domain, especially along the coastline north of Point Sal. The cross-over time along that narrow region was about 2 days.

For SBC experiments targeting BT (Figure 32c), the surface forcing influence was overall very limited, as the cross-over time in the interior domain was up to 8 days. Along the coastline, the cross-over time was about 2 to 4 days, potentially suggesting stronger influence from the surface forcing on shallow water depth.

For BC experiments targeting SST (Figure 32b), cross-over time was less than 2 days along the offshore boundary, especially along the southern boundary, indicating a

strong impact from the boundary forcing along the offshore boundary, consistent with Figure 30. The cross-over time gradually increased to up to 10 days from the offshore boundary to the interior, especially the coastline north of Point Sal.

For BC experiments targeting BT (Figure 32d), the pattern of cross-over time was in general similar to the pattern of cross-over time targeting SST, as the cross-over time was as short as 1 day along the offshore boundary and up to 8 days along the coastline north of Point Sal. The difference was that the impact from boundary forcing on BT extended a further distance into the domain, suggesting the lack of influence from surface forcing resulted in more dominant influence from boundary forcing.

Comparing the impact from SBC versus BC, and comparing the result on SST versus BT, we found that for SST, boundary forcing dominated the predictability along the offshore boundary and surface forcing dominated the impact in the interior domain, as the cross-over time of $\frac{\mathrm{BC}}{\mathrm{IC}}$ was shorter than the cross-over time of $\frac{\mathrm{SBC}}{\mathrm{IC}}$ along the offshore boundary and longer in the interior domain. For BT, the surface forcing was more restricted and dominated only along the coastline, leaving the boundary forcing in control of the majority of simulated domain.

Similar findings were seen regarding surface and bottom currents (Figure 32e, f, g, h, i, j, k, l): on the surface, boundary forcing had more control along the offshore boundary and surface forcing had dominant impact in the interior; on the bottom, boundary forcing had dominant control within almost the entire region, except a narrow band along the coastline controlled by the surface forcing.

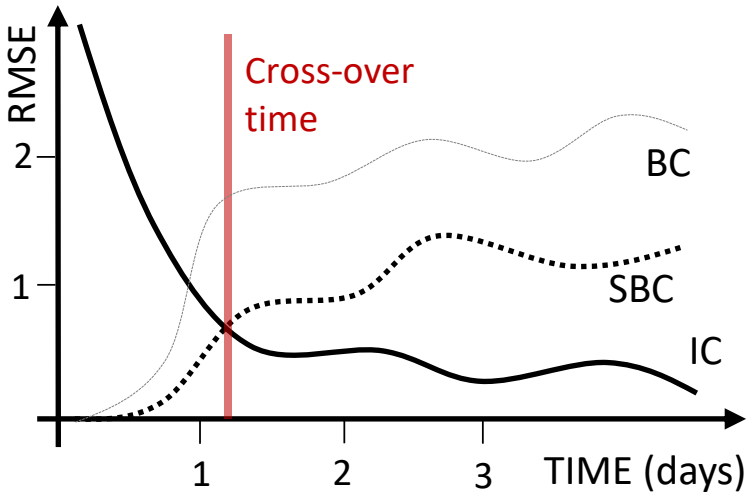

Figure 31. Schematic representation of the RMSE caused by forcings and the definition of cross-over time.

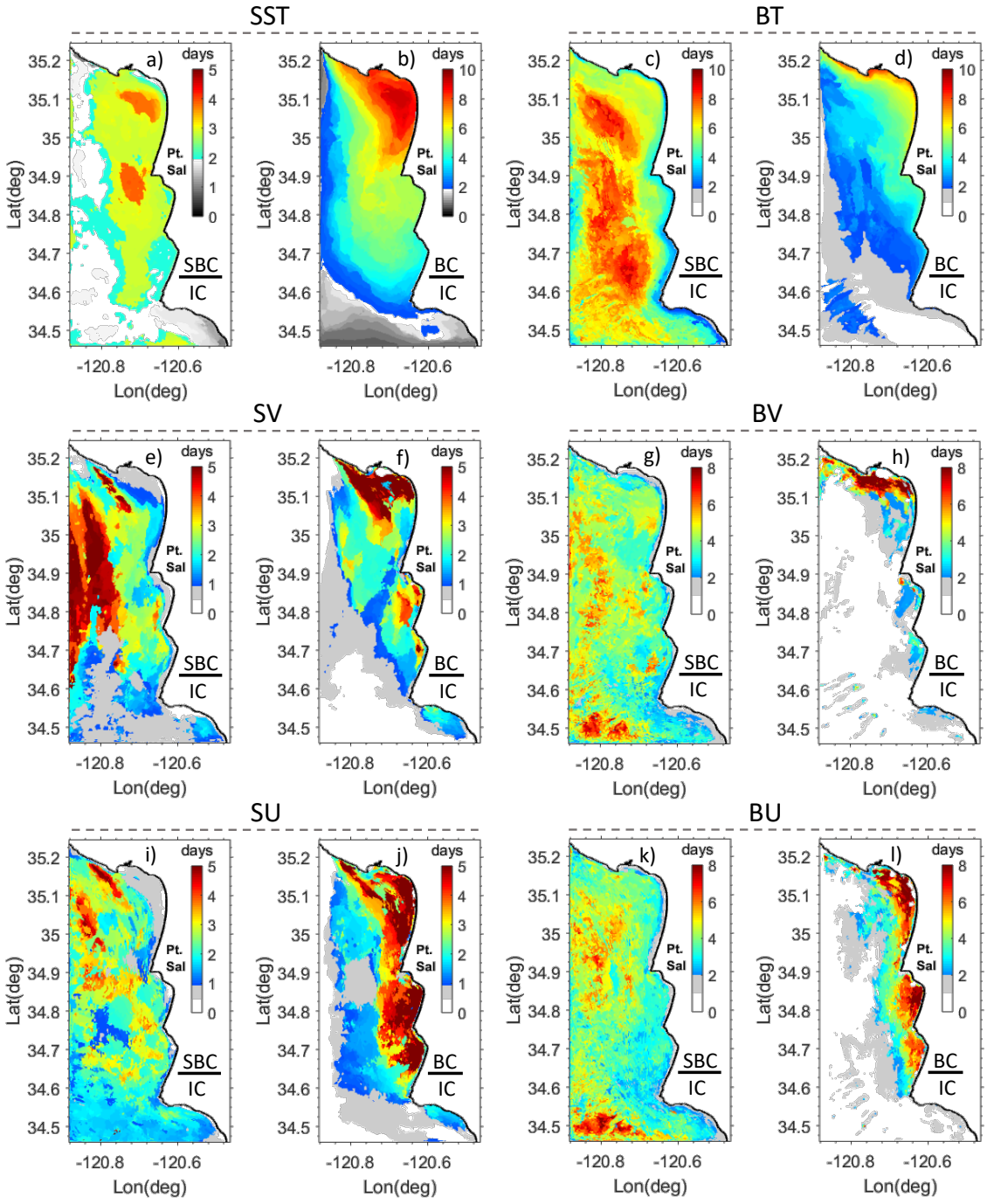

Figure 32. Spatial Distribution of cross-over time calculated from RMSE between SBC and IC, between BC and IC for variables (a, b) SST, (c, d) BT, (e, f) SV, (g, h) BV, (i, j) SU, (k, l) BU. $\frac{\mathbf{SBC}}{\mathbf{IC}}$ represents the timing when the impact of IC was exceeded by the impact of SBC; $\frac{\mathbf{BC}}{\mathbf{IC}}$ represents the timing when the impact of IC was exceeded by the impact of BC.

Next, we showed the spatial distribution of cross-over time calculated by relative entropy (Figure 33). This was done by treating each geographic location with the 100 ensembles as an independent distribution, calculating the relative entropy of each group of ensembles, and lastly calculating the cross-over time between one forcing with the other. Results showed that the cross-over time calculated based on relative entropy was overall consistent with the cross-over time calculated based on RMS difference. One difference was that, based on relative entropy, boundary forcings and surface forcings were sooner for taking over the control from the initial forcing, or in another words, a shorter persistence of the initial forcing.

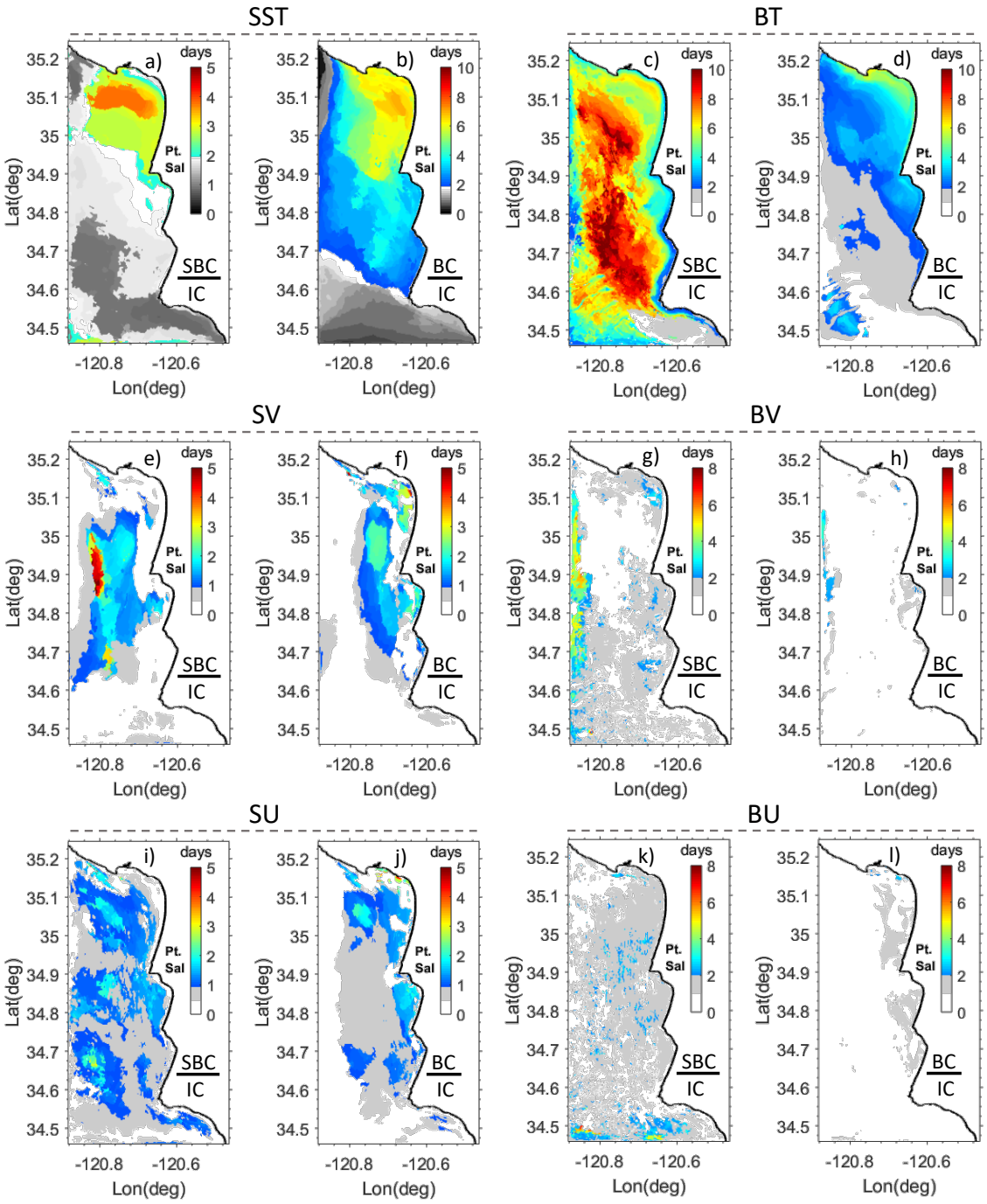

Figure 33. Spatial Distribution of cross-over time calculated from Relative Entropy between SBC and IC, between BC and IC for variables (a, b) SST, (c, d) BT, (e, f) SV, (g, h) BV, (i, j) SU, (k, l) BU.

4.5 Conclusion

An automatic forecast system was developed to conduct the multiple downscaling regional ocean model (3km → 1km → 600m → 200m) near Point Sal and to implement a 2-day forecast on a daily basis. We compared our forecast with the observed temperature and currents collected during the Fall 2017 Inner-shelf DRI field measurement campaign. Moreover, our real-time forecast was implemented on a daily basis in the Fall 2017, to assist the in-situ measurement. In general, the model prediction compared reasonably well to the observation. Furthermore, our forecast results were better than the persistence 2-day forecast, showing the validity of the developed forecast system.

Uncertainty of the system could propagate from system bias in the atmospheric prediction COAMPS system, interpolation error from coarse resolution to fine resolution, modeling error from downscaling inside the forecast system, etc. In our predictability study, it was assumed that the prediction trajectories of the 200m layer forecast system was the perfect representative of the nature. Under this assumption, the predictability study neglected the above uncertainty sources and concentrated on the impact of forcing versus the intrinsic variability of the system. Thus, prediction skill was dependent on initializing a climate model in the correct state of internal climate variations, imposing accurate external forcing and correctly simulating the evolution of the ocean system.

We studied the predictability of regional forecast near Point Sal by running 300 ensemble simulations with different initial forcing, boundary forcing, and surface forcing. According to our analysis on the temporal control of forcings, initial forcing had the most dominant control within the first 24 hours after model initialization. Afterwards, boundary

forcing and surface forcing shared their control on the ocean surface, whereas the bottom of the ocean was more dominant by boundary forcing. Spatial control of forcings showed again that the initial forcing controlled the predictability of the entire domain within the beginning 24 hours. After the 24 hours, on the ocean surface, boundary forcing dominated the predictability mostly along the offshore boundary, whereas surface forcing controlled the interior, especially along the coastline north of Point Sal. On the bottom of the ocean, surface forcing had very limited impact except along the coastline where the water depth was much shallower.

Now returning back to our *2-day* multi-grid forecast system, our findings of the predictability from different forcings suggested that, on the first day, initial forcing was the most important, and on the second day, the source of predictability was contributed by boundary forcing along the offshore boundary and surface forcing within the interior domain. Also, although our predictability study focused on a fine resolution grid (~200m grid) near Point Sal, our findings may be general and applicable to other near-real time coastal forecast models of similar temporal and spatial scales.

CHAPTER 5. CONCLUSION

This thesis work was motivated by the recurrent marine heatwaves and the ocean extremes in the North Pacific that have caused severe consequences to coastal ecosystems. This raised questions as to (0) how well we could model and represent the characteristics and statistical behaviors of North Pacific marine heatwaves, (0) how well we could forecast the coastal ocean conditions and understand the local versus remote control on the these coastal conditions, and (0) what the role of the fine-scale local coastal processes was on controlling the near-real time forecasts of a small area, continental-shelf coastal waters. To answer these questions, we developed multi-scales statistical and dynamical model frameworks, including the Linear Inverse Model (LIM) and the Regional Ocean Modeling System (ROMS).

In 0, we analyzed the composite evolution of observed Northeast Pacific marine heatwaves and reproduced the statistics and evolution of the observed by a large LIM ensemble, where each ensemble member was considered an alternative trajectory to what had already happened in the historical records. These alternatives provided us a large sample pool of simulated North Pacific marine heatwaves, which were then used to understand the link to the tropical Pacific and the role of climate change. Our result suggested that the durations of the Northeast Pacific marine heatwaves were linked to the tropical Pacific and, thus, indicated that these marine heatwaves had a predictable component. The intensities of the Northeast Pacific marine heatwaves were linked to the North Pacific variability, which was intrinsically unpredictable. As the background climatology became warmer, these Northeast Pacific marine heatwaves were projected to

occur more frequently in the future. Whether the higher frequency of occurrence was statistically significant remained to be explored.

In 0, we assessed the forecast skill of North Pacific coastal waters to understand how we predicted the ocean conditions relevant to the coastal ecosystem, if not just the ocean extremes. To that end, we constructed a LIM framework of the tropical Pacific and North Pacific SST and SSH, considering SSH as a proxy of subsurface ocean temperature. Our result showed that coastal waters of North Pacific eastern boundary had higher forecast skill than the coastal waters of western boundary. By retaining only the tropical forcing versus the North Pacific forcing in the LIM, we found that the high forecast skills along the North Pacific eastern boundary were dependent on both local dynamics and remote forcing by ocean and atmospheric tropical teleconnections. Specifically, local dynamic impact originated from the North Pacific SSH, i.e., memory from the subsurface ocean temperature, whereas the remote tropical Pacific forcing had equivalent control, or even slightly higher control along the lower latitude of North Pacific.

In 0, we developed a multi-grid near-real time ROMS forecast system to predict 48-hours ocean conditions near Pt. Sal, California. The multi-grid system included a grid with horizontal resolution of 3km, to 1km, 600m and 200m. The forecast system aimed to provide the future ocean conditions of the 200m grid on a daily basis and to help guide the in-situ measurement campaign at the time. Our forecast results compared well to the in-situ collected observation. We then designed ensemble sensitivity experiments forced by various initial forcing, boundary forcing and surface boundary forcing. These experiments were designed to understand the role of the very fine-scale local processes, which we assumed were contained in the initial forcing, compared to the role of the remote processes,

i.e., the boundary forcing. Through these experiments, we found that initial forcings had dominant control on evolution of the trajectory for no more than 48-hours, whereas the boundary forcing became the dominant source of influence afterwards.

In summary, this thesis had adopted both the statistical and dynamical modelling techniques from understanding large-scale phenomenon down to forecasting the ocean conditions of a fine-scale coastal region. These two techniques are the major and most important ocean modelling approaches (Jacox et al., 2020b). While the applications using these two techniques did not directly overlap in this thesis, they individually provided understanding of the involved dynamics. However, it is of interest to explore the consolidation of the two kinds for further improving multi-scale hybrid forecasting systems, Thus, in the follow-up studies, we plan to explore the statistical downscaling of the large-scale North Pacific LIM forecast to obtain fine resolution coastal state variables, which serve as inputs to drive the regional dynamical model for conducting seasonal forecast of coastal waters. We plan to expand the studies focusing on ocean extremes and forecast of the North Pacific to the entire globe. We plan to evaluate and construct a benchmark case of the hybrid California coastal water forecast driven by the statistically downscaled boundary forcing and later expand to the U.S. coastal waters.

REFERENCES

Alexander, M. A., Blade, I., Newman, M., Lanzante, J. R., Lau, N. C., and Scott, J. D., 2002, The atmospheric bridge: The influence of ENSO teleconnections on air-sea interaction over the global oceans: Journal of Climate, v. 15, no. 16, p. 2205-2231.

Alexander, M. A., and Deser, C., 1995, A Mechanism for the Recurrence of Wintertime Midlatitude Sst Anomalies: Journal of Physical Oceanography, v. 25, no. 1, p. 122-137.

Alexander, M. A., Deser, C., and Timlin, M. S., 1999, The reemergence of SST anomalies in the North Pacific Ocean: Journal of Climate, v. 12, no. 8, p. 2419-2433.

Alexander, M. A., Matrosova, L., Penland, C., Scott, J. D., and Chang, P., 2008, Forecasting Pacific SSTs: Linear inverse model predictions of the PDO: Journal of Climate, v. 21, no. 2, p. 385-402.

Alexander, M. A., Timlin, M. S., and Scott, J. D., 2001, Winter-to-winter recurrence of sea surface temperature, salinity and mixed layer depth anomalies: Progress in Oceanography, v. 49, no. 1-4, p. 41-61.

Amaya, D., Bond, N., Miller, A., and DeFlorio, M., 2016, The evolution and known atmospheric forcing mechanisms behind the 2013-2015 North Pacific warm anomalies: CLIVAR's Variations Newsletter, v. Spring, p. 1-6.

Amaya, D. J., 2019, The Pacific Meridional Mode and ENSO: a Review: Current Climate Change Reports, v. 5, no. 4, p. 296-307.

Amaya, D. J., Miller, A. J., Xie, S.-P., and Kosaka, Y., 2020, Physical drivers of the summer 2019 North Pacific marine heatwave: Nature Communications, v. 11, no. 1, p. 1903.

Anderson, B. T., Perez, R. C., and Karspeck, A., 2013, Triggering of El Nino onset through trade wind-induced charging of the equatorial Pacific: Geophysical Research Letters, v. 40, no. 6, p. 1212-1216.

Bahurel, P., 2006, Mercator Ocean Global to Regional Ocean Monitoring and Forecasting, *in* Chassignet, E. P., and Verron, J., eds., Ocean Weather Forecasting: An Integrated View of Oceanography: Dordrecht, Springer Netherlands, p. 381-395.

Balmaseda, M. A., Mogensen, K., and Weaver, A. T., 2013, Evaluation of the ECMWF ocean reanalysis system ORAS4: Quarterly Journal of the Royal Meteorological Society, v. 139, no. 674, p. 1132-1161.

Battisti, D. S., and Hirst, A. C., 1989, Interannual Variability in a Tropical Atmosphere Ocean Model - Influence of the Basic State, Ocean Geometry and Nonlinearity: Journal of the Atmospheric Sciences, v. 46, no. 12, p. 1687-1712.

Baxter, S., and Nigam, S., 2015, Key Role of the North Pacific Oscillation-West Pacific Pattern in Generating the Extreme 2013/14 North American Winter: Journal of Climate, v. 28, no. 20, p. 8109-8117.

Bell, M. J., Forbes, R. M., and Hines, A., 2000, Assessment of the FOAM global data assimilation system for real-time operational ocean forecasting: Journal of Marine Systems, v. 25, no. 1, p. 1-22.

Benthuysen, J. A., Oliver, E. C. J., Feng, M., and Marshall, A. G., 2018, Extreme Marine Warming Across Tropical Australia During Austral Summer 2015-2016: Journal of Geophysical Research-Oceans, v. 123, no. 2, p. 1301-1326.

Bjerknes, J., 1966, A possible response of the atmospheric Hadley circulation to equatorial anomalies of ocean temperature: Tellus, v. 18, no. 4, p. 820-829.

Bjerknes, J., 1968, Atmospheric teleconnections from the equatorial Pacific, Santa Monica,, Rand Corp., iii, 37 p. p.:

Bond, N. A., Cronin, M. F., Freeland, H., and Mantua, N., 2015, Causes and impacts of the 2014 warm anomaly in the NE Pacific: Geophysical Research Letters, v. 42, no. 9, p. 3414-3420.

Bond, N. A., Overland, J. E., Spillane, M., and Stabeno, P., 2003, Recent shifts in the state of the North Pacific: Geophysical Research Letters, v. 30, no. 23.

Branstator, G., and Teng, H. Y., 2010, Two Limits of Initial-Value Decadal Predictability in a CGCM: Journal of Climate, v. 23, no. 23, p. 6292-6311.

Brassington, G. B., Pugh, T., Spillman, C., Schulz, E., Beggs, H., Schiller, A., and Oke, P. R., 2007, BLUElink development of operational oceanography and servicing in Australia: Journal of Research and Practice in Information Technology, v. 39, no. 2, p. 151-164.

Brusdal, K., Brankart, J. M., Halberstadt, G., Evensen, G., Brasseur, P., van Leeuwen, P. J., Dombrowsky, E., and Verron, J., 2003, A demonstration of ensemble-based assimilation methods with a layered OGCM from the perspective of operational ocean forecasting systems: Journal of Marine Systems, v. 40, p. 253-289.

Capotondi, A., and Sardeshmukh, P. D., 2015, Optimal precursors of different types of ENSO events: Geophysical Research Letters, v. 42, no. 22, p. 9952-9960.

Capotondi, A., and Sardeshmukh, P. D., 2017, Is El Niño really changing?: Geophysical Research Letters, v. 44, no. 16, p. 8548-8556.

Capotondi, A., Sardeshmukh, P. D., Di Lorenzo, E., Subramanian, A. C., and Miller, A. J., 2019, Predictability of US West Coast Ocean Temperatures is not solely due to ENSO: Scientific Reports, v. 9, p. 10.

Carr, M. E., 2002, Estimation of potential productivity in Eastern Boundary Currents using remote sensing: Deep-Sea Research Part Ii-Topical Studies in Oceanography, v. 49, no. 1-3, p. 59-80.

Cavole, L. M., Demko, A. M., Diner, R. E., Giddings, A., Koester, I., Pagniello, C. M. L. S., Paulsen, M. L., Ramirez-Valdez, A., Schwenck, S. M., Yen, N. K., Zill, M. E., and Franks, P. J. S., 2016, Biological Impacts of the 2013-2015 Warm-Water Anomaly in the Northeast Pacific: Oceanography, v. 29, no. 2, p. 273-285.

Ceballos, L. I., Di Lorenzo, E., Hoyos, C. D., Schneider, N., and Taguchi, B., 2009, North Pacific Gyre Oscillation Synchronizes Climate Fluctuations in the Eastern and Western Boundary Systems: Journal of Climate, v. 22, no. 19, p. 5163-5174.

Chassignet, E. P., Hurlburt, H. E., Metzger, E. J., Smedstad, O. M., Cummings, J. A., Halliwell, G. R., Bleck, R., Baraille, R., Wallcraft, A. J., and Lozano, C., 2009, US GODAE: global ocean prediction with the HYbrid Coordinate Ocean Model (HYCOM): Oceanography, v. 22, no. 2, p. 64-75.

Chassignet, E. P., Hurlburt, H. E., Smedstad, O. M., Halliwell, G. R., Hogan, P. J., Wallcraft, A. J., Baraille, R., and Bleck, R., 2007, The HYCOM (HYbrid

Coordinate Ocean Model) data assimilative system: Journal of Marine Systems, v. 65, no. 1-4, p. 60-83.

Chavez, F. P., and Messie, M., 2009, A comparison of Eastern Boundary Upwelling Ecosystems: Progress in Oceanography, v. 83, no. 1-4, p. 80-96.

Chen, D. K., Lian, T., Fu, C. B., Cane, M. A., Tang, Y. M., Murtugudde, R., Song, X. S., Wu, Q. Y., and Zhou, L., 2015a, Strong influence of westerly wind bursts on El Nino diversity: Nature Geoscience, v. 8, no. 5, p. 339-345.

Chen, K., Gawarkiewicz, G., Kwon, Y. O., and Zhang, W. F. G., 2015b, The role of atmospheric forcing versus ocean advection during the extreme warming of the Northeast US continental shelf in 2012: Journal of Geophysical Research-Oceans, v. 120, no. 6, p. 4324-4339.

Chiang, J. C. H., and Vimont, D. J., 2004, Analogous Pacific and Atlantic meridional modes of tropical atmosphere-ocean variability: Journal of Climate, v. 17, no. 21, p. 4143-4158.

Clayson, C. A., and Weitlich, D., 2007, Variability of tropical diurnal sea surface temperature: Journal of Climate, v. 20, no. 2, p. 334-352.

Corti, S., Palmer, T., Balmaseda, M., Weisheimer, A., Drijfhout, S., Dunstone, N., Hazeleger, W., Kroger, J., Pohlmann, H., Smith, D., von Storch, J. S., and Wouters, B., 2015, Impact of Initial Conditions versus External Forcing in Decadal Climate Predictions: A Sensitivity Experiment*: Journal of Climate, v. 28, no. 11, p. 4454-4470.

Deser, C., Alexander, M. A., and Timlin, M. S., 1999, Evidence for a wind-driven intensification of the Kuroshio Current extension from the 1970s to the 1980s: Journal of Climate, v. 12, no. 6, p. 1697-1706.

Di Lorenzo, E., Cobb, K. M., Furtado, J. C., Schneider, N., Anderson, B. T., Bracco, A., Alexander, M. A., and Vimont, D. J., 2010, Central Pacific El Nino and decadal climate change in the North Pacific Ocean: Nature Geoscience, v. 3, no. 11, p. 762-765.

Di Lorenzo, E., Combes, V., Keister, J. E., Strub, P. T., Thomas, A. C., Franks, P. J. S., Ohman, M. D., Furtado, J. C., Bracco, A., Bograd, S. J., Peterson, W. T., Schwing, F. B., Chiba, S., Taguchi, B., Hormazabal, S., and Parada, C., 2013a, Synthesis of

Pacific Ocean Climate and Ecosystem Dynamics: Oceanography, v. 26, no. 4, p. 68-81.

Di Lorenzo, E., Liguori, G., Schneider, N., Furtado, J. C., Anderson, B. T., and Alexander, M. A., 2015, ENSO and meridional modes: A null hypothesis for Pacific climate variability: Geophysical Research Letters, v. 42, no. 21, p. 9440-9448.

Di Lorenzo, E., and Mantua, N., 2016, Multi-year persistence of the 2014/15 North Pacific marine heatwave: Nature Climate Change, v. 6, no. 11, p. 1042-+.

Di Lorenzo, E., Mountain, D., Batchelder, H. P., Bond, N., and Hofmann, E. E., 2013b, Advances in Marine Ecosystem Dynamics from US GLOBEC The Horizontal-Advection Bottom-up Forcing Paradigm: Oceanography, v. 26, no. 4, p. 22-33.

Di Lorenzo, E., and Ohman, M. D., 2013, A double-integration hypothesis to explain ocean ecosystem response to climate forcing: Proceedings of the National Academy of Sciences of the United States of America, v. 110, no. 7, p. 2496-2499.

Di Lorenzo, E., Schneider, N., Cobb, K. M., Franks, P. J. S., Chhak, K., Miller, A. J., McWilliams, J. C., Bograd, S. J., Arango, H., Curchitser, E., Powell, T. M., and Riviere, P., 2008, North Pacific Gyre Oscillation links ocean climate and ecosystem change: Geophysical Research Letters, v. 35, no. 8.

Dias, D. F., Subramanian, A., Zanna, L., and Miller, A. J., 2019, Remote and local influences in forecasting Pacific SST: a linear inverse model and a multimodel ensemble study: Climate Dynamics, v. 52, no. 5-6, p. 3183-3201.

Ding, H., Newman, M., Alexander, M. A., and Wittenberg, A. T., 2018, Skillful Climate Forecasts of the Tropical Indo-Pacific Ocean Using Model-Analogs: Journal of Climate, v. 31, no. 14, p. 5437-5459.

Dole, R. M., and Gordon, N. D., 1983, Persistent Anomalies of the Extratropical Northern Hemisphere Wintertime Circulation - Geographical-Distribution and Regional Persistence Characteristics: Monthly Weather Review, v. 111, no. 8, p. 1567-1586.

Doyle, J., Jiang, Q., Chao, Y., and Farrara, J., 2009, High-resolution atmospheric modeling over the Monterey Bay during AOSN II: Deep Sea Res. II, v. 56, p. 87-99.

Drevillon, M., Bourdalle-Badie, R., Derval, C., Drillet, Y., Lellouche, J. M., Remy, E., Tranchant, B., Benkiran, M., Greiner, L., Guinehut, S., Verbrugge, N., Garric, G., Testut, C. E., Laborie, M., Nouel, L., Bahurel, P., Bricaud, C., Crosnier, L., Dombrowsky, E., Durand, L., Ferry, N., Hernandez, F., Le Galloudec, O., Messal, F., and Parent, L., 2008, The GODAE/Mercator-Ocean global ocean forecasting system: results, applications and prospects: Journal of Operational Oceanography, v. 1, no. 1, p. 51-57.

Ezer, T., and Mellor, G. L., 1992, A Numerical Study of the Variability and the Separation of the Gulf-Stream, Induced by Surface Atmospheric Forcing and Lateral Boundary Flows: Journal of Physical Oceanography, v. 22, no. 6, p. 660-682.

Frankignoul, C., and Hasselmann, K., 1977, Stochastic climate models, Part II Application to sea-surface temperature anomalies and thermocline variability: Tellus, v. 29, no. 4, p. 289-305.

Frankignoul, C., and Reynolds, R. W., 1983, Testing a Dynamical Model for Mid-Latitude Sea Surface Temperature Anomalies: Journal of Physical Oceanography, v. 13, no. 7, p. 1131-1145.

Frischknecht, M., Munnich, M., and Gruber, N., 2015, Remote versus local influence of ENSO on the California Current System: Journal of Geophysical Research-Oceans, v. 120, no. 2, p. 1353-1374.

Frolicher, T. L., and Laufkotter, C., 2018, Emerging risks from marine heat waves: Nature Communications, v. 9, p. 4.

Gill, A. E., 1982, Atmosphere-ocean dynamics, New York, Academic Press, International geophysics series, xv, 662 p. p.:

Gonella, J., 1972, A rotary-component method for analysing meteorological and oceanographic vector time series: Deep Sea Research and Oceanographic Abstracts, v. 19, no. 12, p. 833-846.

Haidvogel, D. B., Arango, H., Budgell, W. P., Cornuelle, B. D., Curchitser, E., Di Lorenzo, E., Fennel, K., Geyer, W. R., Hermann, A. J., Lanerolle, L., Levin, J., McWilliams, J. C., Miller, A. J., Moore, A. M., Powell, T. M., Shchepetkin, A. F., Sherwood, C. R., Signell, R. P., Warner, J. C., and Wilkin, J., 2008, Ocean forecasting in terrain-following coordinates: Formulation and skill assessment of the Regional Ocean Modeling System: Journal of Computational Physics, v. 227, no. 7, p. 3595-3624.

Harrison, D., and Smith, N., 2002, Ocean observing systems and prediction - the next ten years.

Hartmann, D. L., 2015, Pacific sea surface temperature and the winter of 2014: Geophysical Research Letters, v. 42, no. 6, p. 1894-1902.

Hasselmann, K., 1976, Stochastic Climate Models .1. Theory: Tellus, v. 28, no. 6, p. 473-485.

Hervieux, G., Alexander, M. A., Stock, C. A., Jacox, M. G., Pegion, K., Becker, E., Castruccio, F., and Tommasi, D., 2019, More reliable coastal SST forecasts from the North American multimodel ensemble: Climate Dynamics, v. 53, no. 12, p. 7153-7168.

Hobday, A. J., Alexander, L. V., Perkins, S. E., Smale, D. A., Straub, S. C., Oliver, E. C. J., Benthuysen, J. A., Burrows, M. T., Donat, M. G., Peng, M., Holbrook, N. J., Moore, P. J., Scannell, H. A., Sen Gupta, A., and Wernberg, T., 2016, A hierarchical approach to defining marine heatwaves: Progress in Oceanography, v. 141, p. 227-238.

Hobday, A. J., Oliver, E. C. J., Sen Gupta, A., Benthuysen, J. A., Burrows, M. T., Donat, M. G., Holbrook, N. J., Moore, P. J., Thomsen, M. S., Wernberg, T., and Smale, D. A., 2018, Categorizing and Naming MARINE HEATWAVES: Oceanography, v. 31, no. 2, p. 162-173.

Hodur, R. M., Hong, X., Doyle, J. D., Pullen, J., Cummings, J., Martin, P., and Rennick, M. A., 2002, The coupled ocean/atmosphere mesoscale prediction system (COAMPS): NAVAL RESEARCH LAB MONTEREY CA.

Holbrook, N. J., Scannell, H. A., Sen Gupta, A., Benthuysen, J. A., Feng, M., Oliver, E. C. J., Alexander, L. V., Burrows, M. T., Donat, M. G., Hobday, A. J., Moore, P. J., Perkins-Kirkpatrick, S. E., Smale, D. A., Straub, S. C., and Wernberg, T., 2019, A global assessment of marine heatwaves and their drivers: Nature Communications, v. 10, p. 13.

Holbrook, N. J., Sen Gupta, A., Oliver, E. C. J., Hobday, A. J., Benthuysen, J. A., Scannell, H. A., Smale, D. A., and Wernberg, T., 2020, Keeping pace with marine heatwaves: Nature Reviews Earth & Environment.

Hu, Z. Z., Kumar, A., Jha, B., Zhu, J. S., and Huang, B. H., 2017, Persistence and Predictions of the Remarkable Warm Anomaly in the Northeastern Pacific Ocean during 2014-16: Journal of Climate, v. 30, no. 2, p. 689-702.

Jacox, M. G., Alexander, M. A., Bograd, S. J., and Scott, J. D., 2020a, Thermal displacement by marine heatwaves: Nature, v. 584, no. 7819, p. 82-86.

Jacox, M. G., Alexander, M. A., Siedlecki, S., Chen, K., Kwon, Y. O., Brodie, S., Ortiz, I., Tommasi, D., Widlansky, M. J., Barrie, D., Capotondi, A., Cheng, W., Di Lorenzo, E., Edwards, C., Fiechter, J., Fratantoni, P., Hazen, E. L., Hermann, A. J., Kumar, A., Miller, A. J., Pirhalla, D., Buil, M. P., Ray, S., Sheridan, S. C., Subramanian, A., Thompson, P., Thorne, L., Annamalai, H., Aydin, K., Bograd, S. J., Griffis, R. B., Kearney, K., Kim, H., Mariotti, A., Merrifield, M., and Rykaczewski, R., 2020b, Seasonal-to-interannual prediction of North American coastal marine ecosystems: Forecast methods, mechanisms of predictability, and priority developments: Progress in Oceanography, v. 183.

Jacox, M. G., Alexander, M. A., Stock, C. A., and Hervieux, G., 2019a, On the skill of seasonal sea surface temperature forecasts in the California Current System and its connection to ENSO variability: Climate Dynamics, v. 53, no. 12, p. 7519-7533.

Jacox, M. G., Tommasi, D., Alexander, M. A., Hervieux, G., and Stock, C. A., 2019b, Predicting the Evolution of the 2014-2016 California Current System Marine Heatwave From an Ensemble of Coupled Global Climate Forecasts: Frontiers in Marine Science, v. 6, p. 13.

Joh, Y., and Di Lorenzo, E., 2017, Increasing Coupling Between NPGO and PDO Leads to Prolonged Marine Heatwaves in the Northeast Pacific: Geophysical Research Letters, v. 44, no. 22, p. 11663-11671.

-, 2019, Interactions between Kuroshio Extension and Central Tropical Pacific lead to preferred decadal-timescale oscillations in Pacific climate: Scientific Reports, v. 9, p. 12.

Jones, T., Parrish, J. K., Peterson, W. T., Bjorkstedt, E. P., Bond, N. A., Ballance, L. T., Bowes, V., Hipfner, J. M., Burgess, H. K., Dolliver, J. E., Lindquist, K., Lindsey, J., Nevins, H. M., Robertson, R. R., Roletto, J., Wilson, L., Joyce, T., and Harvey, J., 2018, Massive Mortality of a Planktivorous Seabird in Response to a Marine Heatwave: Geophysical Research Letters, v. 45, no. 7, p. 3193-3202.

Kleeman, R., 2002, Measuring Dynamical Prediction Utility Using Relative Entropy: Journal of the Atmospheric Sciences, v. 59, no. 13, p. 2057-2072.

Kullback, S., and Leibler, R. A., 1951, On Information and Sufficiency: The Annals of Mathematical Statistics, v. 22, no. 1, p. 79-86, 78.

Kumar, N., Feddersen, F., Uchiyama, Y., McWilliams, J., and O'Reilly, W., 2015, Midshelf to Surfzone Coupled ROMS-SWAN Model Data Comparison of Waves, Currents, and Temperature: Diagnosis of Subtidal Forcings and Response: Journal of Physical Oceanography, v. 45, no. 6, p. 1464-1490.

Kumar, N., Lerczak, J. A., Xu, T., Waterhouse, A. F., Thomson, J., Terrill, E. J., Swann, C., Suanda, S. H., Spydell, M. S., Smit, P. B., Simpson, A., Romeiser, R., Pierce, S. D., de Paolo, T., Pal?czy, A., O?Dea, A., Nyman, L., Moum, J. N., Moulton, M., Moore, A. M., Miller, A. J., Mieras, R. S., Merrifield, S. T., Melville, K., McSweeney, J. M., MacMahan, J., MacKinnon, J. A., Lund, B. r., Di Lorenzo, E., Lenain, L., Kovatch, M., Janssen, T. T., Haney, S., Haller, M. C., Haas, K., Grimes, D. J., Graber, H. C., Gough, M. K., Fertitta, D. A., Feddersen, F., Edwards, C. A., Crawford, W., Colosi, J., Chickadel, C. C., Celona, S., Calantoni, J., Braithwaite, E. F., Becherer, J., Barth, J. A., and Ahn, S., 2020, The Inner-Shelf Dynamics Experiment: Bulletin of the American Meteorological Society, p. 1-77.

Kumar, N., Suanda, S. H., Colosi, J. A., Haas, K., Di Lorenzo, E., Miller, A. J., and Edwards, C. A., 2019, Coastal Semidiurnal Internal Tidal Incoherence in the Santa Maria Basin, California: Observations and Model Simulations: Journal of Geophysical Research-Oceans, v. 124, no. 7, p. 5158-5179.

Larson, S. M., and Kirtman, B. P., 2014, The Pacific Meridional Mode as an ENSO Precursor and Predictor in the North American Multimodel Ensemble: Journal of Climate, v. 27, no. 18, p. 7018-7032.

Laufkötter, C., Zscheischler, J., and Frölicher, T. L., 2020, High-impact marine heatwaves attributable to human-induced global warming: Science, v. 369, no. 6511, p. 1621.

Lavaniegos, B. E., and Ohman, M. D., 2003, Long-term changes in pelagic tunicates of the California Current: Deep-Sea Research Part Ii-Topical Studies in Oceanography, v. 50, no. 14-16, p. 2473-2498.

Liguori, G., and Di Lorenzo, E., 2018, Meridional Modes and Increasing Pacific Decadal Variability Under Anthropogenic Forcing: Geophysical Research Letters, v. 45, no. 2, p. 983-991.

Linkin, M. E., and Nigam, S., 2008, The north pacific oscillation-west Pacific teleconnection pattern: Mature-phase structure and winter impacts: Journal of Climate, v. 21, no. 9, p. 1979-1997.

Lluchbelda, D., Lluchcota, D. B., Hernandezvazquez, S., and Salinaszavala, C. A., 1992, Sardine Population Expansion in Eastern Boundary Systems of the Pacific-Ocean as Related to Sea-Surface Temperature: South African Journal of Marine Science-Suid-Afrikaanse Tydskrif Vir Seewetenskap, v. 12, p. 147-155.

Lorenz, E., 1975, Climate predictability: The physical basis of climate modeling.

Lorenz, E. N., 1963, Deterministic Nonperiodic Flow: Journal of Atmospheric Sciences, v. 20, no. 2, p. 130-141.

Mantua, N. J., Hare, S. R., Zhang, Y., Wallace, J. M., and Francis, R. C., 1997, A Pacific interdecadal climate oscillation with impacts on salmon production: Bulletin of the American Meteorological Society, v. 78, no. 6, p. 1069-1079.

Marta-Almeida, M., Cirano, M., Pereira, J., and Ruiz-Villarreal, M., 2010, Development of the Brazilian Operational Ocean Forecast System with the OOFε Python engine for model ROMS.

Marta-Almeida, M., Ruiz-Villarreal, M., Otero, P., Cobas, M., Peliz, A., Nolasco, R., Cirano, M., and Pereira, J., 2011, OOFε: A Python engine for automating regional and coastal ocean forecasts: Environmental Modelling & Software, v. 26, no. 5, p. 680-682.

Mason, E., Molemaker, J., Shchepetkin, A. F., Colas, F., McWilliams, J. C., and Sangra, P., 2010, Procedures for offline grid nesting in regional ocean models: Ocean Modelling, v. 35, no. 1-2, p. 1-15.

McCabe, R. M., Hickey, B. M., Kudela, R. M., Lefebvre, K. A., Adams, N. G., Bill, B. D., Gulland, F. M. D., Thomson, R. E., Cochlan, W. P., and Trainer, V. L., 2016, An unprecedented coastwide toxic algal bloom linked to anomalous ocean conditions: Geophysical Research Letters, v. 43, no. 19, p. 10366-10376.

McPhaden, M. J., 1999, Genesis and evolution of the 1997-98 El Nino: Science, v. 283, no. 5404, p. 950-954.

-, 2015, COMMENTARY: Playing hide and seek with El Nino: Nature Climate Change, v. 5, no. 9, p. 791-795.

Menkes, C. E., Lengaigne, M., Vialard, J., Puy, M., Marchesiello, P., Cravatte, S., and Cambon, G., 2014, About the role of Westerly Wind Events in the possible development of an El Nino in 2014: Geophysical Research Letters, v. 41, no. 18, p. 6476-6483.

Miller, A. J., Cayan, D. R., and White, W. B., 1998, A westward-intensified decadal change in the North Pacific thermocline and gyre-scale circulation: Journal of Climate, v. 11, no. 12, p. 3112-3127.

Miller, A. J., and Schneider, N., 2000, Interdecadal climate regime dynamics in the North Pacific Ocean: theories, observations and ecosystem impacts: Progress in Oceanography, v. 47, no. 2-4, p. 355-379.

Miller, R. L., Lackmann, G. M., and Robinson, W. A., 2020, A New Variable-Threshold Persistent Anomaly Index: Northern Hemisphere Anomalies in the ERA-Interim Reanalysis: Monthly Weather Review, v. 148, no. 1, p. 43-62.

Mills, K. E., Pershing, A. J., Brown, C. J., Chen, Y., Chiang, F. S., Holland, D. S., Lehuta, S., Nye, J. A., Sun, J. C., Thomas, A. C., and Wahle, R. A., 2013, Fisheries Management in a Changing Climate Lessons from the 2012 Ocean Heat Wave in the Northwest Atlantic: Oceanography, v. 26, no. 2, p. 191-195.

Miyasaka, T., Nakamura, H., Taguchi, B., and Nonaka, M., 2014, Multidecadal modulations of the low-frequency climate variability in the wintertime North Pacific since 1950: Geophysical Research Letters, v. 41, no. 8, p. 2948-2955.

Mizuno, K., and White, W. B., 1983, Annual and Interannual Variability in the Kuroshio Current System: Journal of Physical Oceanography, v. 13, no. 10, p. 1847-1867.

Nellemann, C., Hain, S., and Alder, J., 2008, In dead water: merging of climate change with pollution, over-harvest, and infestations in the world's fishing grounds, UNEP/Earthprint.

Newman, M., Alexander, M. A., Ault, T. R., Cobb, K. M., Deser, C., Di Lorenzo, E., Mantua, N. J., Miller, A. J., Minobe, S., Nakamura, H., Schneider, N., Vimont, D. J., Phillips, A. S., Scott, J. D., and Smith, C. A., 2016, The Pacific Decadal Oscillation, Revisited: Journal of Climate, v. 29, no. 12, p. 4399-4427.

Newman, M., Alexander, M. A., and Scott, J. D., 2011a, An empirical model of tropical ocean dynamics: Climate Dynamics, v. 37, no. 9-10, p. 1823-1841.

Newman, M., Compo, G. P., and Alexander, M. A., 2003, ENSO-forced variability of the Pacific decadal oscillation: Journal of Climate, v. 16, no. 23, p. 3853-3857.

Newman, M., and Sardeshmukh, P. D., 2017, Are we near the predictability limit of tropical Indo-Pacific sea surface temperatures?: Geophysical Research Letters, v. 44, no. 16, p. 8520-8529.

Newman, M., Shin, S. I., and Alexander, M. A., 2011b, Natural variation in ENSO flavors: Geophysical Research Letters, v. 38, p. 7.

Oliver, E. C. J., 2019, Mean warming not variability drives marine heatwave trends: Climate Dynamics, v. 53, no. 3-4, p. 1653-1659.

Oliver, E. C. J., Benthuysen, J. A., Bindoff, N. L., Hobday, A. J., Holbrook, N. J., Mundy, C. N., and Perkins-Kirkpatrick, S. E., 2017, The unprecedented 2015/16 Tasman Sea marine heatwave: Nature Communications, v. 8.

Oliver, E. C. J., Benthuysen, J. A., Darmaraki, S., Donat, M. G., Hobday, A. J., Holbrook, N. J., Schlegel, R. W., and Gupta, A. S., 2021, Marine Heatwaves: Annual Review of Marine Science, v. 13, no. 1, p. null.

Oliver, E. C. J., Donat, M. G., Burrows, M. T., Moore, P. J., Smale, D. A., Alexander, L. V., Benthuysen, J. A., Feng, M., Sen Gupta, A., Hobday, A. J., Holbrook, N. J., Perkins-Kirkpatrick, S. E., Scannell, H. A., Straub, S. C., and Wernberg, T., 2018, Longer and more frequent marine heatwaves over the past century: Nature Communications, v. 9, p. 12.

Overland, J. E., Alheit, J., Bakun, A., Hurrell, J. W., Mackas, D. L., and Miller, A. J., 2010, Climate controls on marine ecosystems and fish populations: Journal of Marine Systems, v. 79, no. 3-4, p. 305-315.

Peng, W. Y., Chen, Q. L., Zhou, S. J., and Huang, P., 2021, CMIP6 model-based analog forecasting for the seasonal prediction of sea surface temperature in the offshore area of China: Geoscience Letters, v. 8, no. 1.

Penland, C., and Matrosova, L., 1994, A Balance Condition for Stochastic Numerical-Models with Application to the El-Nino-Southern Oscillation: Journal of Climate, v. 7, no. 9, p. 1352-1372.

Penland, C., and Sardeshmukh, P. D., 1995, The Optimal-Growth of Tropical Sea-Surface Temperature Anomalies: Journal of Climate, v. 8, no. 8, p. 1999-2024.

Pinardi, N., Allen, I., Demirov, E., De Mey, P., Korres, G., Lascaratos, A., Le Traon, P. Y., Maillard, C., Manzella, G., and Tziavos, C., 2003, The Mediterranean ocean forecasting system: first phase of implementation (1998-2001): Annales Geophysicae, v. 21, no. 1, p. 3-20.

Qiu, B., 2000, Interannual variability of the Kuroshio Extension system and its impact on the wintertime SST field: Journal of Physical Oceanography, v. 30, no. 6, p. 1486-1502.

-, 2003, Kuroshio Extension variability and forcing of the Pacific decadal oscillations: Responses and potential feedback: Journal of Physical Oceanography, v. 33, no. 12, p. 2465-2482.

-, 2019, Kuroshio and Oyashio Currents, London, Academic Press Ltd-Elsevier Science Ltd, Encyclopedia of Ocean Sciences, Vol 3: Ocean Dynamics, 3rd Edition, 384-394 p.:

Qiu, B., and Chen, S. M., 2005, Variability of the Kuroshio Extension jet, recirculation gyre, and mesoscale eddies on decadal time scales: Journal of Physical Oceanography, v. 35, no. 11, p. 2090-2103.

-, 2010, Eddy-mean flow interaction in the decadally modulating Kuroshio Extension system: Deep-Sea Research Part Ii-Topical Studies in Oceanography, v. 57, no. 13-14, p. 1098-1110.

Qiu, B., Chen, S. M., Schneider, N., and Taguchi, B., 2014, A Coupled Decadal Prediction of the Dynamic State of the Kuroshio Extension System: Journal of Climate, v. 27, no. 4, p. 1751-1764.

Quan, X., Hoerling, M., Whitaker, J., Bates, G., and Xu, T., 2006, Diagnosing sources of US seasonal forecast skill: Journal of Climate, v. 19, no. 13, p. 3279-3293.

Rayner, N. A., Parker, D. E., Horton, E. B., Folland, C. K., Alexander, L. V., Rowell, D. P., Kent, E. C., and Kaplan, A., 2003, Global analyses of sea surface temperature, sea ice, and night marine air temperature since the late nineteenth century: Journal of Geophysical Research-Atmospheres, v. 108, no. D14.

Reichler, T. J., and Roads, J. O., 2003, The role of boundary and initial conditions for dynamical seasonal predictability: Nonlinear Processes in Geophysics, v. 10, no. 3, p. 211-232.

Ryan, J. P., Kudela, R. M., Birch, J. M., Blum, M., Bowers, H. A., Chavez, F. P., Doucette, G. J., Hayashi, K., Marin, R., Mikulski, C. M., Pennington, J. T., Scholin, C. A., Smith, G. J., Woods, A., and Zhang, Y., 2017, Causality of an extreme harmful algal bloom in Monterey Bay, California, during the 2014-2016 northeast Pacific warm anomaly: Geophysical Research Letters, v. 44, no. 11, p. 5571-5579.

Sanford, E., Sones, J. L., García-Reyes, M., Goddard, J. H. R., and Largier, J. L., 2019, Widespread shifts in the coastal biota of northern California during the 2014–2016 marine heatwaves: Scientific Reports, v. 9, no. 1.

Santora, J. A., Mantua, N. J., Schroeder, I. D., Field, J. C., Hazen, E. L., Bograd, S. J., Sydeman, W. J., Wells, B. K., Calambokidis, J., Saez, L., Lawson, D., and Forney, K. A., 2020, Habitat compression and ecosystem shifts as potential links between marine heatwave and record whale entanglements: Nature Communications, v. 11, no. 1.

Sasaki, Y. N., and Schneider, N., 2011, Decadal Shifts of the Kuroshio Extension Jet: Application of Thin-Jet Theory: Journal of Physical Oceanography, v. 41, no. 5, p. 979-993.

Scannell, H. A., Pershing, A. J., Alexander, M. A., Thomas, A. C., and Mills, K. E., 2016, Frequency of marine heatwaves in the North Atlantic and North Pacific since 1950: Geophysical Research Letters, v. 43, no. 5, p. 2069-2076.

Schneider, N., and Cornuelle, B. D., 2005, The forcing of the Pacific decadal oscillation: Journal of Climate, v. 18, no. 21, p. 4355-4373.

Schneider, N., and Miller, A. J., 2001, Predicting western North Pacific Ocean climate: Journal of Climate, v. 14, no. 20, p. 3997-4002.

Schölkopf, B., Smola, A., and Müller, K.-R., Kernel principal component analysis, *in* Proceedings Artificial Neural Networks — ICANN'97, Berlin, Heidelberg, 1997// 1997, Springer Berlin Heidelberg, p. 583-588.

Schopf, P. S., and Suarez, M. J., 1988, Vacillations in a Coupled Ocean Atmosphere Model: Journal of the Atmospheric Sciences, v. 45, no. 3, p. 549-566.

Shchepetkin, A. F., and McWilliams, J. C., 2005, The regional oceanic modeling system (ROMS): a split-explicit, free-surface, topography-following-coordinate oceanic model: Ocean Modelling, v. 9, no. 4, p. 347-404.

Sherman, K. A., Lm, 1986, Variability and Management of Large Marine Ecosystems: Westview Press, Boulder.

Shin, S. I., and Newman, M., 2021, Seasonal Predictability of Global and North American Coastal Sea Surface Temperature and Height Anomalies: Geophysical Research Letters, v. 48, no. 10.

Shin, S. I., Sardeshmukh, P. D., Newman, M., Penland, C., and Alexander, M., 2020, Impact of Annual Cycle on ENSO Variability and Predictability: submitted to Journal of Climate.

Shin, S. I., Sardeshmukh, P. D., Newman, M., Penland, C., and Alexander, M. A., 2021, Impact of Annual Cycle on ENSO Variability and Predietability: Journal of Climate, v. 34, no. 1, p. 171-193.

Sieck, K., and Jacob, D., 2016, Influence of the boundary forcing on the internal variability of a regional climate model: American Journal of Climate Change, v. 5, no. 03, p. 373.

Smedstad, O., Cummings, J., Metzger, E., Hurlburt, H., Wallcraft, A., Franklin, D., Shriver, J., and Thoppil, P., 2010, The 1/12 degree Global HYCOM Nowcast/Forecast System.

Smith, T. M., Reynolds, R. W., Peterson, T. C., and Lawrimore, J., 2008, Improvements to NOAA's historical merged land-ocean surface temperature analysis (1880-2006): Journal of Climate, v. 21, no. 10, p. 2283-2296.

Sriver, R. L., Forest, C. E., and Keller, K., 2015, Effects of initial conditions uncertainty on regional climate variability: An analysis using a low-resolution CESM ensemble: Geophysical Research Letters, v. 42, no. 13, p. 5468-5476.

Stock, C. A., Pegion, K., Vecchi, G. A., Alexander, M. A., Tommasi, D., Bond, N. A., Fratantoni, P. S., Gudgel, R. G., Kristiansen, T., O'Brien, T. D., Xue, Y., and Yang, X. S., 2015, Seasonal sea surface temperature anomaly prediction for coastal ecosystems: Progress in Oceanography, v. 137, p. 219-236.

Strub, P. T., Allen, J. S., Huyer, A., Smith, R. L., and Beardsley, R. C., 1987, Seasonal Cycles of Currents, Temperatures, Winds, and Sea-Level over the Northeast Pacific Continental-Shelf - 35-Degrees-N to 48-Degrees-N: Journal of Geophysical Research-Oceans, v. 92, no. C2, p. 1507-1526.

Suanda, S. H., Feddersen, F., and Kumar, N., 2017, The Effect of Barotropic and Baroclinic Tides on Coastal Stratification and Mixing: Journal of Geophysical Research-Oceans, v. 122, no. 12, p. 10156-10173.

Suanda, S. H., Kumar, N., Miller, A. J., Di Lorenzo, E., Haas, K., Cai, D. H., Edwards, C. A., Washburn, L., Fewings, M. R., Torres, R., and Feddersen, F., 2016, Wind relaxation and a coastal buoyant plume north of Pt. Conception, CA: Observations, simulations, and scalings: Journal of Geophysical Research-Oceans, v. 121, no. 10, p. 7455-7475.

Swain, D. L., Tsiang, M., Haugen, M., Singh, D., Charland, A., Rajaratnam, B., and Diffenbaugh, N. S., 2014, The Extraordinary California Drought of 2013/2014: Character, Context, and the Role of Climate Change: Bulletin of the American Meteorological Society, v. 95, no. 9, p. S3-S7.

Tanahashi, S., Kawamura, H., Takahashi, T., and Yusa, H., 2003, Diurnal variations of sea surface temperature over the wide-ranging ocean using VISSR on board GMS: Journal of Geophysical Research-Oceans, v. 108, no. C7.

Taylor, K. E., 2001, Summarizing multiple aspects of model performance in a single diagram.: Journal of Geophysical Research-Atmospheres, v. 106, no. D7, p. 7183-7192.

Teng, H. Y., and Branstator, G., 2011, Initial-value predictability of prominent modes of North Pacific subsurface temperature in a CGCM: Climate Dynamics, v. 36, no. 9-10, p. 1813-1834.

Tommasi, D., Stock, C. A., Alexander, M. A., Yang, X., Rosati, A., and Vecchi, G. A., 2017, Multi-Annual Climate Predictions for Fisheries: An Assessment of Skill of Sea Surface Temperature Forecasts for Large Marine Ecosystems: Frontiers in Marine Science, v. 4, no. 201.

Traon, P.-Y., Rienecker, M., Smith, N., Bahurel, P., and Bell, M., 1999, Operational Oceanography and Prediction - A GODAE Perspective, p. 23.

Trenberth, K. E., and Hurrell, J. W., 1994, Decadal Atmosphere-Ocean Variations in the Pacific: Climate Dynamics, v. 9, no. 6, p. 303-319.

Vallis, G. K., 2017, Atmospheric and Oceanic Fluid Dynamics Fundamentals and Large-Scale Circulation Second Edition Preface: Atmospheric and Oceanic Fluid Dynamics: Fundamentals and Large-Scale Circulation, 2nd Edition, p. Xiii-+.

Vandendool, H. M., 1994, Searching for Analogs, How Long Must We Wait: Tellus Series a-Dynamic Meteorology and Oceanography, v. 46, no. 3, p. 314-324.

Vimont, D. J., Wallace, J. M., and Battisti, D. S., 2003, The seasonal footprinting mechanism in the Pacific: Implications for ENSO: Journal of Climate, v. 16, no. 16, p. 2668-2675.

Ware, D. M., and Thomson, R. E., 2005, Bottom-up ecosystem trophic dynamics determine fish production in the northeast Pacific: Science, v. 308, no. 5726, p. 1280-1284.

Warner, J. C., Armstrong, B., He, R. Y., and Zambon, J. B., 2010, Development of a Coupled Ocean-Atmosphere-Wave-Sediment Transport (COAWST) Modeling System: Ocean Modelling, v. 35, no. 3, p. 230-244.

Weare, B., Navato, A., and Newell, R., 1976, Empirical Orthogonal Analysis of Pacific Sea Surface Temperatures: Journal of Physical Oceanography - J PHYS OCEANOGR, v. 6, p. 671-678.

Wei, M. Z., Toth, Z., Wobus, R., and Zhu, Y. J., 2008, Initial perturbations based on the ensemble transform (ET) technique in the NCEP global operational forecast system: Tellus Series a-Dynamic Meteorology and Oceanography, v. 60, no. 1, p. 62-79.

Wu, W. L., Lynch, A. H., and Rivers, A., 2005, Estimating the uncertainty in a regional climate model related to initial and lateral boundary conditions: Journal of Climate, v. 18, no. 7, p. 917-933.

Wu, Y. J., Duan, W. S., and Rong, X. Y., 2016, Seasonal predictability of sea surface temperature anomalies over the Kuroshio-Oyashio Extension: Low in summer and high in winter: Journal of Geophysical Research-Oceans, v. 121, no. 9, p. 6862-6873.

Xie, S. P., 1999, A dynamic ocean-atmosphere model of the tropical Atlantic decadal variability: Journal of Climate, v. 12, no. 1, p. 64-70.

Yasuda, I., Okuda, K., and Hirai, M., 1992, Evolution of a Kuroshio Warm-Core Ring - Variability of the Hydrographic Structure: Deep-Sea Research Part a-Oceanographic Research Papers, v. 39, no. 1a, p. S131-+.

Yeh, S. W., Kirtman, B. P., Kug, J. S., Park, W., and Latif, M., 2011, Natural variability of the central Pacific El Nino event on multi-centennial timescales: Geophysical Research Letters, v. 38.

Zhang, H. H., Deser, C., Clement, A., and Tomas, R., 2014, Equatorial signatures of the Pacific Meridional Modes: Dependence on mean climate state: Geophysical Research Letters, v. 41, no. 2, p. 568-574.

Zhang, X., Marta-Almeida, M., and Hetland, R. D., 2012, A high-resolution pre-operational forecast model of circulation on the Texas-Louisiana continental shelf and slope: Journal of Operational Oceanography, v. 5, no. 1, p. 19-34.

Zhang, Y., Wallace, J. M., and Battisti, D. S., 1997, ENSO-like interdecadal variability: 1900-93: Journal of Climate, v. 10, no. 5, p. 1004-1020.

Zhang, Y., Wallace, J. M., and Iwasaka, N., 1996, Is climate variability over the North Pacific a linear response to ENSO?: Journal of Climate, v. 9, no. 7, p. 1468-1478.